UNIVERSITY OF TECHNOLOGY, SYDNEY

MFL Based Advanced Condition Assessment for Aged Cast Iron Pipes

by

Wijerathna Mudiyanselage Buddhi Sachith Wijerathna

A thesis submitted in partial fulfilment for the
degree of Doctor of Philosophy

in the
Faculty of Engineering and IT
Centre for Autonomous Systems

February 2016

Declaration of Authorship

I certify that the work in this thesis has not previously been submitted for a degree nor has it been submitted as part of requirements for a degree except as fully acknowledged within the text.

I also certify that the thesis has been written by me. Any help that I have received in my research work and the preparation of the thesis itself has been acknowledged. In addition, I certify that all information sources and literature used are indicated in the thesis.

Signature of Student:

Date:

UNIVERSITY OF TECHNOLOGY, SYDNEY

Abstract

Faculty of Engineering and IT
Centre for Autonomous Systems

Doctor of Philosophy

by Wijerathna Mudiyanselage Buddhi Sachith Wijerathna

Demanding essential industries such as water, petrochemical and energy use billions of dollars worth of metallic pipe infrastructure. Sydney Water Corporation alone has buried systems valued at over $15 billion and this is typical for large utilities. Catastrophic failures of these critical high pressure water pipes has severe impact on the general public, including disturbance to water supply, road traffic, compromised safety and surrounding infrastructure costing billions to the economy.

This raises the specific demand of accurate and reliable in-service inspection and maintenance of supply lines that do not disturb the service. A vibrant collaboration of researchers from Monash University, University of Technology Sydney and University of Newcastle along with ten water utilities and research institutes from around the globe are dedicated to research on 'The Advanced Condition Assessment and Pipe Failure Prediction Project' through a collaborative research agreement and committed overall funding of $16 million.

Condition assessment of Cast Iron (CI) water mains is a major part of the project where non-destructive evaluation (NDE) technologies are considered. Magnetic Flux Leakage (MFL) technology has been a popular choice in the industry for NDE for decades, and hence it is a focus technology of this project. Obtaining accurate and reliable interpretations using MFL signals is a significant challenge due to the ill-posed nature of the inverse problem. Therefore the main contributions of this thesis stem from the use of different interpretation techniques to solve the MFL inverse problem.

In this thesis, initially a realistic analytical model was developed to capture the behaviour of MFL signals. Analytical model has restrictive assumptions and could not be utilised to solve the MFL inverse modelling. Therefore a data analytic approach using Gaussian Processes (GP) is proposed to capture highly complex MFL inverse model. The caveat in this method is that it is highly dependent on the quality of training data. To generate the required exhaustive data, a more generalised FEA based simulation model was developed and validated. The simulation model enabled the generation of exhaustive data to train a GP model and the model predictions were validated using the simulation data. This raised the need for experimental validation of the models and therefore the simulation model was experimentally prototyped. With successful experimental validations using the prototyped MFL lab set-up, a software module was produced to interpret real life

industrial MFL data. This software produces $2.5D$ cylindrical approximated defect profile along with the uncertainty for each prediction.

Stress and failure analysis literature shows that ellipsoidal defects are the most vulnerable stress failure sources on gray cast iron pipes. In order to approximate ellipsoidal defects on aged CI pipes, a global optimisation procedure has been proposed. Using an analytical model the global optimisation algorithm produces the optimum ellipsoidal parameters which minimises the mismatch between the measurement and model output. The proposed algorithm produced high quality ellipsoidal parameters which can readily be used in the stress analysis.

MFL interpretation results were not only used for stress analysis, but also for multi-sensor fusion within the project. In this way, complementary information from different sensing modalities can be fused to enhance the overall prediction quality. Approximated cylindrical defects and ellipsoidal defects provided sparse information but this was not sufficient for multi-sensor fusion. A dense representation of the entire scan area is highly desirable. Further investigations of the MFL signals indicated that they contain information to interpret continuous thickness profiles. A global optimiser based on a FEA model has been iteratively used to estimate the continuous thickness profile. The results indicate that the proposed framework can accurately interpret dense $2.5D$ thickness maps.

This thesis addressed the MFL data interpretation problem in 3 specific scenarios; cylindrical defects approximation, ellipsoidal defects approximation and continuous remaining wall thickness profiling. Simulations, lab experiments and field trials were carried out for each scenario and the results were used to validate the effectiveness of the algorithms.

Acknowledgements

I am sincerely in debt to my supervisor, Associate Professor Sarath Kodagoda who was a benevolent shadow behind me through my entire candidature. Also to my co-supervisors Associate Professor Jaime Valls Miro and Dr. Teresa Vidal Calleja for believing in me and for giving me a free hand to work on my lifelong passion. Their continuous support, guidance and enthusiasm made this feat both achievable and memorable. Thanks for the countless hours of thought provoking discussions, both technical and otherwise, for they were the bits that I enjoyed the most.

I would also like to thank Professor Gamini Dissanayake and Professor Tomonari Furukawa for the fruitful discussions and for their continuous encouragement. I would like to extend my gratitude towards Asset Integrity Australasia (Pty) Ltd and Advanced Engineering Solutions Limited, the industry partners for this research. Moreover I extend my gratitude to the entire UTS Advanced Condition Assessment and Pipe Failure Prediction Project research team including Dr. Alen Alempijevic, Dr. Brad Skinner, Dr. Lei Shi, Dr. Qiang Zhang, Mr. Freek De Bruijn, Mr. Nalika Ulapane, Mr. Raphael Falque, Mr. Daobilige Su and Ms. Sun Liye, for constructive feedback throughout the entire candidature. Also I acknowledge the valuable feedback from other project collaborators from The University of Newcastle and Monash University.

To all my friends at CAS, thanks for the four years of good laughs, best ever games of badminton and above all, unrivalled comradeship. To all the academic and support staff at CAS, thanks for taking me in and making me part of the family. Never have I felt more at home than in these past four years. My special gratitude to my friends Raphael, Lakshitha, Lasitha and Nalika for being there with me to go through easy and hard times.

This thesis is an outcome from the Critical Pipes Project funded by Sydney Water Corporation, Water Research Foundation of the USA, Melbourne Water, Water Corporation (WA), UK Water Industry Research Ltd, South Australia Water Corporation, South East Water, Hunter Water Corporation, City West Water, Monash University, University of Technology Sydney and University of Newcastle. The research partners are Monash University (lead), University of Technology Sydney and University of Newcastle.

Finally, I am ever in debt to my family, dear amma and appachchi (mom and dad) who made great sacrifices in making me who I am today.

Contents

List of Figures

List of Tables

Abbreviations

AMR	Anisotropic Magneto-resistive
ANN	Artificial Neural Networks
CI	Cast Iron
DWT	Discrete Wavelet Transform
DI	Ductile Iron
FEA	Finite Element Analysis
GA	Genetic Algorithm
GT	Ground Truth
HPC	High Performance Cluster
MFL	Magnetic Flux Leakage
MPI	Magnetic Particle Inspection
MS	Mild Steel
NDE	Non-Destructive Evaluation
PCA	Principal Component Analysis
PEC	Pulsed Eddy Current
RBFNN	Radial Basis Function Neural Network
RT	Radiography Testing
RFT	Remote Field Testing
RPM	Revolutions Per Minute
RMS	Root Mean Square
SNR	Signal to Noise Ratio
SCF	Stress Concentration Factor (SCF)
UT	Ultrasonics(UT)

Nomenclature

Symbol	Quantity
$f(\cdots)$	A scalar valued function
$\boldsymbol{f}(\cdots)$	A vector valued function
$[\cdot]_x$	The x component of a vector
$[\cdot]_y$	The y component of a vector
$[\cdot]_z$	The z component of a vector
$\dot{[\cdot]}$	The time derivative of a variable
$[\cdot]^T$	Transpose of a vector or a matrix
$\|\cdot\|$	The magnitude of a vector
$[\cdot](p,q)$	The $(p,q)^{th}$ element or block of a matrix
$[\cdot](p,:)$	The p^{th} row or row block of a matrix

	Specific Symbol Usage
k	Coefficient of friction
$\vec{I}$	Electric current
$\vec{J}$	Electric current density
$\vec{E}$	Electric field intensity
f	Frequency
σ	Magnetic charge density
$\vec{H}$	Magnetic field intensity
Φ	Magnetic flux
$\vec{B}$	Magnetic flux density
$\vec{A}$	Magnetic vector potential

μ	Permeability
μ_0	Permeability of free space
ϵ_0	Permittivity of free space
$P(\cdot)$	Probability
μ_r	Relative permeability
p	Remaining wall thickness
$f(\cdot)$	Scalar valued function
β	Hyper-parameters of the covariance function
t	Time
τ	Torque

Glossary of Terms

Autonomous	No human intervention involved.
Calibration Defects	Circular shaped flat bottom drilled holes to known dimensions for the purpose of calibration and localisation.
Critical Pipes	Large diameter (usually $\geq$ 300mm) high pressure pipes.
Critical Pipe Materials	Materials usually used for manufacturing critical pipes.
Lift-off	Distance between the sensor and the nearest pipe surface.
Semi-Autonomous	Some degree of human intervention involved.
Testing Data	Set of data used to evaluate algorithms.
Training Data	Set of data used to discover potentially predictive relationships.

Chapter 1

Introduction

Worldwide about 70% of the total asset base of a typical urban water utility consists of buried pipes in congested cities [7]. Most of these critical water pipes are extensively large diameter and operate in critical water pressure conditions subjected to pump station pressure transients as well. Most major urban water utilities in the world including Australia have been in service for a century or even more [7–9]. Sydney Water Corporation [10] has buried systems valued at over AUD 15 billion and this is typical of large utilities.

Failure of these critical high pressure water pipes has severe impact on maintaining the continuous service to the public, fire fighting capabilities specially in bush fire areas in Australia, compromised safety, disturbance to general public including road traffic, other social costs as well as significant financial and reputational implications.

With further aging of this mission critical infrastructure, probability of failures will continue to increase [7]. This will have very high growing cost implications for the reliability and sustainability of the public water supply. It is clear that this is a global issue which will become even worst with global climate changes and soil property changes due to industrialisation.

In Australia, the total replacement costs of the pipe network have been estimated to exceed AU$100 billion [9]. Over the next five years, the costs of urgently needed asset replacement are around AU$5 billion. Maintenance costs over the same period are estimated at some AU$2.5 billion [9]. Elsewhere, The US Environmental Protection Agency (USEPA)

estimates that the US public water sector will require US$335 billion of capital investment over the next 20 years to sustain essential service levels. Also, US studies indicate that the average cost per failure for large diameter pipes exceeds US$500,000 [9].

In response to these cost drivers, and to meet demands for reliable water supply services, water utilities have already made considerable efforts to control potential failures by applying existing, state-of-the-art methods for failure prediction, condition assessment and proactive pipe asset management technologies. The methods used have limited level of confidence which limits the ability to target renewal programs. It has been conservatively estimated that even a 30% improvement in the present state of the art, would reduce the high consequence events by 50% and total failure events by 30% resulting in potential savings of over AU$160 million over a 20 year period to the Australian Water industry [9]. With better prediction from condition assessment, expenditure can be delayed by 5 years and replacement costs reduced up to 20%; the projected savings over a 20 year period will exceed a further AU$300 million [9].

Water utilities urgently need better techniques for estimating the probability of failure of critical pipelines and for estimating their remaining life. The unavailability of such tools increases the risk of substantial funds being potentially misdirected through premature replacements. This could impact on future water service pricing. On the other hand, not undertaking timely replacement of pipes could lead to increasing number and frequency of failures with associated costs and disruption. A vibrant collaboration of researchers from Monash University, University of Technology Sydney and University of Newcastle along with ten water utilities and research institutes from around the globe are dedicated to research on 'The Advanced Condition Assessment and Pipe Failure Prediction Project' through a collaborative research agreement and committed overall funding of $16 million. This thesis is produced as part of this research project and strives to produce better interpretation results to the water utilities for their decision making.

The project consists of three main research teams. University of Technology Sydney team focuses on improvement of condition assessment techniques. Monash university uses the condition assessment results to conduct stress analysis to examine the structural properties of aged pipes. The University of Newcastle works on corrosion modelling. Therefore

condition assessment plays a major role in the project as the results are used by other research teams for their work.

Corrosion and graphitisation are the main causes which weaken the strength of aging critical pipes and cause them to fail eventually [7, 11]. Knowing the amount of non-compromised conductive ferromagnetic material remaining in the pipe walls is therefore the key first step towards lifetime/failure prediction.

Since corrosion and graphitisation occur on inner and outer surfaces of pipe walls, healthy material often remains in subsurface regions which cannot be accessed directly. Causing any physical destruction to critical pipes even in the form of corrosion removal done to access the healthy material surface is undesirable due to the risk of pipe bursts. Therefore, the amount of healthy material can only be evaluated non-destructively. Consequently, many NDE techniques have emerged and grown in demand in the field of pipe condition assessment [12].

The following describes most commonly used NDE techniques in metallic structures. One of the earliest techniques in NDE is radiography (RT). This is analogous to the medical X-ray. A beam of radiation is released and diverted through the object being inspected. X-ray sensitive film or a sensor in modern designs records a $2D$ image correlated to the varying densities of the absorption of the radiation. RT is used in weld quality inspections and other quality control procedures but there is a variety of safety issues and it is not convenient to use for in-situ pipe inspections.

High frequency sound waves (typically around $1MH_z$) have the ability to transmit through solids and the associated technologies are known as ultrasonics(UT). A very useful feature is that any discontinuity or change of density produces a reflection and this can be turned into an 'image' by measuring the signal travel time. UT is commonly used for precise crack detection in relatively small items. Due to the focal length of the sensor, the technology cannot be used to detect shallow surface cracks. A significant disadvantage is that there is quite a degree of operator skill required and consequently the industry requires formal qualifications for UT operators. UT probe needs very good coupling to the material and this limits the use of UT on cast iron due to the graphitisation layer on aged cast iron pipes.

Liquid Penetrant also known as Dye Penetrant or Dye Check is widely used to find open cracks with live leaking. The idea is simple. A coloured special dye is applied on the surface and after an interval the excess dye is cleaned. Inner and outer surfaces are inspected for penetrated dye. This is a very basic technique and depends on the experience of the operator. Magnetic particle inspection (MPI) is similar to the dye Penetrant method, but gives better results. A powerful magnetic field is applied to the object being inspected followed by the application of a magnetic ink or powder. Anomalies on or near the surface collect the dye and the surface is then visually inspected. This method also has a higher human involvement and is thus prune to error.

More advanced magnetic induction based methods were developed later for better inspection accuracies [12]. Pulsed Eddy Current (PEC) , Remote Field Testing (RFT) and Magnetic Flux Leakage (MFL) are examples. In PEC, by generating a high frequency current in a coil, eddy currents are induced in the test material. The inductive effect of these eddy currents can be measured as modulations of the current in the coil and can be correlated to wall thickness. There has been recent research on these techniques by applying cutting edge machine learning techniques to attain better interpretation accuracies [13].

This thesis focuses on the Magnetic Flux Leakage (MFL) technology where the test substance is magnetically saturated to generate leakage flux around the close proximity of anomalies in the material, external or internal.

The MFL phenomenon has been analysed using a dipole based analytical model as well as using a Finite Element Analysis (FEA) model to study, characterise and quantify the effects of defect geometry, defect locations and multiple defect interaction on MFL signals. The ultimate objective is to use sensor models to characterise the correlation between the MFL signals and defect parameters. Captured correlations can be used to solve the inverse problem of interpreting MFL signals collected from aged in-service critical water mains for quantitative condition assessment and asset maintenance purposes.

The thesis presents: (a) A realistic MFL model to characterise the signal behaviour in the presence of various defect scenarios; (b) Design and development of a semi-automated MFL tool for condition assessment; (c) Machine learning based MFL signal interpretation framework ; (d) An analytical model-aided iterative numerical method for ellipsoidal

defect estimation and (e) Reconstruction of dense $2.5D$ thickness maps using MFL measurements. Developed frameworks are evaluated by applying them for in-situ critical water pipe condition assessment. A commercial MFL tool commonly used in the industry has been used for data collection and commercial reported results produced for water utilities have been compared to the developed framework results.

FIGURE 1.1: Industrial MFL tool in operation [1].

The rest of this chapter introduces the research work presented in this thesis. It commences with a background of the target application scenario of critical pipe evaluation and details key research issues. The rest of the sections describe the thesis scope and its main contributions followed by the outline of the rest of the thesis.

1.1 Background

Due to their reliability and long lasting capabilities, metal pipes are used for transportation of fluids over long distances. This infrastructure demands very reliable and accurate condition assessment due to safety requirements as well as due to the very high costs involved in replacing a failure.

Non-destructive evaluation (NDE) techniques are commonly used for infrastructure inspection. With current advancements of NDE technologies, in-service inspection is getting more popular in industries such as water, petrochemical and energy where the undisturbed service is essential. There is a large number of technologies used in NDE. Research effort

is being applied continuously to come up with more effective ways of achieving reliable and cost effective NDE techniques [14].

This thesis is originated as a part of Activity 2 of the Advanced Condition Assessment & Pipe Failure Prediction Project [15], which is co-led by the University of Technology Sydney (UTS). The project is strongly supported by Sydney Water and many Australian and international water utilities, condition assessment service providers and research institutions. This activity aims to advance knowledge and improve levels of confidence of direct methods for condition assessment using sensor modelling and advanced data interpretation techniques which have already been successfully employed in fields such as aerospace, cargo handling, undersea ecology, land vehicles and mining.

Most of the commercially used NDE techniques have shortcomings. One of the main issues is the requirement of sensor calibration to achieve quantitative interpretation of pipe condition [13, 16, 17]. Accurate calibration is challenging in the target application due to the difficulty of obtaining calibration materials having properties which satisfactorily match those of critical pipes. As a result of calibration errors, interpreted pipe conditions can be observed to deviate from reality in practice. One other issue is the requirement of time-intensive manual labour to analyse signals individually to accomplish accurate interpretation.

The desired outcome of Activity 2 is a method of accurately predicting the geometric description of a buried large critical pipe, and obtaining the best estimate of the pipe geometry from a set of measurements. As a part of this activity, this thesis deals with MFL specific modelling and data interpretation. The activity 2 considers four most widely used industrial technologies; MFL, PEC, RFT and UT.

In this work MFL signals are acquired and processed to regenerate various defect information. The frameworks are developed aiming at large diameter critical water mains ($i.e. diameter > 500mm$) owned and maintained by water utility companies to supply consumable fresh water to the community. The majority of these large diameter critical water mains are made of cast iron (CI), ductile iron(DI) and mild steel(MS). Therefore these pipes are electrically conductive and ferromagnetic in nature which enables the use of magnetic NDE techniques such as MFL.

Although ferromagnetic material specific MFL signal processing techniques are available, an autonomous framework which is readily usable with commercial MFL tools is lacking in the industry. A intelligent system which models sensors and autonomously inferring pipe condition using MFL data, has the potential to greatly increase accuracy and productivity of the entire asset management process.

1.2 Objectives

Magnetic Flux Leakage (MFL) technology has been used in the industry for more than three decades for condition assessment. In the MFL inspection process, a sample of a ferromagnetic material is magnetised using a strong magnetic field. In the presence of defects or anomalies, a magnetic flux "leak" can be detected which contains information on anomalies [18–20]. Suitable sensors are employed to scan this leakage field on which different signal processing techniques are applied for detection and sizing of them.

There are several commercially available magnetic flux leakage inspection services. Table 1.1 summarises some of the industrial MFL service providers. Advanced Engineering Solutions Limited uses an external MFL tool to scan the pipe wall thickness. They report the individual defect information. Silverwing (UK) Ltd also provides a range of external MFL tools designed for a range of applications such as floor scanning, pipe scanning and gas tank scanning. in contrast, Weatherford International Ltd provides services using an internal pigging MFL tool which can travel through the pipe long distances. Most of these organisations does not reveal the sensors they use nor the algorithms they use to interpret MFL signals. Only the industry partners of this project have provided their results to evaluate the developed algorithms and results are superior to industry partner's results. These algorithms and results are presented in the following chapters.

MFL signals are strictly dependent on the geometry of defects as well as the properties of the material being tested. Two main frameworks are generally employed to interpret MFL signals. The more traditional forward approach requires knowledge of precise calibration samples to generate reference MFL signals. The readings acquired on reference test pieces with known geometry and intrinsic material properties are compared with fresh readings

Table 1.1: Examples of industrial MFL service providers

Company name	Tools used	Company URL
Advanced Engineering Solutions Limited	smartCAT^{TM}, smartCAT^{TM} 360, smartCAT^{TM} Hybrid, Radar - Ground Penetrating,	http://www.pipeline-inspections.com/
Silverwing (UK) Ltd	Floormap3D, FloormapVS2i, MFL2000, Handscan, Pipescan	http://www.silverw ingndt.com
Weatherford International Ltd	Inspection by Magnetic Flux Leakage (Inline inspection), Inspection by Transverse Field Inspection (TFI) Technology	http:// www.weatherford.com

to infer defect information. However this approach is highly error prone and dependent on the calibration samples.

In the application of critical pipe evaluation, however, destructive extraction is not possible due the physical damage it causes to the infrastructure. As a result, common industrial practice enables geometric calibration of critical pipe materials only by means of prefabricated calibration blocks. For critical pipe materials which include gray cast iron, ductile cast iron and mild steel, electrical conductivity and magnetic permeability values can vary approximately up to $\pm 20\%$ from the expected mean [21] due to the casting and cooling process. Such discrepancies between calibration and measurement adversely affect the measuring technique by offsetting interpreted geometric condition from the reality.

Significant human intervention in the data collection process as well as data processing has made the conventional manual MFL method inherently slow and error-prone. This process can be advanced with the use of today's cutting edge signal processing and analysis technologies which will result in more accurate modelling and prediction. In particular, machine learning algorithms are well-suited for robust modelling of MFL signals.

Although the second type, inverse approach, is more complex, it produces more accurate and robust results. The inverse approach fits a model that can be used to predict the

defect configuration from the MFL signals. This study is focused on the inverse modelling of MFL signals by using state of the art machine learning and optimisation techniques in order to detect and size corrosion defects.

1.3 Scope

This thesis specifically aims to develop MFL based advanced condition assessment techniques for industrial applications. Developed approaches are intended to overcome the issues related to calibration and the requirement of manual data interpretation, in addition to being able to accurately predict pipe condition with the associated uncertainty.

Designing a novel MFL sensor architecture having better and more accurate measurement capabilities is not an objective of this research. The industry partner of the research project who provide commercial MFL services to water industry supplies a MFL tool with a fixed sensor architecture. This tool is used to collect raw data from site trials. The scope of this thesis is limited to the excising design of this industry tool. This tool is an external pipe scanning tool with a U-shaped electro-magnetic exciter. The objective is to use this standard MFL sensor architecture and to propose approaches to better interpret the data to cater for the different requirements of the client, in this case the water utility company.

The U-Shaped MFL tool parameters are considered known through out the thesis, although challenges were faced with the proprietary information acquired from the industry partner. Reasonable assumptions and methods were followed to overcome these challenges and these are described in Chapter 3.

Since the target application of this thesis is critical pipe assessment, and aged critical pipes are found in any of the three critical pipe materials: gray cast iron, ductile cast iron or mild steel [7, 8, 11]. All NDE related developments are experimented on in-situ pipes made of critical pipe materials. Due to the popularity and higher rate of failure according to historic data, this project mainly focuses on gray cast iron pipes. However, the proposed approaches can be generalised for condition assessment of any electrically conductive and ferromagnetic material.

The reconstructions done are mainly for evaluating the structural integrity of the pipes and for lifetime prediction of the remaining material. Developed frameworks are not required to generate the full 3D reconstruction of the pipe wall and it is very challenging to reconstruct the 3D profile only by using external scans. Therefore this thesis produces the interpretations as remaining wall thickness values and $2.5D$ thickness maps.

1.4 Contributions

This thesis presents a four main contributions. First presents a comprehensive methodology to develop a realistic MFL model followed by a prototyped lab set-up. A dipole based parametric analytical model captures the underlying MFL phenomenon. This model also validates the MFL FEA model. In the proposed framework the simulation model is prototyped as an improved MFL lab set-up that employs a semi-automated scanning procedure. The developed realistic model is used to generate extensive data required for the data analytic methods [22].

The advent of kernel machines, such as Gaussian Processes (GP) can be formulated as a non-linear regression. This thesis presents a Gaussian processes based data driven inverse modelling framework to characterise the geometry of multiple defects, *i.e.* depth and width of defects and their associated uncertainties [22]. The GP models trained with the validated simulation models, generate accurate predictions and the associated uncertainties which can be used in the decision making process of asset maintenance. The results are superior to the state of the art industry interpretations.

Latest stress and failure analysis shows that ellipsoidal defects are the most vulnerable stress failure source on gray cast iron pipes [23]. A novel analytical model-aided ellipsoidal defect estimation framework is introduced to aid these stress concentration factor (SCF) calculations. This framework utilises a non linear optimisation algorithm using a MFL analytical model. The ellipsoidal parameters are estimated based on raw MFL signals compared to model generated signals and it is verified through simulations and experiments.

This thesis also presents a global optimiser based framework to reconstruct a dense $2.5D$ high resolution thickness map of the entire scan area using MFL signals generated on ground truth. Non linear optimisation framework minimises the mismatch between the MFL measurement signal and the FEA simulated signal. Reconstruction results are compared with ground truth to validate the algorithm [22].

1.5 Thesis Outline

This thesis consists of seven main chapters. The second chapter which comes after the introduction, contains a review of related work in the field of MFL sensing and interpretation. The chapter presents MFL sensor operating principles, sensor architectures and applications. MFL sensor modelling techniques are subsequently investigated and the chapter concludes by reviewing published research work on iterative optimisation techniques used for coarse to fine interpretation of MFL signals.

The third chapter describes the development of a Realistic MFL Model and a Semi-Automated Tool. It first introduces the underlying MFL phenomenon through a detailed derivation of a dipole based parametric analytical model for MFL. Later this model is generalised using a FEA based simulation model. This simulation model is prototyped and used for experimental validation. With the successful validation, the model has been used for extensive data generation, capturing most geometrical defect scenarios. This data is used in a machine learning approach in the following chapter. The third chapter also discusses the existing shortcomings in the commercial tools and how they could influence the final interpretations. Due to greater industry motivation, the chapter presents a detailed design process of an improved semi-automated MFL tool. With the experimental results it is demonstrated that this design aids in the higher estimation accuracy of the remaining wall thickness as well as defect shape interpretations.

The fourth chapter utilises the data generated in Chapter 3 for machine learning. The chapter discusses the possibility of using Gaussian Process models to formulate a Bayesian framework for non-linear regression. This chapter presents a GP based data driven inverse modelling framework to characterise the geometry of defects. This framework uses

simulated data along with the corresponding defect parameters to learn the models in a supervised learning manner. Raw measurements from aged CI pipes are used to evaluate these inverse models and the results are compared with a laser measuring system based ground truth.

The fifth chapter identifies the importance of ellipsoidal defect approximation for stress analysis. The analytical model presented in Chapter 3 is extended to analyse a general ellipsoidal defect. Given the MFL signal of a certain area, inverse modelling of approximated ellipsoidal defects is formulated as a non linear optimisation problem using the analytical model. A global optimisation algorithm has been used to produce the optimum ellipsoidal parameters which generate a similar signal to the measurement. Four ellipsoidal defects were machined on grit-blasted CI pipes and corresponding MFL signals were used to evaluate the framework.

The sixth chapter further makes use of iterative numerical methods to refine MFL interpretations. A global optimiser based on a FEA model and a moving ROI has been iteratively used to solve the RWT profile. By using the GP based interpretation as the initial seed, the method is formulated as a coarse to fine approach. Finding the thickness profile that minimised the model mismatch to the reference measurement, is equivalent to solving the inverse problem. Extensive simulation and experimental results are presented to illustrate that the proposed global optimisation framework is capable of accurate reconstruction of dense $2.5D$ thickness profiles.

Finally, chapter seven concludes the thesis with a summary of the key findings and the contributions. It also points to several MFL signal interpretation based future research avenues that result from the frameworks presented in this thesis.

1.6 Publications

The work in this thesis has been previously presented in the following publications.

1. Buddhi Wijerathna, Teresa Vidal-Calleja, Sarath Kodagoda, Qiang Zhang, and Jaime Valls Miro. Multiple defect interpretation based on gaussian processes for MFL technology. *Nondestructive Characterization for Composite Materials, Aerospace Engineering, Civil Infrastructure, and Homeland Security*, pages 86941Z–86941Z–12, April 2013. doi: 10.1117/12.2009966

2. Buddhi Wijerathna, Sarath Kodagoda, Jaime Valls Miro, and Gamini Dissanayake. Iterative coarse to fine approach for interpretation of defect profiles using mfl measurements. *Proceedings of the 10th IEEE International Conference on Industrial Electronics and Applications*, 2015

3. Jaime Valls Miro, Jeya Rajalingam, Teresa Vidal-Calleja, Freek de Bruijn, Roger Wood, Dammika Vitanage, Nalika Ulapane, Buddhi Wijerathna, and Daoblige Su. A live test-bed for the advancement of condition assessment and failure prediction research on critical pipes. *Water Asset Management International, ISSN Print: 1814-5434, ISSN Online: 1814-5442*, 10(2):03–08, 2014

4. Daobilige Su, Nalika Ulapane, and Buddhi Wijerathna. An acoustic sensor based novel method for 2d localization of a robot in a structured environment. *Proceedings of the 10th IEEE International Conference on Industrial Electronics and Applications*, 2015

Chapter 2

Related Work

Due to the demanding requirements of the industry, NDE techniques had been a major research topic for decades. There are a wide variety of challenges in developing frameworks which take into account measured intrinsic material properties and sensor signals to predict the condition of the test area.

The main focus of this thesis being MFL technology, few major sub areas are identified in literature. This chapter first reviews various mathematical modelling techniques as well as different MFL sensor architectures. Limitations in these models raise the need for generalised FEA models. Challenges and existing work towards FEA modelling is presented in the next Section.

Having realistic forward models enables researchers to address the inverse problem of finding defect properties using MFL measurements. In literature, there exists several studies towards inverse modelling using simple direct methods as well as more sophisticated data driven machine learning techniques.

This chapter further includes published work regarding noise suppression techniques, permeability and speed invariant schemes. It also identifies that there is a lack of published work related to ellipsoidal defect estimation using MFL signals; this will be studied in Chapter 5.

2.1 Forward Modelling of MFL

One of the earliest research interests was to develop theoretical models to analyse the MFL phenomenon. The idea was to develop mathematical MFL models incorporating defects and various other parameters to affect the leakage signal. Fitting these models to data from an unknown defect can give an estimate of the size of the defect. Zatsepin and Shcherbinin [26] modelled the leakage field from infinitely long surface-breaking cracks considering a point dipole, linear dipole or strip dipole in terms of magnetic charge induced by the external magnetic field on the bounding surfaces of the cracks. Having infinitely long defects is far from the reality. Shcherbinin and Pashagin [27] developed a more sophisticated model extending the previous work into cracks with finite dimensions.

Forster, in [2] describes mathematically the magnetic flux leakage phenomenon. He claims that the determination of the magnetic field strength inside the defect as a function of defect geometry, magnetic properties of the material and applied field strength is required for a better understanding of the magnetic flux leakage phenomenon. The total process of leakage flux measurement including the necessary mechanical probe movement, was controlled by a computer which also evaluated the measurements subsequent to the measuring process. These were drawn with high precision by a plotter in a programmed manner. The tangential H_x and normal H_y leakage field components were measured using the Hall probes. The focus was mainly on a few features of the curves on the experiments. (see Figure 2.1)

The authors observed that the spread of H_x and H_y profiles increased as the widths of the defects increase, and there is a relatively small change in the peak-to-peak magnitude of the H_y profiles as the depth changes (Figure 2.1(b)). Foster also identified that,

- A decreasing crack width corresponds to an increase of magnetic field strength beside a crack
- As the crack width increases the percentage decrease of H_x in the surroundings grows
- The two opposing effects described caused a convergence of the values of H_x from about y = 1 mm for the different crack widths (see Figure 2.1)

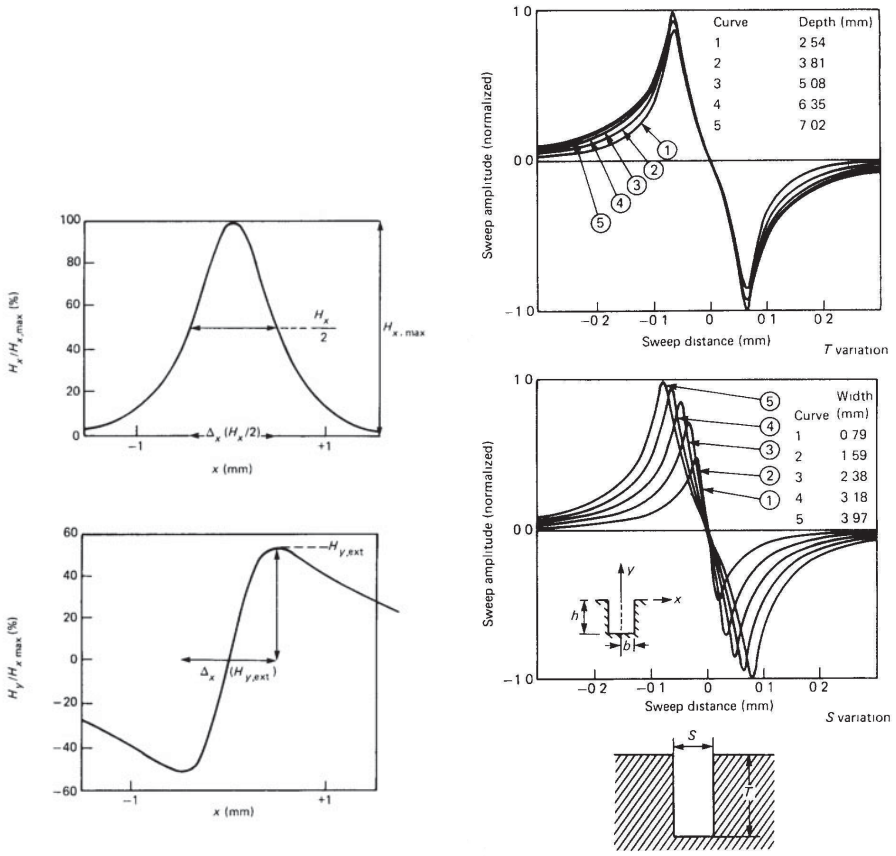

(a) (b)

FIGURE 2.1: Features and their behaviour of a MFL signal [2] where H_x is the axial component and H_y is the radial component. (a) Identified features; (b) Feature behaviour of the radial component.

- The homogeneity of the internal field H, increases with increasing crack depth

Forster also discussed the practical significance of the different sections of the magnetisation curve and hysteresis loop to the magnetic flux leakage method for non-destructive material testing. For non linear permeability, the field inside the defect was found to be higher, and an explanation as well as empirical correction factor were proposed. Hence, Forster demonstrated that earlier dipole simulations in the literature that studied the variation of MFL magnitudes with defect parameters were invalid, because they assume that the induced magnetic charge density was independent of the defect parameters. He concluded that the magnitude of the radial MFL component increased linearly with defect

depth. Moreover he experimentally demonstrated that the magnetic field inside the defect increases as the defect width decreases. In conclusion the author emphasised the fact that, comparison of results published in the literature computed according to the method of finite elements and the results of experiments showed a considerable discrepancy.

R. C. Ireland and C. R. Torres [28] modelled a circumferentially magnetised MFL tool using finite element analysis. First they used a 2D model and later extended it into a 3D model. The 2D model indicated that the defect response picked up by the sensors was dependent on the position of the defect with respect to the tool's magnetic poles. This happened due to the large value of the background magnetic field close to the poles, which can also make defect characterisation difficult. They also presented that several inspections of the same section of pipeline might yield different defect signatures due to the position of the magnetic poles with respect to the pipe being altered for each run. Sensitivity of the sensors, placement, calibration and manufacturing tolerances might also lead to non identical results. However, the modelling results presented, indicate that the magnetic field profile seen within the pipe, is extremely complex under both stationary and dynamic tool conditions. They suggested that understanding the nature of the varying magnetic field profile is the key to develop an optimal circumferential MFL tool. In the same publication they presented modelling and finite element analysis results but they did not present interpretation or classification methods to detect and size defects.

Typically, magnetic sensors measure individual components of a MFL field. Babbar [5] as well as Atherton [29, 30] argued that the radial component B_z is the most significant component of a MFL field whereas the other two components were still not completely investigated at the time.

The FEA published by Yong Li [31] reveals that all three components of the magnetic field over the defect region, not only complement each other but also enhance the detection and characterisation of defects. The simulation studies were undertaken for MFL inspections with rectangular slots and natural irregular cracks. The magnetic field was quantified using a 3-axis anisotropic magneto-resistive (AMR) field sensor. They noticed that the circumferential (B_y) component is particularly informative in detecting the diagonally orientated section of a crack, whereas the axial component (B_x) and radial component (B_z)

contains very little indication of crack position. In the simulations, although there were localisation discrepancies in the magnetic field, the overall distribution of the 3D leakage field from experimental study had good agreement with FEA simulation results. They claimed the discrepancies were due to the inhomogeneous field and non linear material properties of the arbitrary shaped test samples. So finally they concluded that the use of a 3-axis system would be advantageous in certain situations to give orientation information, especially when defects were orientated parallel to the applied field.

2.2 Defect detection and sizing

Rather than straight forward inspection of the leakage flux foot print, researchers tend to investigate various other techniques to analyse, detect and size the defects using the readings of MFL tools.

D. Minkov [32] proposed a method for estimating the sizes of surface cracks in magnetic materials based on applying a magnetic field, determining the leakage magnetic field in the vicinity of a crack by moving a Hall element along straight lines crossing a surface crack and measuring the corresponding Hall voltage distribution. The sizes of the investigated cracks were estimated by regression where they minimised the RMS error between the variable theoretical Hall voltage distribution and the measured Hall voltage distribution. The method was based on a dipole model of a crack. It utilised analytical expressions for determining the theoretical Hall voltage distribution. The analytical expressions neither imposed boundary conditions at the crack walls nor required knowledge of any material constants. They estimated only the maximum depth and the width of an investigated crack which was especially useful due to its practical applicability, simplicity and speed.

Catalin Mandache [33] also addressed the inverse problem of defect size prediction directly from MFL signals. An analytical model was modified to account for circular defects in order to correlate the radial component of MFL profile with the defect dimension along the axial magnetic field. They confirmed the validity of the model through comparison with experimental MFL scans from different defect geometries. The theoretical model developed for a single cylindrical defect was adapted to more complex and realistic defect geometries,

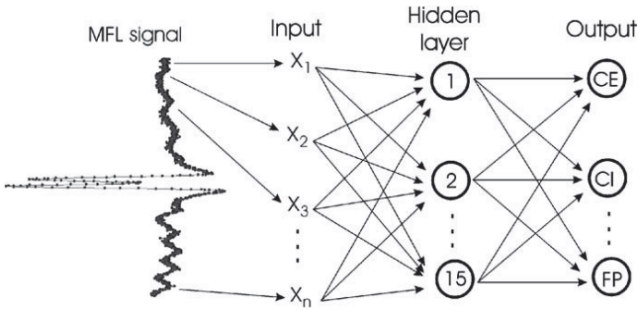

FIGURE 2.2: Neural networks used in MFL for pattern recognition [3]

specifically, racetrack defects. They used very few features of the radial component of the MFL leakage signal such as the peak magnitude and the distance between two peaks. They claimed that the advantage of the method is the low number of parameters that have to be considered when determining the length of defects using radial signal component. The knowledge of material characteristics, such as permeability was not a necessity, as long as the inspection magnetic field strength corresponds to the magnetic saturation of the sample.

Since these inverse approaches are fairly straightforward matching approaches they are not well resistant to noise and other practical imperfections. However this approach can be further advanced using modern machine learning techniques. There have been few attempts in defect detection and sizing using machine learning techniques.

Artificial neural networks (ANNs) are commonly used in modelling complex relationships. A.A. Carvalho [3] evaluates the use of artificial neural networks (ANNs) for pattern recognition of magnetic flux leakage (MFL) signals in weld joints of pipelines obtained by an inline inspection tool (See Figure 2.2). Initially the ANNs were used to distinguish the presence of defects using signal patterns along the weld bead. The initial input to the neural network was without any type of pre-processing, but later they applied a new layer of pre processing too.

Their initial approach was a moving average filter with a numerical procedure that smoothes data by replacing each original signal data point with the average of the neighbouring signal data points. However these filters tend to eliminate information of high-frequency components of the signal along with the noise.

Later they analysed the frequency response of the signal. The Fourier analysis consists of decomposing the signal into its constituent sinusoids of different frequencies. However, many signals contained numerous transitory or non-stationary characteristics, such as abrupt changes, fluctuations, discontinuities. Often these characteristics were the most informative part of the signal and in this case the Fourier analysis was not the most appropriate.

Carvalho [3] also investigated the use of wavelet transform. Wavelet transform is specifically developed to overcome the limitations of the Fourier analysis. The wavelet transform supplies information on when and in which frequencies the events occurred. Savitzky-Golay smoothing filter[34, 35] was also used. This filter is known as a digital smoothing polynomial filter or least-squares smoothing filter, and is typically used to smooth signals with noise and with large frequency intervals. This filter is less sensitive to the frequency interval since output is obtained by the adjustment of the points of the interval by a polynomial and not by the simple average of the neighbouring points, as occurs with the standard moving-average filter. This characteristic allows the Savitzky-Golay filter to be applied to analytical signals with sharp peaks, which is common in MFL signals.

Ahmad Khodayari-Rostamabad [36] presented a complete machine learning framework for the inspection of MFL images from pipelines. This included feature extraction, feature selection, pattern-recognition and regression methodologies to detect major defects in pipelines. They applied the methods of support vector regression, keratinisation techniques, principal component analysis, partial least squares, and methods for reducing the dimensionality of the feature space. They demonstrated the adequacy of the performance of these methods using real MFL data collected from pipelines, with regard to the performance of both the detection of defects and the accuracy in the estimation of the severity of the defects.

The average detection performance in recognising major metal defects vs non injurious or benign anomalies was over 96%. The root-mean-square error in defect depth estimation was less than 8%. Furthermore, the kernel PCA method provided a low-dimensional representation of the MFL data and was presented as an effective visualisation tool.

Not only defect detection and sizing, but classification of the defects is very important too. A.A. Carvalho [3] applied ANNs to classify signal patterns with three types of defects in a weld joint: external corrosion (EC), internal corrosion (IC) and lack of penetration (LP). The defects were intentionally introduced in the weld bead of a steel pipeline with an outer diameter of $304mm$. The MFL signal itself was digitised into 1025 samples, and was used as the ANN input. All the signals from three specimens were grouped together in a single set of data and then randomly separated into a training set (70% of data) and a test set (30% of data). Later fresh data was used for validation.

Signal processing techniques were employed to improve the performance of the neural networks in distinguishing between the defect classes. The results showed that it was possible to classify signals into defect and non-defect classes using ANN with promising results (94.2% success), as well as for corrosion (CO) and lack of penetration (LP) signals (92.5% success). They could also classify the defect pattern signals: external corrosion (EC), internal corrosion (IC) and lack of penetration (LP) using neural networks with an average rate of success of 71.7% for the validation set.

Ameet Joshi [37] and his team also focused on machine learning aspects of the MFL signal. They were more interested in the maximum safe operation pressure (MAOP) since their focus was on natural gas pipelines. In order to obtain a more accurate estimate for the MAOP, it was necessary to interpret the MFL signal to achieve the full $3D$ defect depth profile. They proposed an iterative method of inversion using adaptive wavelets and radial basis function neural network (RBFNN) that can reduce the dimensionality and predict the full $3D$ depth profile.

In order to use wavelet transform efficiently, the depth profile X was re-sampled to match the magnetic field H at a resolution of 10×16. Their inversion procedure followed a multi resolution approach for reconstructing the defect and consists of several steps.

The $1D$ vector representation of H was obtained using $2D$ Haar wavelets and discrete wavelet transform (DWT) as Equation 2.1

$$h = \sum_{i=1}^{L} \sum_{j=1}^{4^L} c_{ij} \phi_{ij} \tag{2.1}$$

where ϕ_{ij} is the j th wavelet at i th level. The coefficients c_{ij} , provide a compact representation of the unknown defect profile. Inverse DWT transforms the coefficient vector c to the depth profile h.

The radial basis function neural network (RBFNN) [38] was used to model the forward process of predicting the MFL signal for a given depth profile. The parameters of the forward model were computed using training data. The iterative operation using the RBFNN estimated optimal values of the wavelet coefficients. The DWT algorithm recursively calculated the next level Haar coefficients. Low energy coefficients were eliminated and the remaining coefficients were applied to the inverse DWT algorithm to generate the next higher resolution depth profile. The process terminated when it reached resolution level L_{max}. In essence this algorithm starts with a coarse resolution prediction of the depth profile and then finds the optimal representation of the depth profile in that resolution. As the algorithm provides a coarse-to-fine improvement in the prediction, it can be adapted depending on the accuracy speed trade off. It then improves the resolution in areas of spatial domain having an energy more than a predefined threshold.

Coefficients having energy below the predefined threshold were eliminated. They generated a database of 71 defect geometries and corresponding MFL signals. In every experiment, 70 samples were used for training and the remaining for sample testing. The multi-resolution iterative inversion algorithm was applied to estimate the defect profile for the test sample. $3D$ cross sections of the predicted depth profiles at different resolution levels along with the true defect profiles were presented.

Above described was only some major work published on machine learning aspects of MFL signals. Up to the best knowledge of the author, literature lacks the use of Bayesian frameworks such as Gaussian processes for MFL signal interpretation. A close form solution is not achievable due to the ill-posed nature of the MFL inverse problem. Therefore the defect sizing results contain an uncertainty associated and GP is capable of producing the associated uncertainty with each prediction. Indication of the uncertainty for a given prediction aids the asset maintenance process which is a target application of this study. Concerning these advantages later work in this thesis focuses on developing a GP based data driven machine learning framework to interpret MFL signals (Chapter 4).

Following up the GP based inference result, in this thesis an iterative coarse to fine approach have been developed to further refine the interpretation. The inversion process for any forward model can be formulated as an optimisation problem, when it is not straight forward. One of the popular methods is stochastic or deterministic optimisation [39]. Deterministic optimisation methods [40, 41] use gradient information to minimise the mismatch between the model prediction and actual measurements. These methods arrive to a convergence rapidly but it is not guaranteed to be the global optima. For global optimisation, computation intensive and exhaustive stochastic methods may be used. These algorithms search over the full parameter space which involves extensive forward model evaluations. The end result has a much higher chance of landing at the global optima of the desired parameters [42, 43].

Ravan *et al.* [44] used partially $3D$ FEM and fast analytical models for reconstruction of simulated $2D$ defect depth profiles with 5 degrees of freedom. Amineh*et al.* estimate two parameters of rectangular cracks using similar inversion techniques. Both references report direct optimisation time with the FEM models alone to be 20 to 40 hours and required about 40 to 150 iterations [45]. Hari *et al.* [42] used a genetic algorithm (GA) which optimised a $2D$ FEM model for arbitrary defect reconstruction. They reported to take only 20s for a reduced order FEM model of size $N_{FEM} = 950$, but total number of evaluations required for convergence is not given.

Recent work by Priewald*et al.* [39] used a full scale non linear FEM model for fast reconstruction of arbitrary surface breaking corrosion defect geometries in steel plates. The inverse algorithm was formulated in a similar way to that suggested by Yan [46]. A fully analytical expression to efficiently compute the required Jacobian of the inverse MFL problem for the non linear magneto-static case was derived. This framework exhibited fast convergence and efficient computation times. Tuning the parameter vector was controlled but the optimisation algorithm depended on the current mismatch between the model prediction and the reference signals. Due to the ill-posed nature of the MFL inverse problem, some extra information was used in the form of regularisation constraints [47, 48]. Priewald conducted the evaluation of the proposed method only on $2D$ simulated data but did not include any experimental results.

It was noticed that most of these studies were based on highly simplified forward models. Use of FEA models in the inversion process has a few advantages. FEA models generate a more realistic MFL signal due to consideration of eddy current effects, edge effects, non-linearity of materials and other real-life imperfections. Moreover by using the real CI pipe profiles, the multidimensional inversion problem can be further simplified. It was identified that the literature lacks published work in these avenues and this shortfall will be addressed later in this thesis.

2.3 Error sources affecting MFL signal interpretation

Experimental real life MFL signals contain a significant amount of noise. Han Wenhua [4] presented a modified wavelet transform based adaptive FIR filtering algorithm for removing the seamless pipe noise (SPN) in the MFL data. The SPN is an artefact in the MFL data caused by the helical nature of the grain of the seamless pipe. The SPN is time-varying and thereby requires an adaptive filter to mitigate its affect [49]. An adaptive filter is capable of adjusting its impulse response appropriately to minimise the error between the filter output and the reference input. A finite impulse response (FIR) filter was utilised to implement the adaptive system. The FIR coefficients were estimated using the least mean squared (LMS). The idea underlying the approach was to exploit the correlation properties of the MFL signal generated by the seamless pipe and the signals due to defects and other artefacts in the pipeline. They modified the wavelet transform domain adaptive FIR filtering algorithm introduced by Hosur [50] such that it can be applied to remove the SPN in the MFL data.The schematic of the modified wavelet transform domain adaptive SPN cancellation system is shown in Figure 2.3.

Unlike the time domain adaptive filtering method, where the $K+1$ consecutive samples from the reference input $u(k)$ were used as the input, the proposed method applied the discrete wavelet transform (DWT) [51] to the $K+1$ consecutive samples of $u(k)$ before being used as the input of the FIR filter. Just as the time domain adaptive filtering algorithm for removing the SPN, the wavelet transform domain adaptive system cancelled

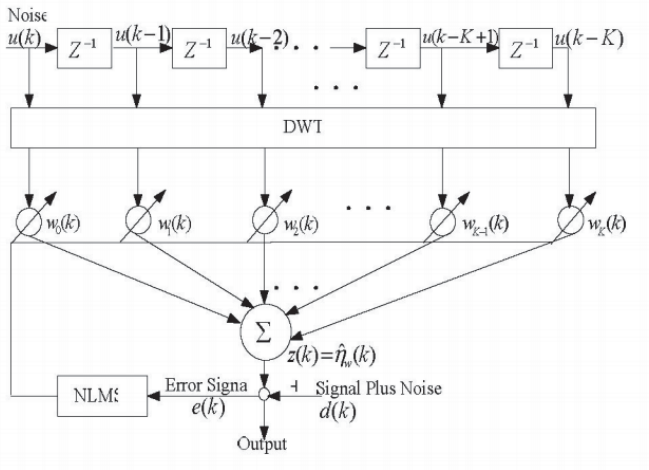

FIGURE 2.3: Wavelet transform domain adaptive SPN algorithm [4]

out the correlated SPN, but still contained the system noise. This noise was treated as an additive white Gaussian noise (AWGN), and therefore was removed using the wavelet shrinkage de-noising method.

For testing their method they used MFL data provided by the material assessment research group in the Department of Electrical and Computer Engineering of Michigan State University. According to the results as shown in Figure 2.4 the modified algorithm had good performance and considerably improved the detectability of the defect signals in the MFL data. Use of these kinds of noise suppression schemes aids in a better detection and interpretation of the defects in MFL data.

The analysis of the MFL signal is however fraught with problems associated with the signal itself such as sensor velocity and permeability variations of the test specimen. Out of these, inspection speed is a major factor. As mentioned, one of the main advantages of the MFL technology is the ability to automate the inspection process. Therefore the effect of inspection speeds needed to be fully investigated.

Yong Li *et al.* [52] presented numerical simulations carried out using ANSOFT Maxwell EM on eddy currents in steel specimens due to a moving probe. Moreover, they studied the effect on MFL signals from a high speed MFL inspection system. In MFL inspection systems, eddy currents were generated because of the travelling probe. The influence of eddy

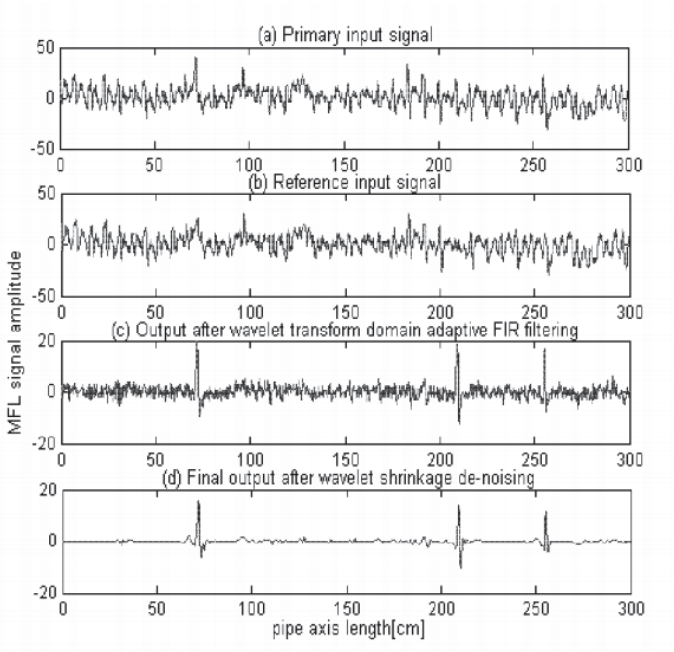

FIGURE 2.4: Wavelet transform domain adaptive SPN algorithm [4]

currents on MFL signal involves not only the shape but also the magnitude of the measured signal. As the probe speed increased, the signal magnitude dropped, which resulted in low signal-to-noise ratio in practical inspection systems. In addition to that, in high-speed MFL inspection systems, it was necessary to apply the noise suppression techniques to cripple systematic noise and extraneous noise. Compared to a static MFL inspection system, a high-speed MFL inspection system required more sophisticated techniques to process signals, such as adaptive filter and algorithms and wavelet analysis.

They also discussed the electronic complexity of high speed MFL equipment. Since the inspection system runs at high velocity, the signal acquisition time should be shortened. Therefore, the instrumentation of signal acquisition should have high sampling frequency and comply with Nyquist law. Moreover the sensor array in high-speed MFL inspection systems is required to have high bandwidth in order to ensure fast response to an instantaneous magnetic field change.

The other main phenomenon affecting the leakage field is the permeability variations in the material. S. Mandayam *et al.* [53] mainly focused on the effects of permeability variations to the output signal. They also considered inspection velocity variations as well and proposed invariant schemes for each of those scenarios. They presented the comparison of the

original signals and the signals obtained using the permeability invariance algorithm. The proposed framework was applied on velocity affected MFL signals arising from different defect dimensions. The velocity invariance scheme examined the underlying signal statistics to construct a restoration filter. This scheme required the value of the undesirable parameter as an input to the algorithm. However they demonstrated the restored signals with respect to the original with promising results.

MFL signals are also contaminated by mechanical vibration noise [54]. This effect is mainly observed in internal pigging tools due to heavy equipment travelling with the sensors [55]. Liang Chen *et al.* modelled these type of noise as additive white Gaussian noise. He suggested Ensemble Empirical Mode Decomposition (EEMD) de-noising method which is a fully data driven method. But as Tan Shi *et al.* presented [55], vibration noises are significant in pigging tools. This work focuses on external hand held MFL set-ups and vibration based noises created in large diameter critical water mains by these type of tools are negligible [55].

It was investigated that the stress applied on the test substances affects the MFL signal. Mandal and Therton [56] experimentally studied the effect of hoop stress on MFL signals of a pit defect. They presented that circumferential hoop stress, which can be generated by line pressure in oil and gas pipelines whilst they are in service, can affect magnetic flux-leakage signals. In their experiment they used a magnetiser containing high strength permanent magnets which generated an axial magnetic field in the pipe wall. To generate the hoop stress, a pressure vessel was artificially created by pumping hydraulic fluid into the chamber. Radial and axial MFL signals of an electrochemically milled pit (50% penetration) were measured on the hydraulic pressure vessel at several hoop stresses. Observed changes in leakage flux signals due to the application of external stress were mainly due to the changes in magnetic anisotropy and hence changes in magnetic surface polarity on the bounding surfaces. In the case of pipes for which the magnetic excitation is axial, application of hoop stress reduced the MFL signal magnitude. They also observed that a considerable increase in MFL signal occurs beyond a certain value of the pipe wall flux density. They claimed that the developed theoretical models fit the experimental MFL data well. The leakage fluxes at various stresses were scaled to make them stress independent in order to avoid the uncertainty due to applied stress when sizing the defects.

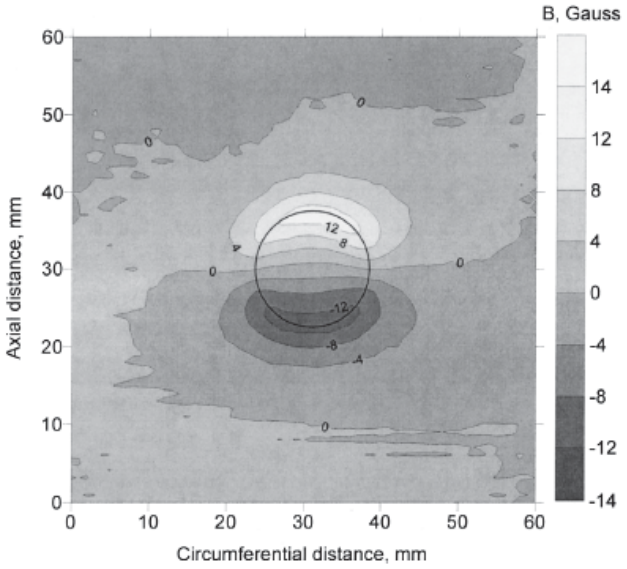

FIGURE 2.5: Contour map of radial residual magnetic leakage flux [5]

They conclude that the MFL magnitude decreases as hoop stress increases within a certain range. However there was no influence on the shape of the MFL foot print, by the hoop stress.

Residual magnetic flux leakage technology

Residual magnetisation is a variation of the ordinary MFL technique. In this technique a strong magnet is passed over the test substance and it is then immediately scanned for residual magnetisation. Few studies are available on the residual magnetisation MFL signal to investigate the possibility to provide useful information about defect size and shape. Since the signal strength is very low, it appears that these studies were channelling which involved very sensitive sensors.

Although the residual flux leakage signals get further decayed at high pressures, the technique still can be used to obtain reasonably useful information about the defects. However, the technique involves the use of sensitive probes to detect the weak remaining magnetic field, which is generally about one tenth of the strength of the active MFL. An earlier study of samples magnetised by strong electric currents revealed that the residual flux

patterns are basically similar to the active flux patterns. However, the magnitudes were very weak and may have opposite magnetic polarity in comparison to active MFL [57]. The opposite polarity occurs only when the excitation current is low, whereas for high excitations, there is no reversal of polarity. A finite element modelling technique has been proposed by Satish [58] to predict the reversal of the residual leakage field.

Vijay Babbar [5] claim that the residual MFL technique with end lift-off method appears to be very promising to provide useful information about defect geometry. They used three simulated defects in the study: a circular blind hole, a blind racetrack-shaped defect, and a gouge. The first two defects were produced on the surface of a hydraulic pressure vessel and were nearly 50% of the wall thickness. After the three magnetisation cycles, a computer controlled Hall probe was moved smoothly over the surface of defects in a two-dimensional grid obtaining surface and contour maps. They used these contour maps to interpret the size and shape of the defect (see Figure 2.5).

They used a straight forward approach to interpret the size and shape. Contour plots were interpreted as the shape of the defect. They also compared signals by lifting the magnet perpendicularly and also by moving the magnetiser to the end of a section and on to a cylindrical platform (end lift-off method).

The literature lacks a systematic study of lift-off. Lift off is the radial distance between the surface of the pipe specimen and the sensor which measures MFL. It is widely known that increasing the lift-off decrease the MFL signal amplitude. However, the influences of the lift-off on defect characterisation are not well documented in literature and is studied in this thesis in Section 4.2.2.

2.4 Chapter Conclusions

This chapter reviewed published work on MFL inspection techniques and inversion methods and clarified the necessity of a complete framework for interpretation of experimental MFL data of cast iron pipes. First various mathematical modelling techniques for MFL phenomenon were reviewed which also included a variety of MFL sensor architectures. Having models for MFL enabled researchers to study the behaviour of the leakage field

in the presence of various defect types. Most of these studies considered parameterised defects which is far from the reality.

When it comes to real life defect types, parameterisation becomes challenging. Researchers tend to use FEA based models in real life defects to overcome these challenges; existing work towards FEA modelling was presented next.

General inverse modelling techniques and customising them for the target application was reviewed followed by more sophisticated data driven machine learning techniques. Recent research on refining MFL interpretations using global optimisation techniques were presented. Most of these frameworks lacked the uncertainty indication of predictions which aids the decision making of asset maintenance. Approximated ellipsoidal defects also aids the asset maintaining by indicating the stress based failure modes. Up to the best of the authors knowledge there is no published work on the use of optimisation approaches to approximate ellipsoidal defects using MFL data.

Various noise sources in the MFL process distort the MFL signal results in erroneous interpretations. Application-specific signal conditioning and noise suppression techniques were reviewed while discussing the importance of distortion free signal processing. Other sources of error in MFL interpretations, such as scanning speed and permeability variations were studied followed by a review on speed and permeability invariant schemes. Residual magnetisation was identified as a variation of the ordinary MFL technique.

Published studies were found to be limited towards generalisation of detailed MFL signal interpretations using real life MFL data. Moreover ellipsoidal approximation of defects which have a major effect on structural integrity of metal pipes was absent in literature. Not only isolated defects but also the thickness profiles could be reconstructed using MFL data. The use of FEA models in iterative optimisation algorithms to solve the inverse problem can achieve real-life corrosion profiles. These identified shortcomings in the current MFL techniques and published studies will be addressed in the following chapters.

Chapter 3

Development of a Realistic MFL Model and a Semi-Automated MFL Set-up

3.1 Introduction

The MFL tool and its parameters play a crucial role in solving the inverse problem of interpreting remaining wall thickness. Although the underlying concept of magnetic flux leakage is common for MFL tool design, excitation field strength, type of sensors, shape of the yoke, the shoes and many other tool specific parameters affect the measurement. Moreover in practice, similar to any other experiment, the measurements are corrupted by various noise sources. Therefore it is almost impossible to experimentally capture the effects of MFL signals over various defect scenarios. This raises the need of having a well calibrated model of the MFL phenomenon so that various parametric changes and defect scenarios can be studied.

Modelling and analysing magnetic flux leakage has been a focus of researchers for more than three decades. Zatsepin and Shcherbinin [26] modelled the leakage field from infinitely long surface-breaking cracks considering a point dipole, linear dipole or strip dipole in terms of magnetic charges induced by the external magnetic field on the bounding surfaces of

the cracks. Later Shcherbinin and Pashagin [27] developed a more sophisticated model extending the previous work into cracks with finite dimensions. This study was the basis for most of the work published later on the interaction between the defects and the leakage field.

Forster [2] analytically described the magnetic flux leakage phenomenon. He claimed that for better understanding of the magnetic flux leakage phenomenon the determination of the magnetic field strength inside the defect as a function of defect geometry, the magnetic properties of the material, and the applied field strength are essential. Minkov et al. [32] applied the dipolar model to single flows of irregular cross sections by considering the defect filled with magnetic dipoles aligned parallel to the excitation field, each dipole having a strength directly proportional to the defect depth. They proposed a method for estimating the sizes of surface cracks in magnetic materials based on applying a magnetic field, determining the leakage magnetic field in the vicinity of a crack by moving a Hall element along one or two scanning lines crossing the crack on the surface of the material, and measuring the corresponding Hall voltage distribution. However, most of these methods are limited to well parametrised defects.

When solving the inverse problem of MFL phenomenon, data driven approaches are well suited due to the complexity of the problem [37], [36]. A good quality data-set capturing a wide range of defect scenarios is the first step for a successful data driven inverse model. Some work have been done on experimental data using in-line MFL tools that employ modern magnetic sensors for MFL measurements and IMUs for localisation [49] [53]. These techniques use inline tools and therefore the service needs to be disturbed. These tools are extremely heavy, bulky and are very expensive to operate. Even though the data could be collected, getting the groundtruth over kilometres becomes a prohibitive process.

The underlying MFL phenomenon can be extensively captured using a validated simulation model. Due to the high demand of a validated forward model, the focus of this chapter is on developing a realistic computer based model for MFL phenomenon. It first derives a dipole based parametric analytical model. Due to its parametric limitations, a finite element analysis based model was developed and the signals were compared against each other with a good agreement. Once the simulation models were validated using the analytical

model, it raises the need to experimentally validate the models too. Later in this chapter the development of an semi-automated experimental MFL tool is discussed. This tool has been used to collect data on calibration defects machined on flat plates as well as on aged cast iron water pipes exhumed after service. These experimental calibration measurements are used to validate the simulation models developed earlier.

This discussion continues in Chapter 4 where data driven inverse models are developed using the simulated data and employed in interpreting experimental measurements.

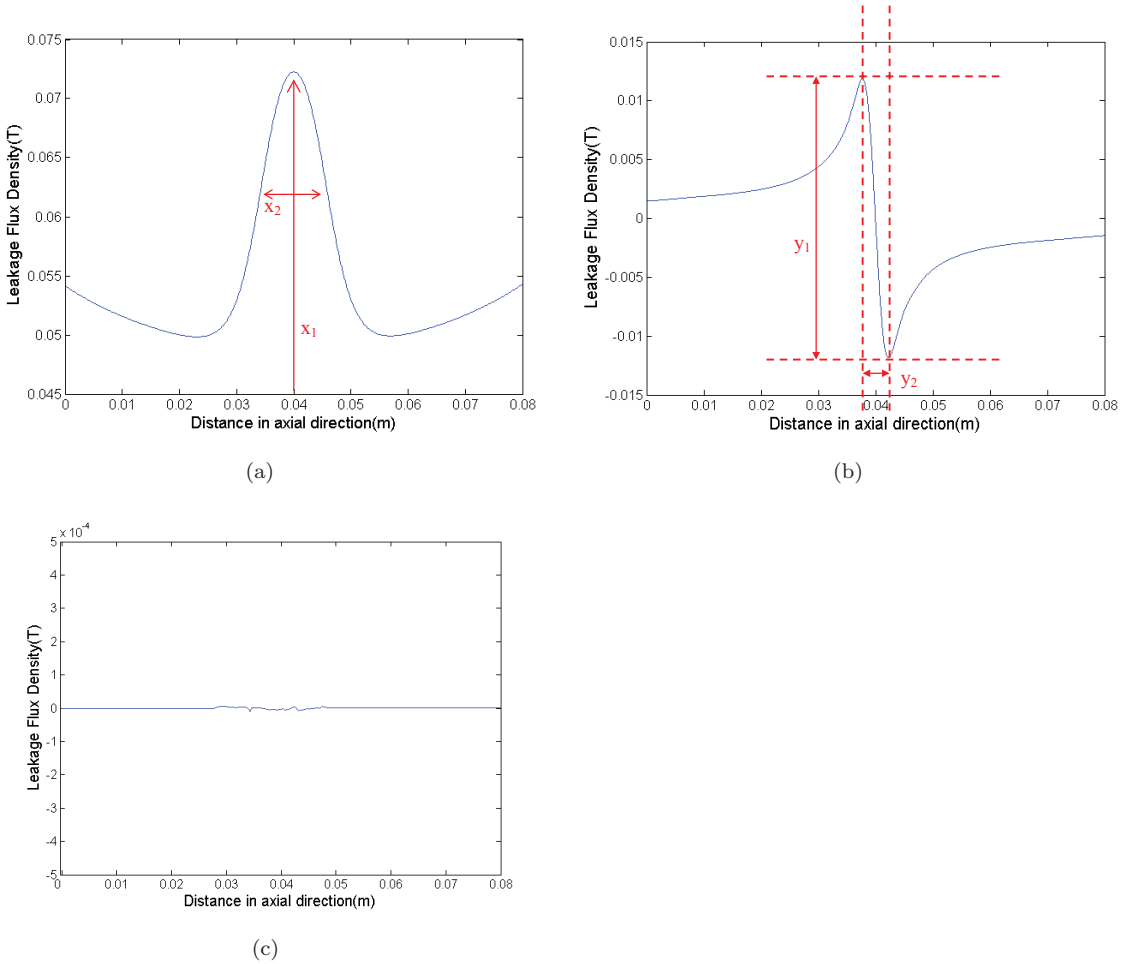

FIGURE 3.1: Three components of an MFL signal scanned along the pipe axis: (a) Axial component (X component), (b) Radial (Y component), (c) Tangential component.

A MFL signal of a pipe can be decomposed into three components, namely axial (X component), radial (Y component) and tangential. An example of these signals for a simple circular defect is shown in Figure 3.1. The tangential component of the leakage magnetic

field vanishes due to the very high axial excitation magnetic field. In the presence of a simple defect, when the flux leakage starts to appear, both axial and radial components get their own shape. It is observed that both of these components carry redundant information about the depth and width of a defect. When the depth of the defect is increased, the peak magnitude of the X component (x_1 of Figure 3.1(a)) as well as difference of peak magnitudes of Y component (y_1 of Figure 3.1(b)), increased. Similarly when the width/diameter of a defect is increased both x_2 of Figure 3.1(b) and y_2 of Figure 3.1(b), increased. Moreover most industrial tools including the one used in this work measure only the x competent. Therefore the scope of this thesis is limited to analysing the axial component (X component) of the magnetic leakage field.

3.2 MFL Analytical Model

A dipole based analytical model has been derived to parameterise the Magnetic flux leakage phenomenon. This model analytically calculates the leakage field distribution around the defined anomaly. This well established dipole modelling technique [33, 59] has been used as a basis for comparisons through out the thesis. Fully understanding the analytical model is important because it is later used to compare and validate computer based FEA simulation models as well as experimental MFL lab set-up. The model is also utilised in the Chapter 5 for developing analytical model-aided optimisation in the ellipsoidal defect approximation framework.

As discussed in the previous chapter, MFL technique consists of magnetising the material, and detecting any defect induced magnetic leakage flux using appropriate sensors. When a corrosion pit is located in a strong background magnetic field, it acts as a region of high magnetic reluctance. This makes the majority of the magnetic flux lines divert in a different path to avoid the high reluctance area, which is around the defect. This results in generating opposite magnetic polarities, or a dipolar magnetic charge (DMC) on the defect walls of opposite sides of the defect [60] [33].

For the following derivation, it is assumed that a dipolar magnetic charge (DMC) is developed on the defect faces intersecting the exciting magnetic field as a result of its interaction

with the excitation field. Moreover, effects of variations in magnetisation and permeability of the material are minimised by assuming high magnetic excitation, corresponding to the saturation region of the material.

The model also assumes that the eddy currents, which occur in the conductive steel due to the relative motion to the strong magnetic fields, can be neglected. This is a reasonable assumption as long as the MFL tool operates at very low velocities [61]. Also it is to be stated that there are stray magnetism, stress, temperature etc which can influence the leakage flux which is very minimal in the order of magnitudes we are considering, so are also neglected[39].

There are few additional assumptions made for this derivation. It has truncated the infinite domain Ω^{∞} at a finite distance sufficiently far from the region of interest (ROI) and created the model domain $\Omega \subset \Omega^{\infty}$. Its also considered that $\Omega = \Omega_0 \cup \Omega_{st}$ to consist of two homogeneous materials. Air in Ω_0 with absolute permeability $\mu = \mu_0$ and a linear steel material in Ω_{st} with absolute permeability $\mu = \mu_0 \mu_{rs}$.

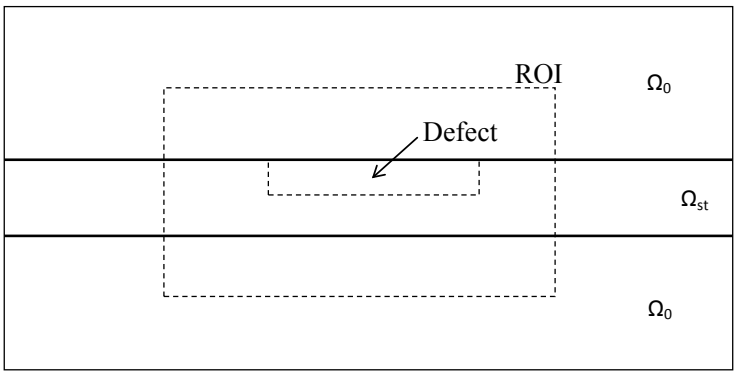

FIGURE 3.2: A defect and its surrounding space

Further simplifications have been used in excitation method as well. As described in Chapter 2, usually in MFL, the magnetisation unit consists of a U shaped yoke with an electro magnet due to practical reasons. A permanent magnet is also used in some scenarios and the sole purpose of this is to magnetise the test material. In this model, this U shaped magnetisation unit is ignored from the modelling process and replaced with a homogeneous magnetic field parallel to the test substance [41, 45, 62]. This allows the

forward model to have a constant magnetic charge density in the wall of the defect, as there is no yoke which can interfere.

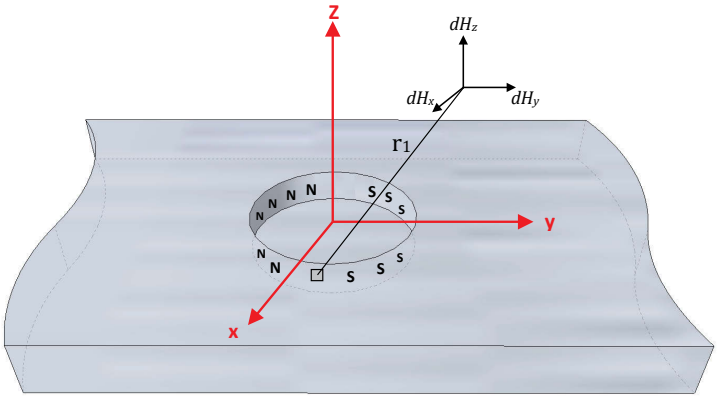

FIGURE 3.3: Dipolar magnetic charge model for a cylindrical defect

A cylindrical defect has been considered with its longitudinal axis (z-direction) perpendicular to the applied magnetic field (y-direction), as schematically represented in Figure 3.3. The magnetic field lines diverge around the low permeability flaw, inducing a DMC on the walls of the cylinder. The surface of the test substance is defined by the xy plane at $z = 0$, with the top area of the cylindrical defect centre at $(0, 0, 0)$, and its bottom area centred at $(0, 0, -b_1)$, where b_1 is the depth of the defect. The MFL signal induced by the type of defect just described is sampled in the region $z > 0$.

Half of the cylindrical defect develops a north polarity or positive magnetic charge density, $+\sigma$, while the other half develops a south polarity or negative magnetic charge density $-\sigma$. The cylindrical defect has a radius of R_1. The angle θ_1 is measured from the positive y direction to an element of magnetic charge, dp_1. The differential element of charge at the defect, dp_1, has coordinates $(R_1 sin\theta_1, R_1 cos\theta_1, z_1)$ and a charge proportional to its area.Therefore,

$$dp_1 = \mu_0.\mu_{rs}\sigma R_1 d\theta_1 dz_1 \tag{3.1}$$

Now, the magnetic field (dH_1) generated at a distance $\mathbf{r_1}$ by this element of charge dp_1 is given by,

$$dH_1 = \frac{dp}{4\pi|r_1|^3}.\mathbf{r_1} \tag{3.2}$$

Lets consider the positive polarity side H^+ of the defect. The axial component of the field at a distance r_{1+} is given by,

$$dH_y^+ = \frac{\mu_0.\mu_{rs}\sigma R_1 d\theta_1 dz_1}{4\pi|r_1^+|^3}\left(y + R_1 sin\theta_1\right) \tag{3.3}$$

where,

$$r_1^+ = \sqrt{(x - R_i cos\theta_1)^2 + (y + R_i sin\theta_1)^2 + (h - z_1)^2} \tag{3.4}$$

The y component of the leakage field, dH_y^+, vanishes due to the symmetry. The Equation 3.3 is integrated over θ_1 from 0 to π and over z from $-b1$ ($b1 > 0$) to 0 to determine the total field at r_{1+} due to the positively polarised side of the defect,

$$H_y^+ = \int_0^\pi \int_{-b1}^0 dH_y^+ dz_1 d\theta_1 \tag{3.5}$$

which leads to,

$$H_y^+ = \int_0^\pi \int_{-b1}^0 \frac{\mu_0.\mu_{rs}\sigma R_1(y + R_1 sin\theta_1)}{4\pi\left\{(x - R_1 cos\theta_1)^2 + (y + R_1 sin\theta_1)^2 + (h - z_1)^2\right\}^{\frac{3}{2}}} dz_1 d\theta_1 \tag{3.6}$$

The same approach can be used to calculate the leakage field by the negatively polarised side of the cylinder. The only change is the opposite polarity and an appropriate y coordinate.

The negative polarity side leakage field H^- of the defect is given by,

$$dH_y^- = -\frac{\mu_0.\mu_{rs}\sigma R_1 d\theta_1 dz_1}{4\pi|r_1^-|^3}\,(y - R_1 sin\theta_1) \tag{3.7}$$

where,

$$r_1^- = \sqrt{(x - R_i cos\theta_1)^2 + (y - R_i sin\theta_1)^2 + (h - z_1)^2} \tag{3.8}$$

The limits of the integral are kept the same, since all the angles and distances are measured in the same way as the positive side. Therefore, by using the same integration for the negatively polarised side $H_z^-$of the cylinder the total normal leakage field is given by,

$$H_y^- = \int_0^{\pi}\int_{-b1}^{0} dH_y^- dz_1 d\theta_1 \tag{3.9}$$

which leads to

$$H_y^- = \int_0^{\pi}\int_{-b1}^{0} -\frac{\mu_0.\mu_{rs}\sigma R_1(y - R_1 sin\theta_1)}{4\pi\left\{(x - R_i cos\theta_1)^2 + (y - R_i sin\theta_1)^2 + (h - z_1)^2\right\}^{\frac{3}{2}}} dz_1 d\theta_1 \tag{3.10}$$

Now the total leakage field is given by the addition of the positive and negative side fields.

$$dH_y = dH_z^+ + dH_z^- \tag{3.11}$$

After the integration over the entire charged surface, the total field is given by, (adding 3.6 and 3.10)

$$H_y = H_z^+ + H_z^- \tag{3.12}$$

The analytical model was implemented in MATLAB 8.2.0 and was used to compute leakage field for a given defect. Figure 3.4 shows the 3D the leakage field on a cylindrical defect.

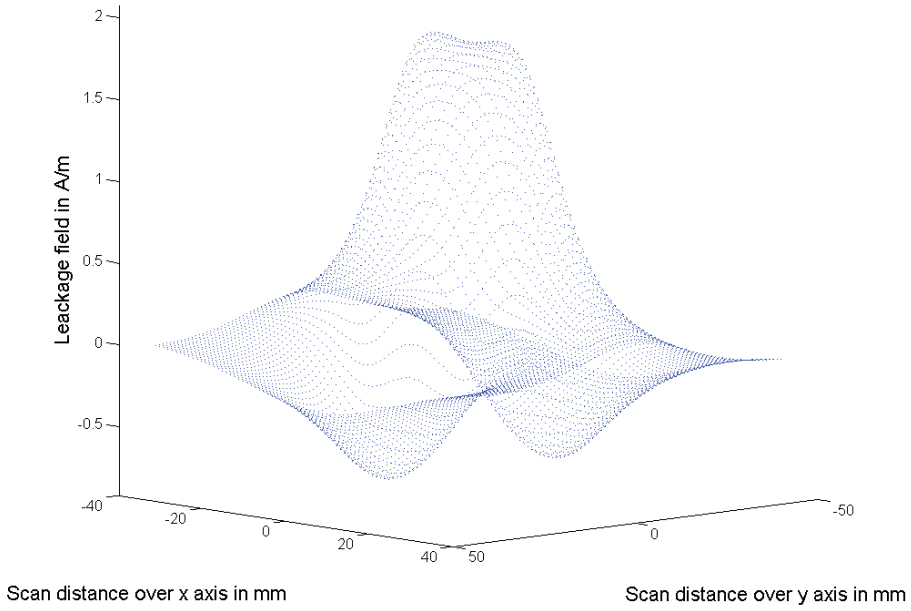

FIGURE 3.4: 3D Magnetic flux Leakage field of a cylindrical defect

As per the assumptions made, analytical model is limited to well parametrised defects. It is not applicable for complex defect shapes unless an approximation is used. This raised the need of having a model which can account for realistic defect shapes and other tool specific parameters. It was decided to use a validated FEA model, which can simulate much more complex and realistic defect shapes that are found on aged water pipes which is the main focus of the research project. Once the analytical model is giving a reasonable representation of the leakage field of a cylindrical defect, an identical defect was simulated using Finite Element Analysis (FEA) software. Section 3.3 describes the development of a FEA simulation model.

3.3 Finite Element Analysis Model

As described having a FEA model becomes crucial when it comes to simulate realistic defect shapes due to the limitations in the analytical model. Moreover, having an exhaustive

data set, capturing vast variety of defects is essential to learn the inverse models described in the next chapter. It is also obvious that generating a dataset experimentally using the experimental set up is exhaustive and prohibitive. Therefore we employ a computer based simulation software to simulate the output of a MFL tool.

3.3.1 Introduction

Finite Element Analysis (FEA) was initially introduced in the early 40's by R. Courant, who used numerical methods to obtain approximate solutions to vibration systems [63] . With this introduction of numerical analysis of physical scenarios, researchers started to use these methods in solving various problems.

FEA generally analyses a computer based model of a physical system for a set of specific properties. These methods are widely used in modern product design and existing product refinement. Especially with the modern computation power, designers have been able to simulate the actual functionality of a product even before it is manufactured. This method enables the simulation of physical properties that are even impossible to measure experimentally. For example a magnetic field strength inside a metallic object.

FEA uses a complex system of points (nodes) which make a grid (mesh) (see Figure 3.10). This mesh is programmed to contain the material and structural properties which define how the structure will react to certain physical excitations. Nodes are assigned at a certain density throughout the material depending on the required level of details as the result. Selected regions can have a higher node density to gain highly detailed information where as less critical areas can have a lesser node density to keep the computations simpler and faster. The mesh acts like a spider web where from each node a mesh element extends to each of the adjacent nodes. This web of vectors is what carries the material properties of the object, creating a web of elements. A simplified $2-D$ illustration of this framework is shown in Figure 3.5.

For a first order element as shown in Figure 3.5, any physical property varies within the triangle. When a given property varies linearly with the distance, it can be formulated in general as,

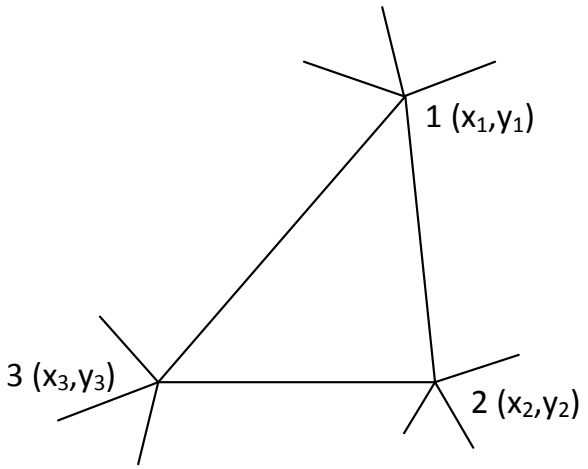

FIGURE 3.5: A single element in a $2D$ mesh

$$V(x,y) = a_1 + a_2 x + a_3 y \tag{3.13}$$

This relation applies to all the nodes in the mesh. For the three nodes in Figure 3.5 ,

$$V_1 = a_1 + a_2 x_1 + a_3 y_1 \tag{3.14}$$

$$V_2 = a_1 + a_2 x_2 + a_3 y_2 \tag{3.15}$$

$$V_3 = a_1 + a_2 x_3 + a_3 y_3 \tag{3.16}$$

Using these three equations, it is apparent that we can determine the values of a_1, a_2, and a_3 as,

$$a_1 = \frac{1}{D} \begin{vmatrix} V_1 & x_1 & y_1 \\ V_2 & x_2 & y_2 \\ V_3 & x_3 & y_3 \end{vmatrix} \tag{3.17}$$

Similarly,

$$a_2 = \frac{1}{D}\begin{vmatrix} 1 & V_1 & y_1 \\ 1 & V_2 & y_2 \\ 1 & V_3 & y_3 \end{vmatrix} \tag{3.18}$$

$$a_3 = \frac{1}{D}\begin{vmatrix} 1 & x_1 & V_1 \\ 1 & x_2 & V_2 \\ 1 & x_3 & V_3 \end{vmatrix} \tag{3.19}$$

where,

$$D = \frac{1}{D}\begin{vmatrix} 1 & x_1 & y_1 \\ 1 & x_2 & y_2 \\ 1 & x_3 & y_3 \end{vmatrix} \tag{3.20}$$

Now by substituting values a_1,a_2 and a_3 in Equation 3.13 gives,

$$V(x,y) = \sum_{i=0}^{3} \frac{1}{D}\left(p_i + q_i x + r_i y\right) V_i \tag{3.21}$$

where,

$$p_i = x_2 y_3 - x_3 y_2 \qquad q_1 = y_2 - y_3 \qquad r_1 = x_3 - x_2 \tag{3.22}$$

and the remaining terms are obtained by cyclical permutation of the indices. To proceed further after this point, we need to specify the physical properties we are calculating for. An electro magnetic problem is considered as an example. When E is in vector form, $E = -gradV$ and we have ,

$$E = iE_x + jE - y = -i\frac{\partial V}{\partial x} - j\frac{\partial V}{\partial y} \tag{3.23}$$

By using Equation 3.21 we have,

$$E = -gradV = -i\frac{1}{D}\left(q_1 V_1 + q_2 V_2 + q_3 V_3\right) - j\frac{1}{D}\left(r_1 V_1 + r_2 V_2 + r_3 V_3\right) \tag{3.24}$$

The main difference between a closed form solution and a FEA based solution is that FEA is an approximation. When substituting the answer into the original equation, it generates a residual R. In the above scenario,

$$div\,(\epsilon gradV) + \rho = R \tag{3.25}$$

The idea is to numerically force R to be zero using the following operation. The accuracy of the result depends on the termination criteria. In the work described in this chapter, the relative tolerance has been set to 0.1%.

$$\int_{\Omega} W[div\,(\epsilon gradV) + \rho] = 0 \tag{3.26}$$

where W is a weighting function and Ω represents the domain in which the condition is enforced. The derivation of the weighting function and the numerical methods to solve the equation 3.25 such as "Galerkin methods" are not described in this chapter and the reader is referred to the book "Electromagnetic Modelling by Finite Element Analysis" [64].

Rather than implementing a complete FEA solution, a well established FEA based simulation software was used to do the simulations. After some research, COMSOL Multiphysics® [65] software was selected for this work. Figure 3.6 shows the basic geometry of the FEA simulation model created using the AC/DC module of COMSOL Multiphysics® [65] software.

3.3.2 Model development using COMSOL Multiphysics® Software

The first step of the COMSOL modelling process is to generate the geometry of a realistic MFL tool. Due to the nature of the research project, the industry partner provided data for the research work. To be able to comply with these data, a similar tool to the industry tool was simulated. Two coils were wound in a U shaped yoke made of soft iron. These coils were used to excite the test substance by injecting magnetic flux.

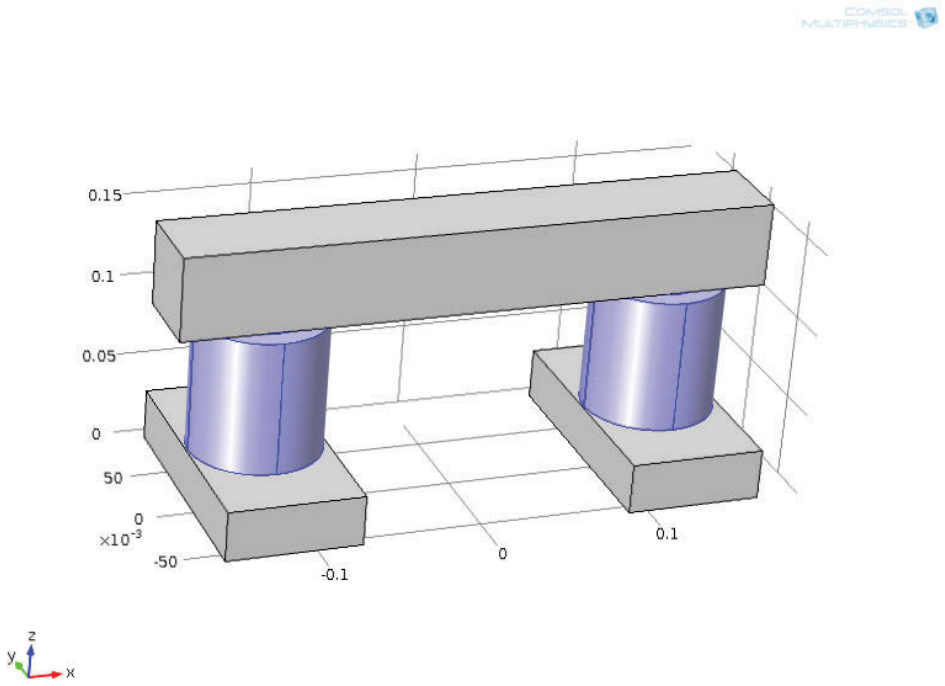

FIGURE 3.6: Basic geometry of the MFL tool

Simulation software required a bounding box as the boundary conditions of the simulation. Therefore a bounding air box was used with a sufficient size, so that it did not affect the magnetic circuit of the tool (See Figure 3.7). On the boundary of the air box it is considered that the magnetic vector potential perpendicular to each surface is zero, which bounds all the flux to be conserved within the air box or in other words, a magnetic insulation. The boundary condition is given by equation,

$$n \times A = 0 \tag{3.27}$$

where A is the magnetic vector potential and n is the normal unit vector to a given surface on the boundary of the air box.

Now the coils need to be excited such that they create a closed magnetic circuit along the U shaped yoke and the test substance. Industry parter uses a design with two separate coils in each leg of the yoke. It is a common design in literature as well [30], [66], [36].

Since both of these coil need to create an accumulated electro-magnetic field on the yoke, they need to be excited accordingly.

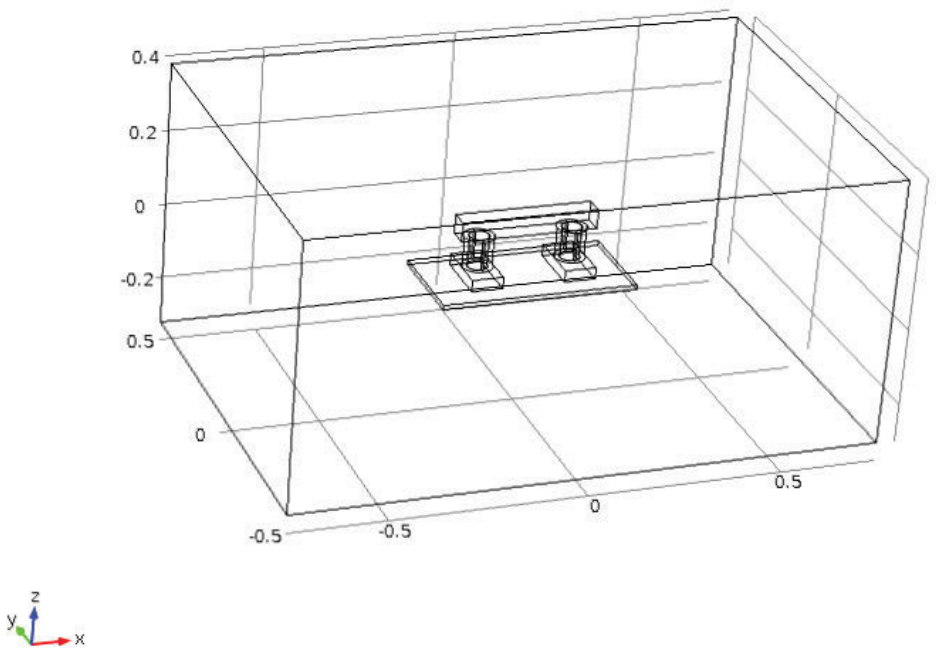

FIGURE 3.7: Boundaries and air box of the FEA simulation

Industry partner's design parameters were considered when deriving equations for the current flow in each coil. For the left coil ($x < 0$), the x component of the current density can be derived as,

$$I_L^x = j_p \frac{y}{\sqrt{(x + 0.12)^2 + y^2}} \tag{3.28}$$

For the same coil, the y component of the current density becomes,

$$I_L^y = -j_p \frac{(x + 0.12)}{\sqrt{(x + 0.12)^2 + y^2}} \tag{3.29}$$

Similarly, for the right hand side coil ($x > 0$) , the x and y components of the current density are given by Equation 3.30 and Equation 3.31 respectively.

$$I_R^x = j_p \frac{-y}{\sqrt{(x-0.12)^2 + y^2}} \tag{3.30}$$

$$I_R^y = j_p \frac{(x-0.12)}{\sqrt{(x-0.12)^2 + y^2}} \tag{3.31}$$

The value of j_p is chosen to match the excitation value of the tool provided by the industry partner. During the FEA simulation, it generates an opposite direction circular current flow in each coil. An arrow surface of the current vector across a section in $x - y$ plane going through the coils is shown in Figure 3.8.

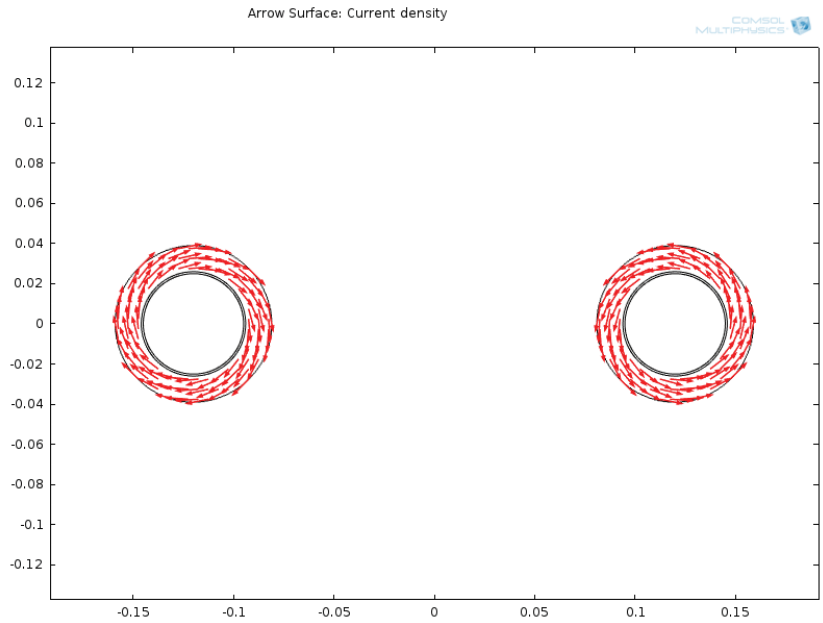

FIGURE 3.8: Arrow surface of current flow in each coil

The model needs to identify materials for each geometry item. This research project is mainly focused on aged gray cast iron pipes used in the water industry. Measuring magnetic properties of the gray cast iron was rather a tedious process. Due to the required accuracy, a superconducting quantum interference device (SQUID) was used to measure the hysteresis loops for different excitation levels. All the hysteresis loops were combined to generate the $B - H$ curve of the pipe material. This is a very sensitive magnetometer,

which can be used to measure magnetic fields with a very high accuracy and it uses a super-conductive material. SQUIDs are very sensitive to measure very small magnetic field values as low as ($\times 10^{-18}T$) and the noise levels are very low. The $B-H$ curve obtained for the gray cast iron pipe is shown in Figure 3.9 .

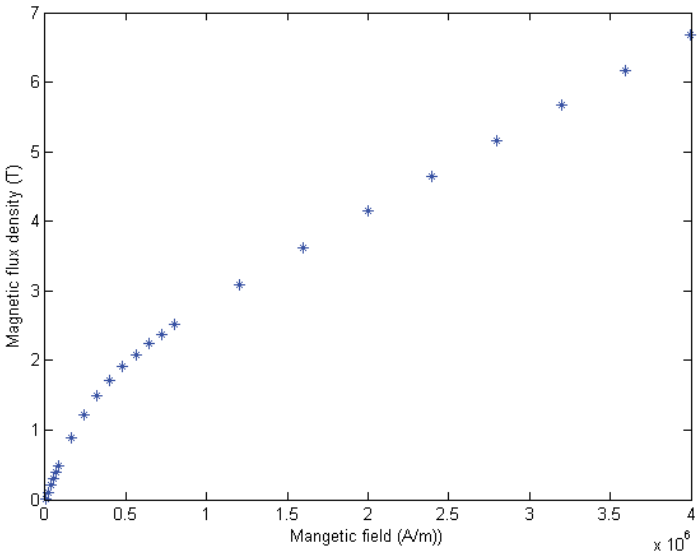

FIGURE 3.9: $B-H$ curve for gray cast iron used in water pipes

Next comes the meshing stage. An unstructured free-tetrahedral mesh was used for this work. These meshes are often used in finite element analysis to discretise a volumetric domain. The current mesh for the model shown in Figure 3.10 contains about 500 000 domain elements.

An experiment was carried out starting from a very coarse mesh to a very fine mesh. For the given model when it comes to about 500 000 elements, the output signal ceases to differ more than $\pm 5\%$. Further fine mesh would give a much finer, high resolution output. However it requires higher computation time.

An array of sensors have been employed to measure the leakage flux placed in the middle of the tool. Once the solution is generated, the software is able to visualise different physical parameters of the model. The flux density distribution over the geometry of the set-up is illustrated in Figure 3.11.

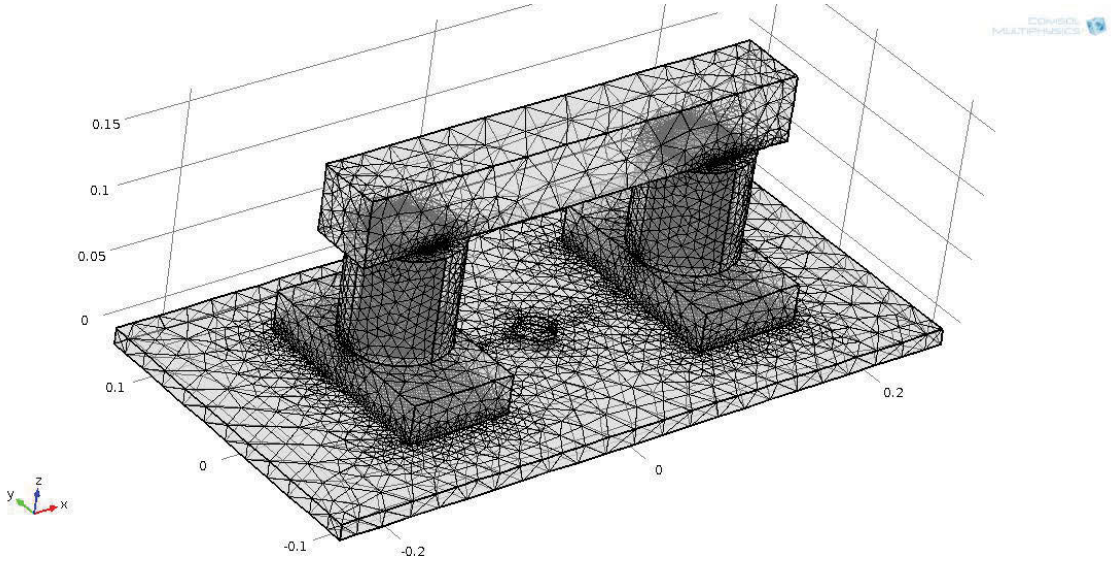

FIGURE 3.10: Free tetrahedral mesh in FEA simulation

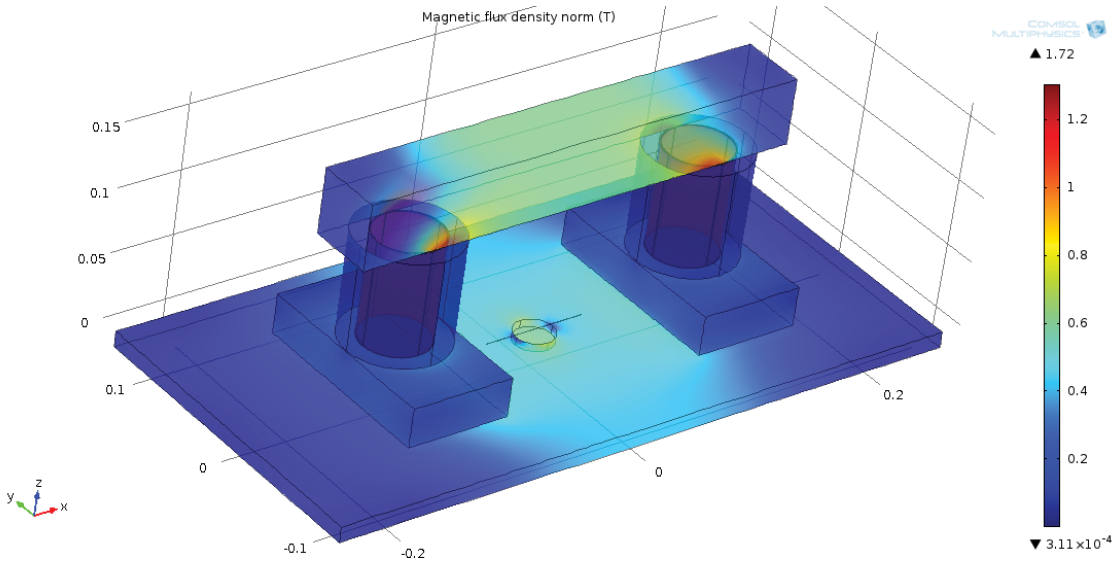

FIGURE 3.11: Flux density distribution over the geometry

Simulation model validation using the analytical results

Once the simulation model was in operation, a preliminary validation step was carried out using the analytical model described in Section 3.2. The analytical model was capable of generating the MFL leakage signals for simple cylindrical defects. Thus, an identical cylindrical defect has been simulated and also analysed using the analytical model for the leakage field. This cylindrical defect had a diameter of 10mm and a depth of 7.5mm on a 30mm thick homogeneous gray cast iron plate. The simulation tool was placed in the

centre line of the defect and moved along. For the analytical model x was set to zero, so the leakage flux along the centre line is calculated. Only $1D$ line scans were simulated to comply with the industry partner's tool, which performs straight line scans. These two results were compared with a 95% agreement between each other. It is observed that the peak values of both curves are very close, but the spread of the curve seems different to each other. This could be due to the further simplification made in the analytical model as opposed to the complex physical interactions considered in FEA simulation. Figure 3.12 shows the two leakage curves generated from each of those methods.

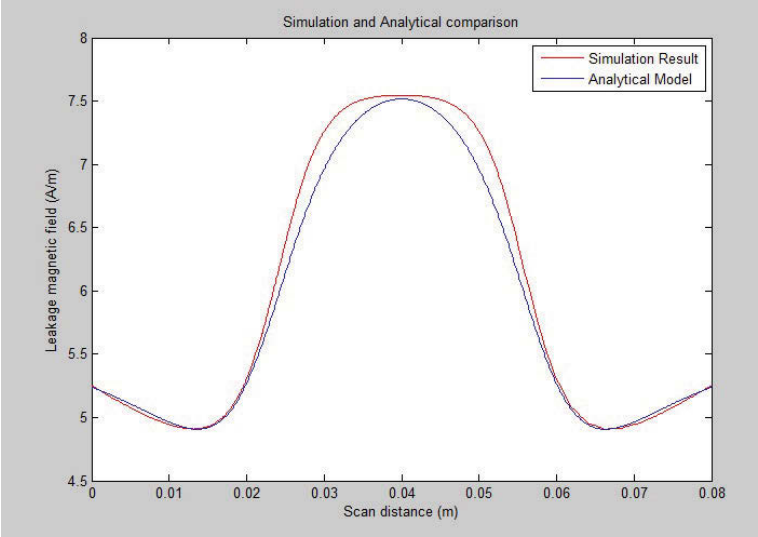

FIGURE 3.12: Comparison of Analytical model and COMSOL Simulation

Not only using the analytical model, but also another simulation software was also employed to the validation process. A similar exercise was carried out with ANSYS simulation software, using identical physical parameters. The resulting signals illustrated a 98.8% agreement between each other. Figure 3.13 shows the comparison between the output signals of the two FEA packages.

3.3.3 Experimental set-up development and fabrication

Once the models were validated using an analytical model and simulation software, it was to be experimentally validated. This raised a need of an experimental MFL set-up. Further, having an experimental tool enables the collection of real measurements for data processing algorithms discussed in subsequent chapters.

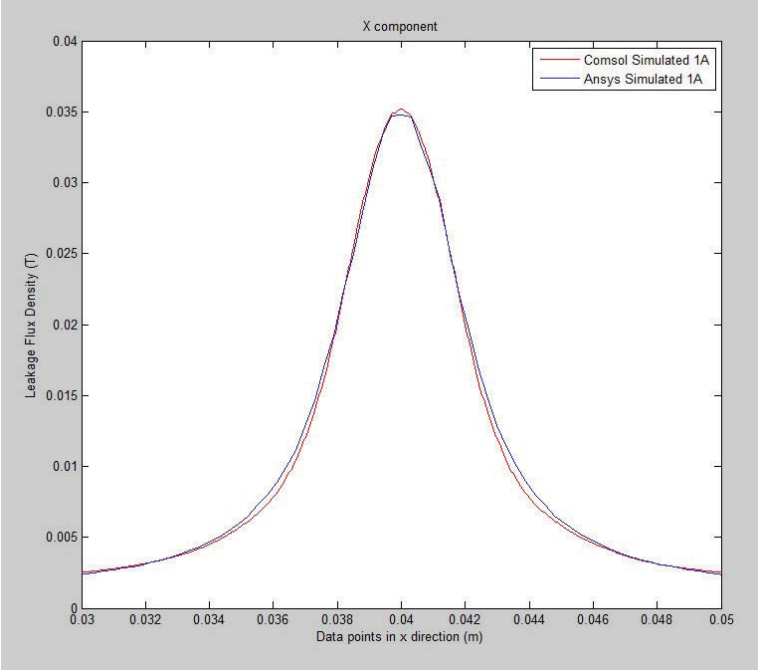

FIGURE 3.13: Comparison of ANSYS and COMSOL simulations

Considering these research requirements, an MFL lab set-up tool was developed. The CAD view of this tool arrangement is shown in Figure 3.20 . This tool was designed to be used on pipes with thicknesses up to $30mm$ and on different ferromagnetic materials.

3.3.3.1 Design parameters of the MFL set-up

The first step of the design process is to calculate the required magnetic flux density on the test substance. A shoe at the end of the yoke has been used to spread the flux to result in a close to homogeneous excitation in the scanning ROI. Figure 3.14 shows the basic CAD design of the set-up.

Gauss's law for magnetism states that [67],

$$\Phi_B = \oint_S BdS = 0 \tag{3.32}$$

where S is any closed surface and dS is a vector, whose magnitude is the area of a tiny piece of the surface S in the direction of the outward surface normal. Φ_B is the net flux of

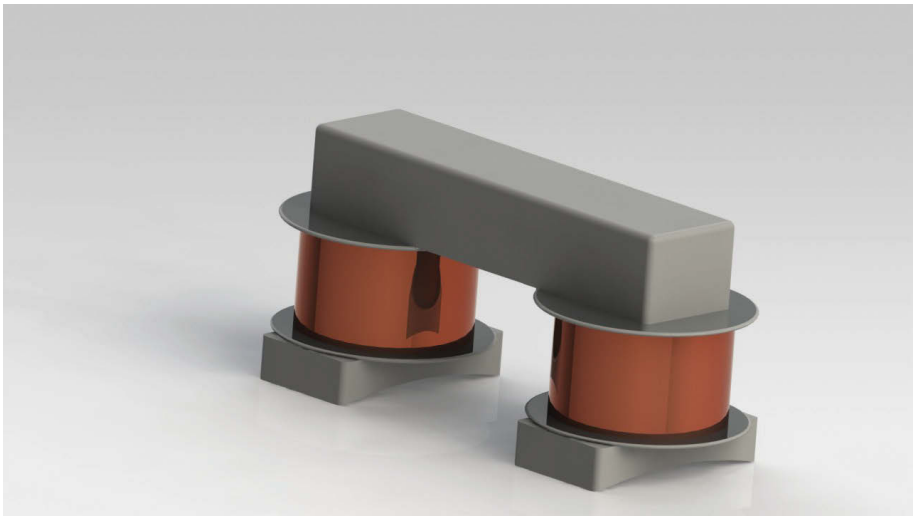

FIGURE 3.14: CAD model of the MFL lab set-up

the magnetic field out of the surface and the Gauss's law states that the surface integral of always zero. In other words flux is conserved over a closed surface.

An instance where the magnetised shoe moves close to the test substance is considered for the simulation. It creates a magnetic footprint on the test material as shown in the simulation (See Figure 3.15).

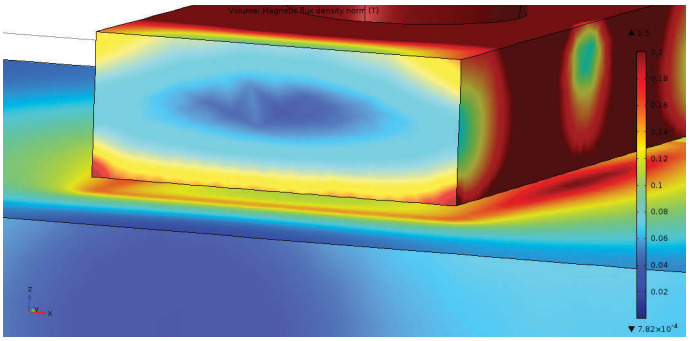

FIGURE 3.15: Magnetic flux density distribution under the shoe

According to the diagram shown in Figure 3.16, consider the magnetic foot print as $ABCDEFGH$, and since it is a closed surface,

$$\Phi_y - \Phi_t - \Phi_o = 0 \tag{3.33}$$

where Φ_y is the magnetic flux coming from the yoke, Φ_t is the flux coupled into the test substance and Φ_o is the non-coupled flux. Given the yoke travels very close to the test substance and the air coupling between two ferromagnetic material it can be assumed that Φ_o is negligible.

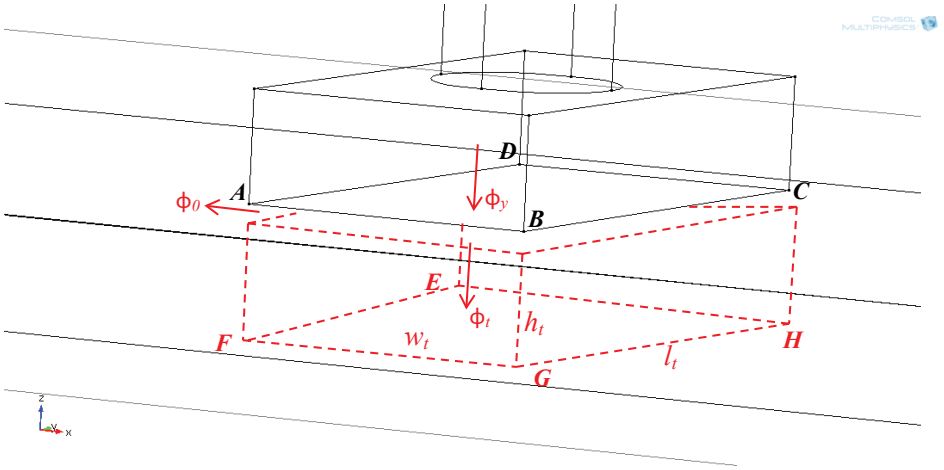

FIGURE 3.16: Magnetic footprint of the shoe

Now if B_y is taken as the total flux density at the shoe, B_t as the flux density inside the test substance and $w_t \times l_t \times h_t$ are dimensions of the foot print just below the shoe,

$$B_y\left(w_t l_t\right) - 2B_t\left(h_t l_t + w_t h_t\right) = 0 \tag{3.34}$$

Therefore the excitation coil combination should create B_y flux density at the end of the shoe. Given a solenoidal coil of length l_c, radius r_c with number of turns N_c carrying a current of I_c , the integral form of Ampere's law states that,

$$\oint_C H dl = \iint_s J_f ds = I_{f,enc} \tag{3.35}$$

where $\oint_C$ is the closed line integral around a closed curve and $I_{f,enc}$ is the free current enclosed in the curve. By substituting the parameters of our solenoidal coil we get,

$$\oint_C H_y dl_c = N_c I_c \tag{3.36}$$

$$H_y l_c = N_c I_c \tag{3.37}$$

From 3.34 we get

$$B_y = \frac{B_t w_t l_t}{w_y l_y} \tag{3.38}$$

From 3.37 we get

$$H_y = \frac{N_c I_c}{l_c} \tag{3.39}$$

Also given the $B - H$ curve of the material we can write (Figure 3.9)

$$B_y \mapsto f(H_y) \tag{3.40}$$

By using the $B - H$ curve for the material and using the Equations 3.34, 3.37 and 3.40, a feasible set of dimensions and other design parameters for the MFL set-up has been calculated.

A hall effect sensor has been placed in the middle of the yoke to read the measurements of the leakage flux. An ARDUINO UNO development board has been used to capture the signals from the sensor and transmit them to a PC. The PC records the signals as the set-up moves along the test substance. Figure 3.17 shows the prototyped MFL set-up along with the controller.

3.3.3.2 Automatic scanning procedure

Currently even on the industry standard, external pipe scanning such as those done on water mains have been performed manually using large, heavy hand held scanners (Figure 3.18). This human intervention results in less accurate measurements and also errors in localisation of the defects. Moreover manually scanning lengths of piping over a prolonged period can be a tedious, time consuming and tiring process for the operator which can also lead to minor injuries such as back soreness due to user bending over for a long period of time. By automating a part of the process it is possible to save time as well as creating

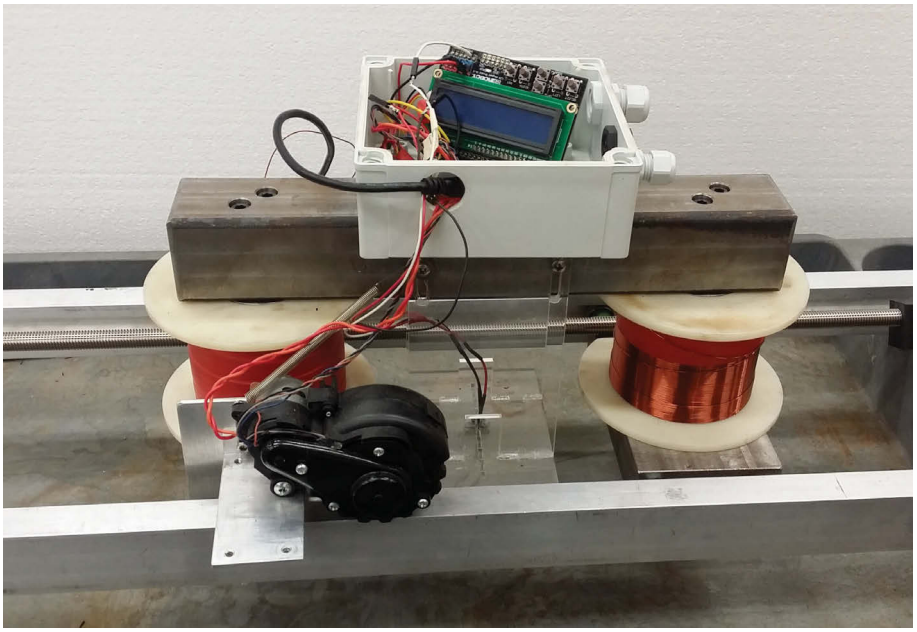

FIGURE 3.17: Prototype of the MFL lab set-up

a more efficient and accurate platform for scanning pipes which finally ends up in better predictions.

FIGURE 3.18: Industrial MFL tool in use [1]

To address these issues, above developed MFL tool was automated to scan a full span of a axial scan automatically (See Figure 3.20). However, the tool does not move circumferentially by itself. This is to keep the practical portability of the tool by keeping the mechanisms simple. The tool should be able to be used in various pipes with a range of

diameters. So a fixed mechanism going circumferentially for a range of diameters of pipe is not feasible.

Considering these requirements, only a linear sliding mechanism has been developed. With the sliding mechanism, the MFL scanner is to be strapped to a section of metal pipe where the scanner will run along the length of its support structure. As the scanner moves, it transmits the signals read by the hall sensors, and these are recorded on the computer connected to the device. These data will be processed to generate the thickness interpretations of the scan area.

Due to the magnetic nature of the device, flaws, dents and uneven surfaces on the pipe can influence the scanning speed of the device and can therefore affect the accuracy of the results. Thus, the device needs to be able to make dynamic adjustments in order to compensate for the constant changes in speed due to the flaws, defects and imperfections on the surfaces of the pipe. The span of the scan is set to 1m and the motors were designed to cover the span in a minute. An FEA simulation was carried out to measure the axial forces generated by the coils. A simple experiment was also carried out to validate the force simulation, but with less strong electro magnets due the instrumentation limitations (Figure 3.19).

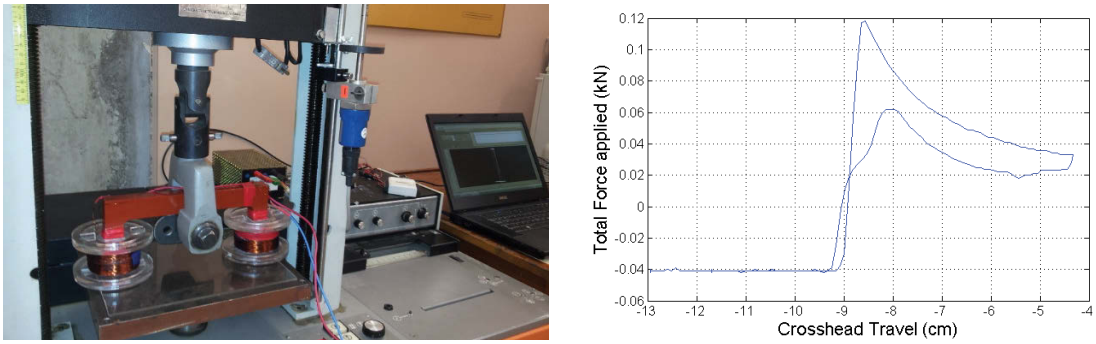

(a) (b)

FIGURE 3.19: Measuring the axial force exerted by the coils: (a) Experimental set-up, (b) Axial force vs vertical displacement.

Once the magnets on the MFL set-up are actuated, it creates about $100N$ axial force along with a $9KN$ normal force. The calculation below assumes a uniform $9KN$ normal force acting on the shoe and the drive shaft is made from AISI 316 stainless steel alloy. Since,

$$\tau = kdF \tag{3.41}$$

where τ is the required torque, k is the coefficient of friction, d is the thread diameter and F is the axial force. As discussed, when $k = 0.1$ for AISI 316 stainless steel alloy, $d = 12mm$ and $F = 100N$, τ becomes $0.12Nm$.

Assuming 1 minute per scan, the RPM of the motor is given by,

$$RPM = \frac{v}{d_p} \tag{3.42}$$

Since $v = 1m/min$ and $d_p = 1.75mm$ for a $d = 12mm$ threaded rod,

$$RPM = 571.4\ rev/min \tag{3.43}$$

By using these design parameters, an appropriate motor was selected and used in the set-up. The complete assembly of the MFL set-up is shown in Figure 3.20.

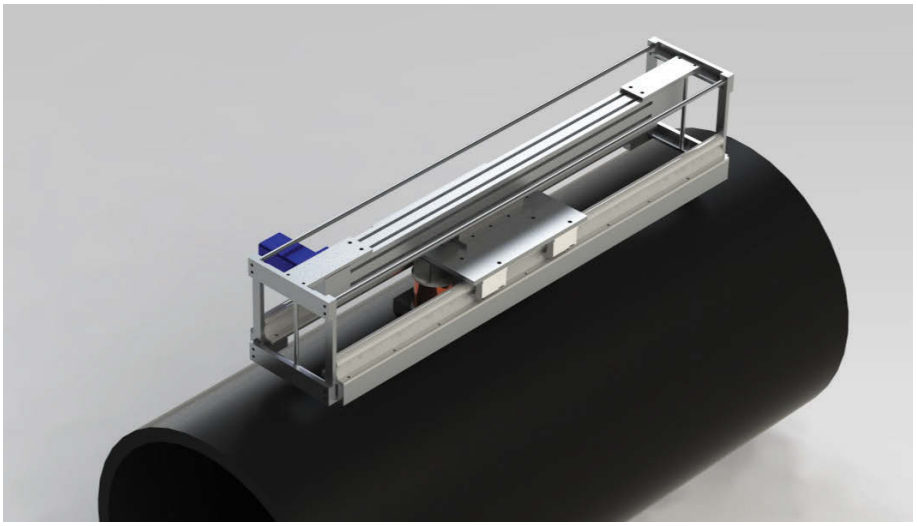

FIGURE 3.20: Semi-automated MFL lab set-up design

When the MFL set-up moves by itself, it is quite important to keep track of the location with respect to the start point, especially when it comes to a high data acquisition rate, where it takes 3 measurements for every millimetre. So the odometry plays a major role

in localising the interpreted defects. The set-up utilises a very accurate wheel odometer to localise the defects along the pipe scan (See Figure 3.21).

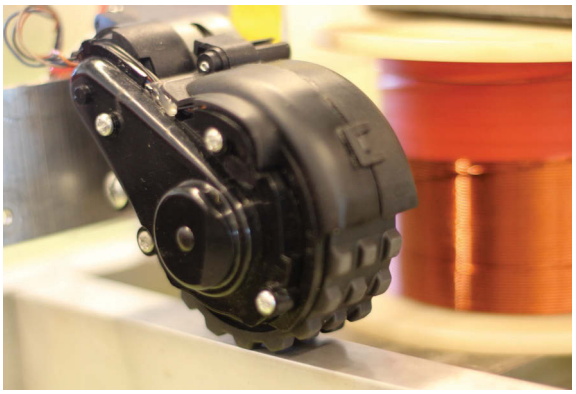

FIGURE 3.21: Wheel odometer used for localisation

With the initial design, some degree of wheel slips were detected with sudden movements specially in the beginning of the scan and the end. Later a spring loaded wheel odometer was used along with rubber enclosure which significantly reduced the wheel slip. The encoder reading was synchronised with the sensor measurements and tethered to a PC for data logging.

3.3.4 Experimental validation of the Simulation model

Once the MFL set-up was in operation, it was used to scan well defined machined defects for validation purposes. Having access to a gray cast iron pipe with no major corrosion was not possible because cast iron pipes are no longer manufactured in the industry. Existing aged pipes were not suitable for the calibration task due to the irregular nature of corrosion patches. Therefore, experimental validations were done on a calibration plate made of gray cast iron where the scanning was done in a laboratory setting with controlled conditions.

The calibration plate was 15mm think and was a simple flat plate with two circular defects. Both defects were 40mm in diameter and 33.3% and 66.6% deep relative to the original thickness. The set-up was placed right on top of the defect such that the sensor aligns with the centre line of the defect. The signal was captured moving the set-up along the length of the plate. In order to validate the simulation model, identical defects were introduced to a 15mm thick plate in the simulation environment. Once the simulation

FIGURE 3.22: Cast iron plate used for model validations

results were generated, they were compared with each other with good agreement with the experimental curves. Although the simulation assumes a homogeneous material, due to the casting process and differences in cooling rates, the magnetic material properties can vary even in a single plate. The slight variations observed in the experimental measurement signals beside the defect are assumed to be due to this reason. Section 3.3.5 discusses the noise levels and sources in MFL signals.

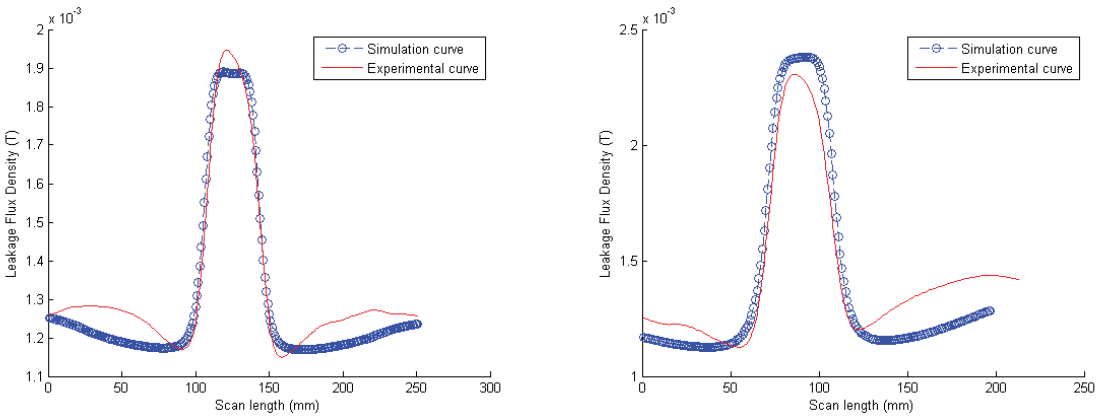

(a) (b)

FIGURE 3.23: Model validation using gray cast iron plates: (a) 33.3% deep defect, (b) 66.6% deep defect.

Further validations were carried out using aged gray cast iron pipes. Defects were machined on the cast iron pipes where there is no major corrosion wall losses. So it is assumed that the machined defect is relatively isolated from any imperfections. Given the fact that these

cast iron pipes are exhumed after about 100 years of service, relatively less corrosion areas were very limited to be used in the validation process (See Figure 3.24).

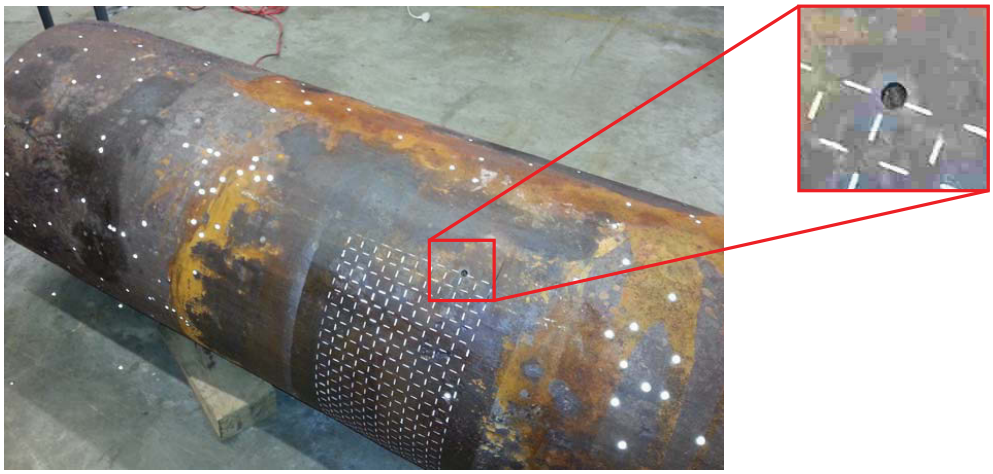

FIGURE 3.24: Machined defects on cast iron pipes

MFL signals were captured by placing the MFL set-up on the centre line of this machined defect and compared with the identical defect simulated in COMSOL Multiphysics® [65] software. Figure 3.25 shows the comparison of these two signals. With all these validation steps it becomes clear that the COMSOL simulation model is capable of simulating the realistic experimental response of the MFL set-up.

3.3.5 Noise Level of Experimental Signals

Repetitive experiments were carried out under controlled conditions to investigate the tool for the noise identified in literature (See section 2.3). Keeping all the conditions and tool parameters the same, industrial tool was used to scan 10 times on the same location. The exercise was repeated on a few independent locations. Signals captured on the same location were analysed for mean and standard deviation. By subtracting the mean for each data point, the noise was isolated (See Figure3.26(b)). It was observed that there was a significant effect on the MFL signal due to noise. Quantitatively signal to noise ratio with respect to the average signal was $SNR = 42.84\ dB$. The noise standard deviation was $2.013 \times 10^{-5}T$. Few major noise factors present in literature [28] were identified in the experimental process.

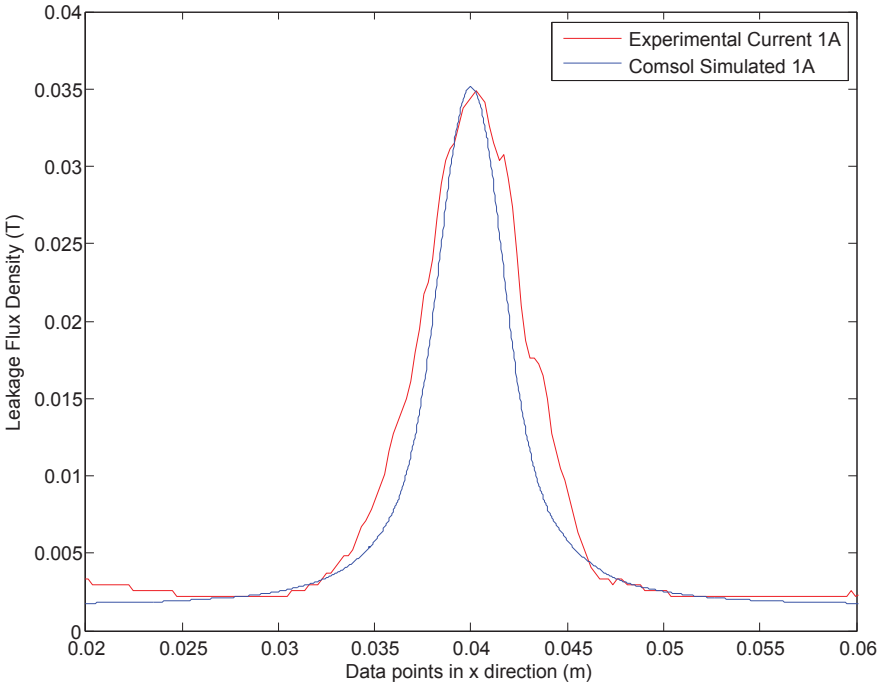

FIGURE 3.25: Comparison of simulated and experimental MFL signal for a machined defect

The nature of the MFL inverse problem is that, the peaks of the MFL signal does not necessarily corresponds to a defect on the test material. One of the major factors affecting the MFL signal is the in-homogeneity of the material. In particular magnetic properties of gray cast iron can vary locally. Irregular cooling rates in the manufacturing process makes the material have different spacial grain structure. This has been verified by microscopic analysis of the grain structure of the pipe samples. Casting lumps and irregular thicknesses are also noticed in cast iron plates and pipes. Any residual magnetisation could also cause noise in later measurements.

Tool and operation related errors are also identified as noise. On Figure 3.26(a), scan 6 demonstrates a slight misalignment with respect to other scans initiated at about $480cm$. A possible odometer slip could result in a similar result. It is very challenging to identify an odometer slip in practise, unless the same location is scanned more than once. However scanning the same location multiple times is time consuming. Modern localisation techniques such as high resolution wheel odometers and lasers can be used to increase the

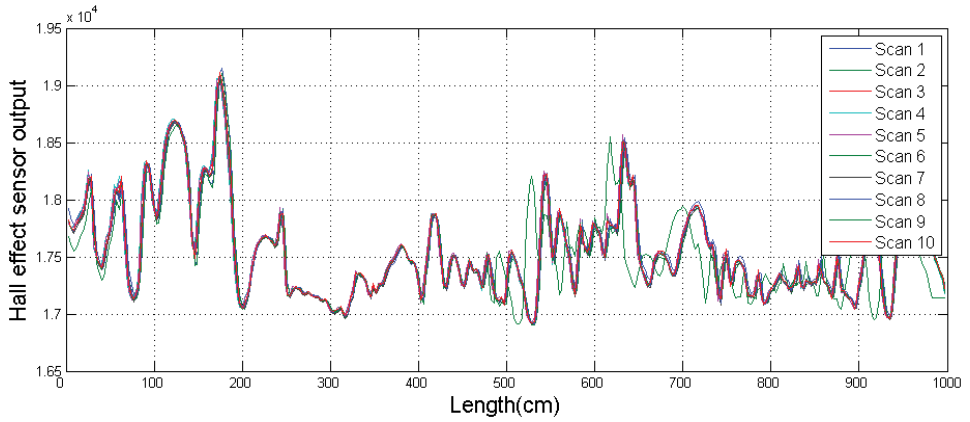

(a)

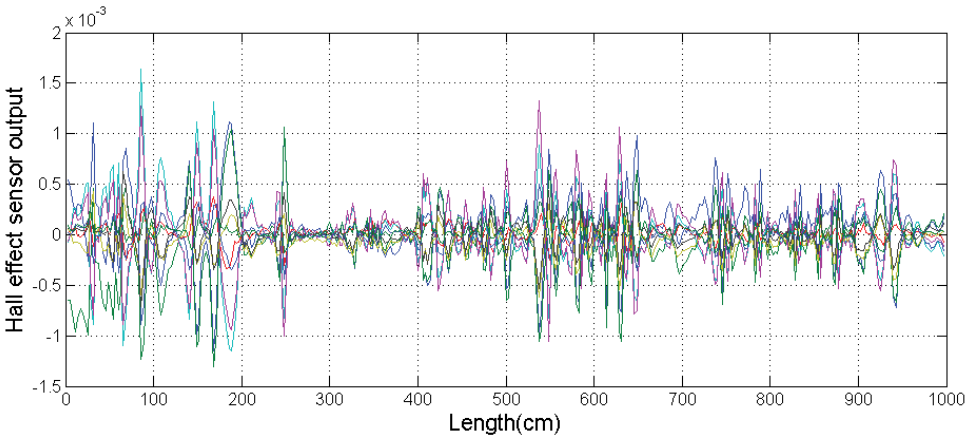

(b)

FIGURE 3.26: Noise level of experimental signals: (a) Industry MFL tool output, (b) Isolated noise.

accuracy of the odometer reading. Some of these techniques were suggested in the MFL lab set-up design in Section 3.3.3.2.

With all these noise sources it becomes a challenging task to interpret MFL signals. Not only the noise level, but the other non unique properties of MFL signals makes the inverse problem more demanding. In Figure 3.27 an example MFL signal on a gray cast iron pipe is shown with the corresponding laser based ground truth. A peak in the MFL signal is affected mainly by defects but also by minor thickness variations in the GT as well as other factors such as material inhomogeneity, residual magnetisation or any other noise source described in Section 2.3. This clearly indicates the need is sophisticated data analytic approaches to interpret MFL signals. Experimental data has been collected using aged gray cast iron large diameter water pipes. The use of modern machine learning techniques and signal interpretation methods developed are discussed in the next chapter.

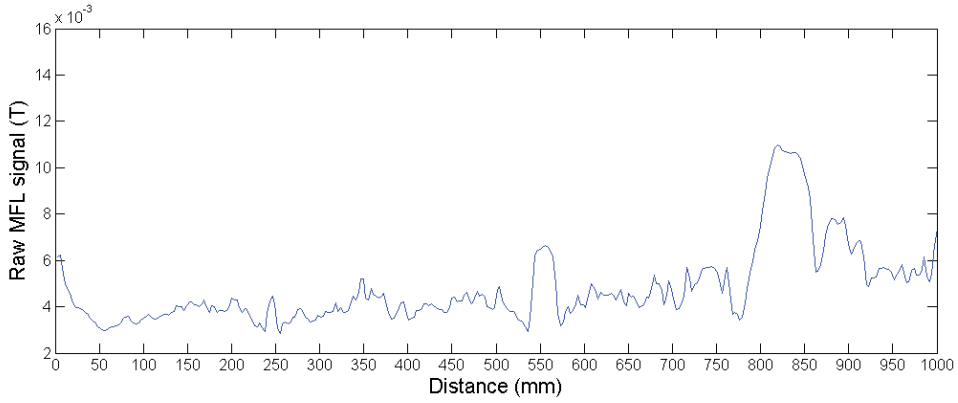

(a)

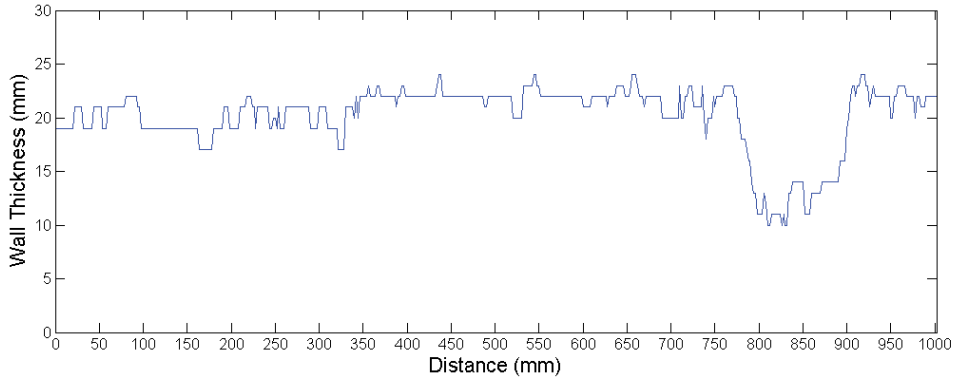

(b)

FIGURE 3.27: Example MFL signal on a gray cast iron pipe: (a) MFL signal, (b) Corresponding cross-sectional groundtruth.

3.4 Discussions and Chapter Conclusions

The main objective of this chapter was to develop a realistic MFL model as the first step towards a data driven inverse modelling. The MFL phenomenon has been initially captured using a dipole based analytical model. Due to its limitations, a finite element analysis based model was developed and two signals were compared with each other with a good agreement. Once the simulation models were validated using the analytical model, further experimental validations were desired.

In order to validate the developed simulation models as well as to collect experimental measurements on cast iron pipes a semi-automated experimental MFL lab set-up was developed. This set-up as well as a similar industrial tool has been used to collect data on calibration defects machined on flat plates as well as on aged cast iron water pipes exhumed after decades of service. These experimental calibration measurements under controlled conditions were used to validate the developed simulation models.

One of the main limitations of the simulation model is the lack of sensor noise. As described in Section 3.3.5 a variety of real life noise sources were identified. Experiments were carried out to characterise the sensor noise and this was introduced to the simulation signals.

Computation power required in the simulations is also another limitation in the generated models. Later in this thesis simplifications and assumptions are made to reduce the exponential computation times. Despite these limitations, the presented approach provided a better platform to collect the extensive data required.

Having an extensive dataset allows the learning of the variations of the signals using data driven approaches. Analysis of MFL signal behaviour, development of data driven models and interpretation of experimental data will be discussed in Chapter 4.

Chapter 4

MFL Data Interpretation using non-parametric Models

4.1 Introduction

In the MFL inspection process, the test ferromagnetic material is magnetised using a strong magnetic field. A localised corrosion pit acts as a region of high magnetic reluctance. Therefore most of the flux lines are diverted around the defect, creating a leakage magnetic field. Suitable sensors are employed to scan this leakage field on which different signal processing techniques are applied for detection and sizing of the defects. However, due to a range of factors that affect the signal behaviour, detection and sizing becomes a challenging problem.

Two main frameworks are generally employed to model MFL signals. Traditional forward approach requires knowledge of precise calibration samples to generate MFL signals which are compared with fresh measurements to infer the most likely defect profile. However, this approach is highly error prone and depends on the calibration pieces.

Although the second type, inverse approach, is more complex, it produces more accurate and robust results. The inverse approach fits a model that can be used to predict the defect configuration from the MFL signals.

With the rapid advancement of computational capabilities, machine learning techniques are being used in solving the inverse MFL problem. Artificial neural networks (ANN) are commonly used in modelling complex relationships between inputs and outputs or to find patterns in data. A.A. Carvalho[3] evaluates the use of ANN for pattern recognition of MFL signals in weld joints. Pradeep Ramuhalli [68] proposed the use of ANN as forward models to determine defect parameters such as the defect length, depth, and shape (profile) from the measured values of the flux density B. This work opt to use Gaussian process regression [69], which will inherently give a measure of uncertainty in the recovered defect profile.

Supervised learning in the form of regression is an important constituent of machine learning for inferring a function from a "labeled" data set, *e.g.* measurements associated with their ground truth. Traditionally parametric models have been used for this purpose. These models have a possible advantage in ease of interpretability, but for complex data sets, simple parametric models may lack expressive power, and their more complex counterparts may not be easy to work with in practice. The advent of kernel machines, such as Gaussian Processes [69] (GP) has opened the possibility of flexible models which are practical to work with. Gaussian Process models can conveniently be used to formulate a Bayesian framework for non-linear regression. In this chapter GP models have been trained to solve the inverse MFL problem.

4.2 MFL Signal Behaviour with Different Defect Configurations

Having a well validated simulation model enables the study of the behaviour of MFL signals under various defect configurations. Each of the test defect scenarios are carefully selected to identify the behavioural features of MFL signals. It is evident that analysing these signals experimentally is not feasible due to the exhaustive defect scenarios used. All the signal acquisition is carried out in the simulation environment avoiding all the noise sources described in Section 3.3.5. A gray cast iron plate of 30mm thickness was used for most of the simulations unless otherwise mentioned.

TABLE 4.1: Simulated different defect scenarios

Defect	Depth	Diameter	Separation between centres
Single circular	0.5mm to 30mm(through hole) with a step of 0.5mm	5mm to 80mm with a step of 1mm	
Two circular	0.5mm to 30mm(through hole) with a step of 0.5mm	5mm to 25mm with a step of 1mm	3mm to 20mm with a step of 1mm

4.2.1 MFL Signal Behaviour with Defect Dimensions

A series of defect dimensions and configurations are used to analyse the basic MFL signal behaviour. All the other parameters such as the excitation strength, lift-off of the sensor and orientation of the tool are kept constant during the experiment. Table 4.1 summarises each of the defect scenarios used. Dimensions of each defect are iteratively changed while capturing each of the MFL signals.

The first row of the table shows the scenario where there is only one defect which appears in one particular scan. Keeping this condition, the defect dimensions are iteratively changed. The bottom of the defect for each scenario is considered flat and the walls of the defect are assumed perpendicular to the bottom and the top surface.This mainly captures the basic behaviour of MFL signals in the presence of a well defined simple isolated defect. Example MFL signals for horizontal line scans when the depth/diameter of the defect is changed, keeping all other parameters the same is shown in Figure 4.1. It is to be noted that each of the lines in the signal plot is a single scan for a given defect scenario.

Figure 4.1(a) shows that when the defect depth increases, the amplitude of the signal increases too. However, this is not the only reason for this to happen; when the diameter of the circular defect is increased, keeping all other parameters the same, the magnitude of the leakage signal is slightly increased as well (See Figure 4.1(b)).

Multiple circular defects are introduced for the next series of simulations. Two defects have been simulated next to each other and the depth, diameter as well as the separation distance from centre to centre have been iteratively changed and analysed.

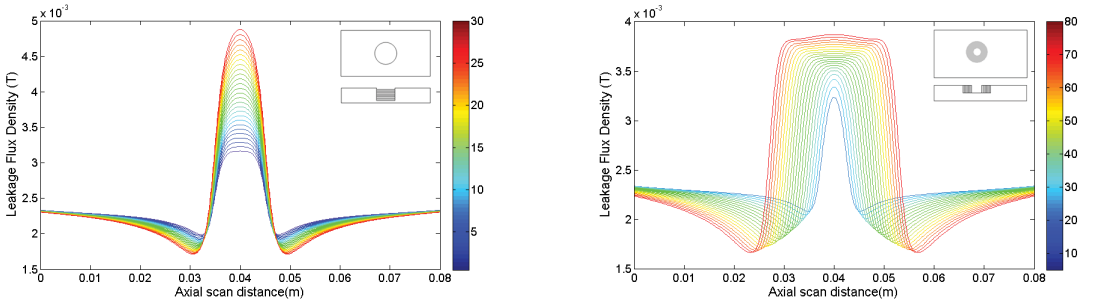

(a) (b)

FIGURE 4.1: Behavior of the axial component of the MFL signal: (a) Varying the depth of one defect, (b) Varying the width of one defect.

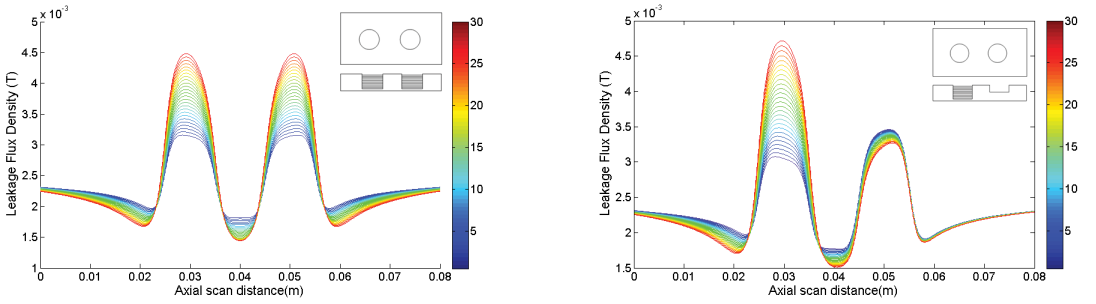

(a) (b)

FIGURE 4.2: Behaviour of the axial component of dual defect MFL signal: (a) Varying the depth of both defects, (b) Varying the depth of one out of two.

Similar to the single defect scenario, in the presence of two defects, the magnitude of the signal changes as both the depths are increased. However, when only one defect changes the depth, it negatively affects the other one which results in a decrease of the leakage flux magnitude. This effect is shown in Figure 4.2(b). Likewise all the combinations shown in Table 4.1 are iteratively used for data collection.

Although the noise sources present in real life scans are neglected in simulations, they do capture the basic behaviour of MFL signals. Given the continuous nature of the MFL scans, a moving window has to be selected to analyse the spacial signals. By selecting a suitable size window according to the defect sizes of interest, any defect combination can be decomposed to either a single defect or two defects interacting with each other.

With the above exercises it is evident that MFL signals demonstrate a clear correlation to the defects. However, there can be other factors that alter the signal readings, such as

tool based parameters. The next section captures these behaviours.

4.2.2 MFL Signal Behaviour with Tool Orientation

Industrial external MFL tools are generally mounted on tracks, so that they can travel in a steady straight line, capturing the leakage signal. However, due to the aged uneven surface of a pipe, few other factors appear to alter the measurements. One of the major factor is the lift-off of the tool. Tool operators try to achieve a consistent lift-off over the full span. However, as mentioned, the uneven erupted pipe surface makes it impossible to have an ideal homogeneous lift-off. Therefore it is important to characterise the effect of the lift-off. The same simulation set-up is employed for this analysis too.

A cylindrical defect of $30mm$ diameter and $10mm$ depth is introduced on the $30mm$ thick gray cast iron plate used in Section 4.2.1. Keeping all these parameters the same, the MFL signals have been captured multiple times by iteratively lifting the entire tool. The simulation is started with a $0mm$ lift-off, in which the shoes touch the scan surface. The tool is then lifted by steps of $0.5mm$ in each iteration. Figure 4.3 shows the signals generated.

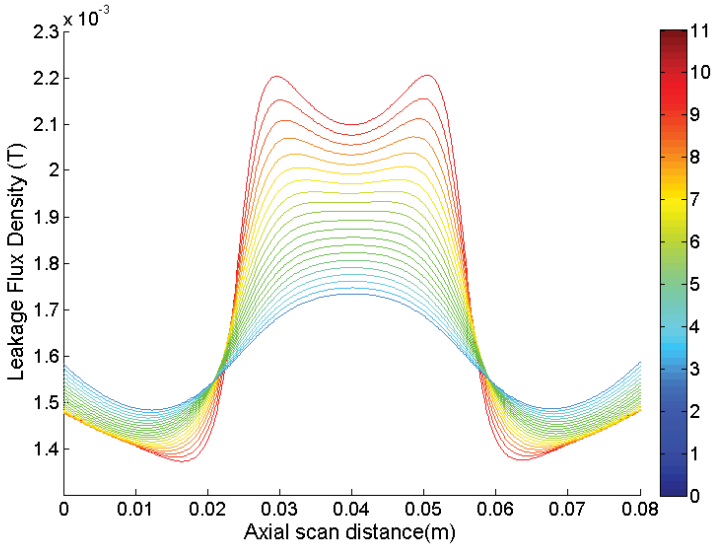

FIGURE 4.3: Behaviour of MFL with asymmetric lift-offs

It's observed that when the tool touches the surface, two distinguish peaks appear on the leakage signal. The higher excitation due to the physical connection between the test

Table 4.2: Single shoe lift-off analysis

Property	Simulated values
Defect diameter	Kept constant at 30mm
Defect depths	29mm, 25mm, 20mm, 15mm, 10mm , 5mm , 1mm and 0mm (no defect)
Initial tool lift-off	4mm
Right shoe lift-off	4mm to 18mm by 2mm steps

substance and the yoke creates strong magnetic poles on the edges of the cylindrical defect. These becomes dominant and make a significant contribution on the total leakage signal shape. However, as the tool lifts off, this distortion gradually disappears and when the tool is about $3mm$ above the surface, the two peaks totally disappear. Moreover, as the tool lifts off further, the signal strength of the MFL signals drops too. So it is desired to capture an optimum signal with an acceptable strength and lesser distortion.

Industrial tool operators use $4mm$ lift-off as their standard to achieve a cleaner signal keeping $1mm$ safety margin for any possible irregularities on the pipe surface. These conditions cannot be maintained in-situ irregular pipe surface. However, it is of interest to compensate for these effects in signal processing rather than physically controlling the signal acquisition process.

Different tool irregularities are analysed on a case by case basis. One of the common tool placement errors is when only one side of the tool comes closer to the pipe surface compared to the other. These scenarios occur when there is a large area of wall thickness reduction. This scenario is analysed by lifting off only one side of the tool which creates a slight angle between the tool and the pipe surface. A series of defects has been used in this analysis and is summarised in Table 4.2.

It is observed that as one shoe of the tool lifts-off, the signal magnitude of that side slightly decreases. This results in a decrease of the peak value too. The behaviour of the MFL leakage signal for each of the defect scenarios in Table 4.2 is shown in Figure 4.4.

When it comes to real life scans ,all the above effects make it very challenging to solve the inverse problem. These relationships become even more complex when multiple defects are present in a single scan. Moreover a cross-section of an aged gray cast iron pipe is more a thicknesses profile than an isolated set of defects.

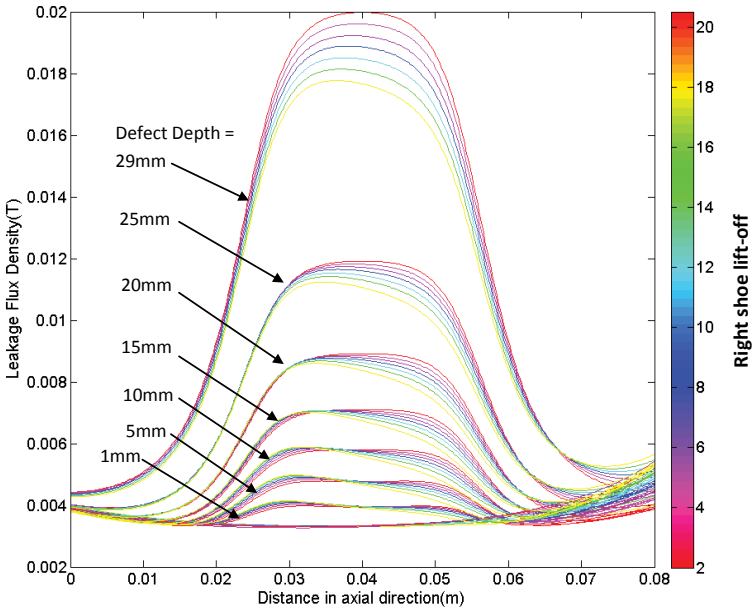

FIGURE 4.4: Behaviour of leakage with the lift-off one shoe

Two main frameworks are generally employed to model MFL signals. The more traditional forward approach requires knowledge of precise calibration samples to generate MFL signals which are compared with fresh measurements to infer the most likely defect profile. However, due to the calibration, this method is less reliable and accurate. Although the second type, inverse approach, is more complex, it produces more accurate and robust results. The inverse approach fits a model that can be used to predict the defect configuration from the MFL signals.

Uncertainty of a prediction becomes crucial when it comes to the decision making process of the water utility providers. Considering these requirements, this chapter takes a Bayesian view of the problem, maintaining a posterior over interpolants rather than simply the maximum-likelihood interpolant, giving a measure of uncertainty in the geometric characterisation of the defects. In this work the proposition is to accomplish this within the Gaussian process framework [70].

4.3 Inverse Modelling with non-parametric models

Inverse modelling is a general framework that is used to infer information about a physical system of interest, from observed measurements. In particular, the approach consists of learning the inverse model to characterise the geometry of defects, *i.e.* depth, width, separation and number of defects in a scan area of a pipe or a plate using MFL measurements as inputs. Mainly the simulation data discussed in Section 4.2 along with their corresponding defect dimensions are used to build models in a supervised learning manner.

4.3.1 Non-parametric modelling

In this section, the non parametric model is formulated in a way that the modelling process is to estimate defect parameters, for instance, the depth of the defects from the MFL device measurements. Let $\{(\mathbf{w}_0, v_0), (\mathbf{w}_1, v_1), ..., (\mathbf{w}_N, v_N)\}$ denote a data set of N hall sensor readings associated with their corresponding depth (*i.e.* the ground truth), where $v_i \in V$ represents the depth of a defect and $\mathbf{w}_i \in \Re^D$ the noisy hall sensor readings. The dimensionality of $\mathbf{w}_i$ is high in general (being all the punctual hall sensor measurements in the horizontal axis extracted from the $2D$ sensor array); therefore, a first step is to reduce the dimensionality of $\mathbf{w}_i$ through a feature extraction process to produce a set of low-dimensional signals with its corresponding depth, $\Psi = \{(\mathbf{u}_0, v_0), (\mathbf{u}_1, v_1), ..., (\mathbf{u}_N, v_N)\}, \mathbf{u}_i \in \Re^d, d << D$. The density $P(v|\mathbf{u})$ must then be estimated from Ψ, without the assumption that Ψ is uniformly distributed over V [71].

Figure 4.5 illustrates a $1D$ example where the v axis shows the state-space, while the u-axis shows the feature space, the space of $1D$ signals extracted from the sensor readings. The solid line shows the most likely sensor reading for each defect depth. When evaluating the likelihood of a particular sensor reading, there are two sources of uncertainty that must be accounted for; the uncertainty in the depth of the defect and the noise of the sensor. In Figure 4.5, sensor noise dominates in the densely sampled area, while depth uncertainty dominates near the edges and in the middle of the state-space.

Given this model, it is straightforward to infer depth of the defects for any MFL device reading. In a similar manner, the models to infer other defect dimensions such as width,

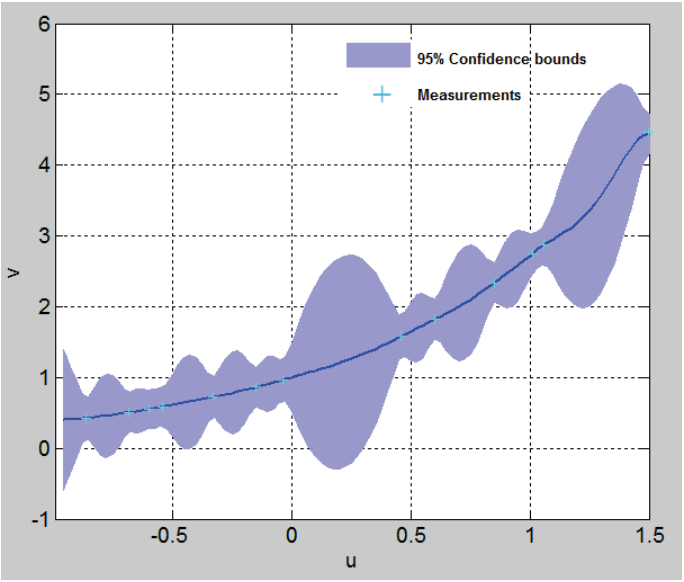

FIGURE 4.5: Illustration of Gaussian processes modelling task.

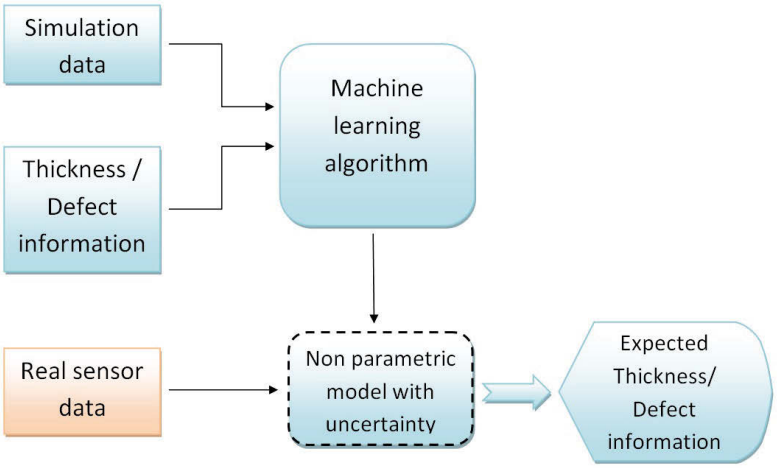

FIGURE 4.6: Illustration of simulation based machine learning approach

separation or the number of defects in a given MFL reading can be learned. These dimensions are independently considered to learn independent models which estimate each quantity separately as shown in Section 4.3.2. The experimental MFL set-up introduced in Section 3.3.3 as well as the industry tool has been used to validate the models and also to generate experimental measurements. The basic overview of this approach is illustrated in Figure 4.6.

4.3.2 Gaussian processes modelling

Gaussian Processes are a non-parametric tool in the sense that they do not explicitly specify a functional model between inputs and outputs. GP can be thought of as a Gaussian prior over the function space mapping inputs and outputs [69].

The problem of learning a MFL signal is one of regression: estimating a function f mapping from inputs $\mathbf{u}$ to output $v = f(\mathbf{u})$. In the context of the present problem, the outputs are the geometrical characteristics of the defects, *i.e.* depth, width, separation and number of defects, and the inputs are the features of MFL signals. To apply a GP framework to this regression problem, one must first select a hyperfunction, called a covariance function. Technically, the covariance function places a prior likelihood on all possible functions. Next, the hyperparameters of the covariance function are learned from the training data. Finally, the combination of the training data and the covariance function induces not only the most likely defect dimension, but also a full posterior probability distribution over all possible defect dimensions.

Formally, we are given a set of N noisy measurements $\mathbf{u}_{1,...,N}$ associated with the outputs $v_{1,...,N}$. The defining characteristic of a GP is that for any finite set of points $\mathbf{u}_{1,...,N}$, the marginal density $p(f(\mathbf{u}_1), f(\mathbf{u}_2), ..., f(\mathbf{u}_N))$ is a multivariate Gaussian. A Gaussian process is completely specified by its mean function $m(\mathbf{u}) = E[f(\mathbf{u})]$ and its covariance function $C(\mathbf{u}, \mathbf{u}')) = E[(f(\mathbf{u}) - m(\mathbf{u}))(f(\mathbf{u}') - m(\mathbf{u}'))]$ as $f(\mathbf{u}) \sim \mathcal{GP}(m(\mathbf{u}), C(\mathbf{u}, \mathbf{u}'))$. The first step is to choose the form of $C(\mathbf{u}, \mathbf{u}')$, which specifies the covariance of this Gaussian for any pair of points. The choice of covariance function is a form of model selection for automatic relevance determination, and should be consistent with prior knowledge about the type of function expected. For the problem at hand, the following commonly used [72] covariance function was selected:

$$C(\mathbf{u}_m, \mathbf{u}_n) = C_i(\mathbf{u}_m, \mathbf{u}_n) + \sigma_v^2 \delta_{mn}, \tag{4.1}$$

where δ is the Dirac delta function, and

$$C\left(\mathbf{u}_m, \mathbf{u}_n\right) = \sigma_f \texttt{exp}\left(-\frac{1}{2}\sum_{l=1}^{D}\frac{\left(\mathbf{u}_m^{(l)} - \mathbf{u}_n^{(l)}\right)^2}{r^2}\right), \tag{4.2}$$

where $\beta = (\sigma_f, r, \sigma_v)'$ represent the hyperparameters of the covariance function. The second term in Equation 4.1 defines the sensor noise, adding σ_v^2 to the diagonal of the covariance matrix for any set of points. Equation 4.2 encodes the correlations between measurements. $\mathbf{u}_n^{(d)}$ denotes the d_{th} component of $\mathbf{u}_n$, a D dimensional vector, *i.e.* the dimension of the feature space.

4.3.3 Hyperparameters of the Covariance Function

Multidimensional outputs are problematic for GPs [72]. In this study, each dimension of the defect is treated independently, building a separate model (with separate covariance function hyperparameters) for each of them. This is an approximation implying no-correlation between the different dimensions of the multiple defects.

In a Bayesian framework, determining the hyperparameters involves first specifying a prior belief about the values of the parameters. Uncertain priors were chosen for all hyperparameters except the sensor noise σ_v, since it can be experimentally characterised.

The next step is to learn the hyperparameters from the training data. Ideally, it should be integrated over all possible values of the parameters to estimate the posterior distribution $p\left(\beta|\Psi, C\left(\cdot\right)\right)$, where $C(\cdot)$ denotes the form of the covariance function. However, since this is analytically intractable, the assumption that $p\left(\beta|\Psi, C\left(\cdot\right)\right)$ is sharply peaked around the most probable values is made, and the integral is approximated by using these values. The most probable values can be found using gradient descent. The posterior over the hyperparameters is given by

$$p\left(\beta|\Psi, C\left(\cdot\right)\right) \propto P\left(V_N|U_{1,\ldots,N}, C\left(\cdot\right), \beta\right)p\left(\beta\right), \tag{4.3}$$

where V_N is a vector of training noisy outputs. Let C_N denote the covariance matrix relating the N outputs. The log likelihood $L = \texttt{log}\left(p\left(v_N|\mathbf{u}_{1,\ldots,N}, C\left(\cdot\right), \beta\right)\right)p\left(\beta\right)$ is given

by,

$$L = -\frac{1}{2}\mathtt{log}\left(\mathtt{det}C^N\right) - \frac{1}{2}v_N^T C_N^{-1} v_N - \frac{N}{2}\mathtt{log}2\pi \tag{4.4}$$

and the gradient of the log-likelihood is given by

$$\frac{\partial L}{\partial \beta} = -\frac{1}{2}\mathtt{trace}\left(C_N^{-1}\frac{\partial C_N}{\partial \beta}\right) + \frac{1}{2}v_N^T C_N^{-1}\frac{\partial C_N}{\partial \beta}C_N^{-1}v_N \tag{4.5}$$

as shown by Gibbs and MacKay [73].

This process allows all hyperparameters to be learned simultaneously from the data. The learning process implicitly trades off the various parameters such as sensor noise and the features' ability to generalise spatially. Note that there are relatively few free parameters that need to be tuned by hand: only the choice of the covariance function and the priors over β. A disadvantage of this process is that it is relatively computationally intensive, since each step of gradient descent requires the inversion of the $N \times N$ matrix C_N . While exact methods were sufficient for the data sets addressed in this paper, Rasmussen and Williams describe a number of approximate methods [69].

4.4 Data Interpretation using Gaussian Processes

As discussed in Section 4.3.2, in this work Gaussian process is formulated in the form of a regression. The main requirement of data driven techniques is the need of exhaustive data for the training process. Simulation signals corresponding to defects summarised in Table 4.1 are used for the training process. In order to evaluate the proposed framework, a set of isolated defects are machined on a plate and scanned using the experimental tool. The prediction results are compared with the groundtruth. The experimental evaluation is further carried out with the industrial tool as well. Large diameter gray cast iron pipes are scanned with the industry tool and the MFL data is analysed using the developed models. Later, the prediction results are compared with the ground truth extracted after exhuming and grit-blasting those sections. A 3D laser scanner has been used to scan the pipes for generating the ground truth.

4.4.1 Feature Extraction

An ideal feature extraction algorithm should minimise the mutual information between the resulting features and the variables of interest (depth/width of defect). Simply, this means that the features should vary as much as possible over the world, while varying as little as possible for any given defect configuration. The X component of the MFL signals were analysed to extract features to be used in the learning process. The features extracted include heights and widths of each peak, distances between peaks, number of peaks. Figure 4.7 illustrates these basic features.

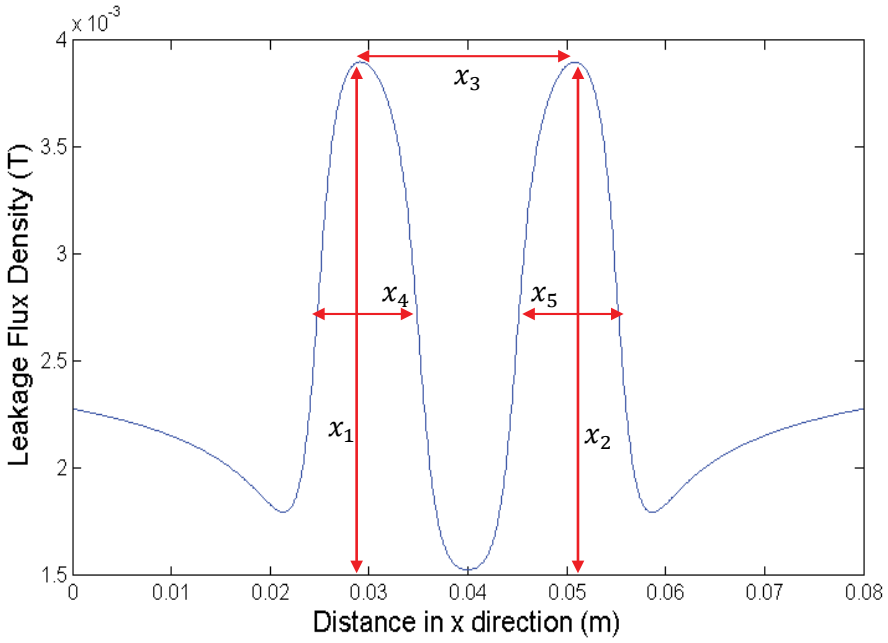

FIGURE 4.7: Basic features of the axial component

Signals were further analysed to investigate mode descriptive features. One way of extracting more features is to convert the amplitude/time pattern into the frequency distribution. Since the phase information is then normally omitted, this conversion leads to a pattern of reduced complexity, although the basic problems of finding adequate descriptive qualities for a pattern remain. Since the MFL signal cannot be associated with harmonics of simple sine functions concept, on which the time-frequency conversion is based, the amplitude/frequency pattern must be considered as a purely descriptive system, not necessarily

having any direct connection with the generating physical system. From this point of view a descriptive system based on time may be regarded as more relevant.

Following this concept, the Hjorth Transform [6] is identified as a more informative set of features for MFL signals. This method takes into account not the detailed histogram, but one of its basic parameters, the standard deviation, and it is further generalised to include also the standard deviations of the amplitude and the second derivative. From these standard deviations have been derived a set of parameters.

1. Activity: Giving a measure of the squared standard deviation of the amplitude, sometimes referred to as the variance or mean power.
2. Mobility: Giving a measure of the standard deviation of the slope with reference to the standard deviation of the amplitude. It is expressed as a ratio per time unit and may be conceived also as a mean frequency.
3. Complexity: Giving a measure of excessive details with reference to the "softest" possible curve shape, the sine wave, this corresponding to unity. It is expressed as the number of standard slopes actually generated during the average time required for generation of one standard amplitude as given by the mobility. Due to the non-linear calculation of standard deviation this parameter will quantify any deviation from the sine shape as an increase from unity.

These three parameters will together characterise the MFL signal pattern in terms of amplitude, time scale and complexity.

Feature Extraction for Industry Tool

Feature extraction used for the industry tool is more simplified. The tool only has magnetic sensors to read the axial component of the signal with the distance travelled. Wheel odometers are used to trace the travelling distance. For each scan the tool generates 8 hall sensor readings and an example of an experimental scan is shown in Figure 4.9.

The aim of this exercise is to apply the same approach that was proved using the experimental MFL tool on the industrial data. However, being a proprietary industrial tool, all

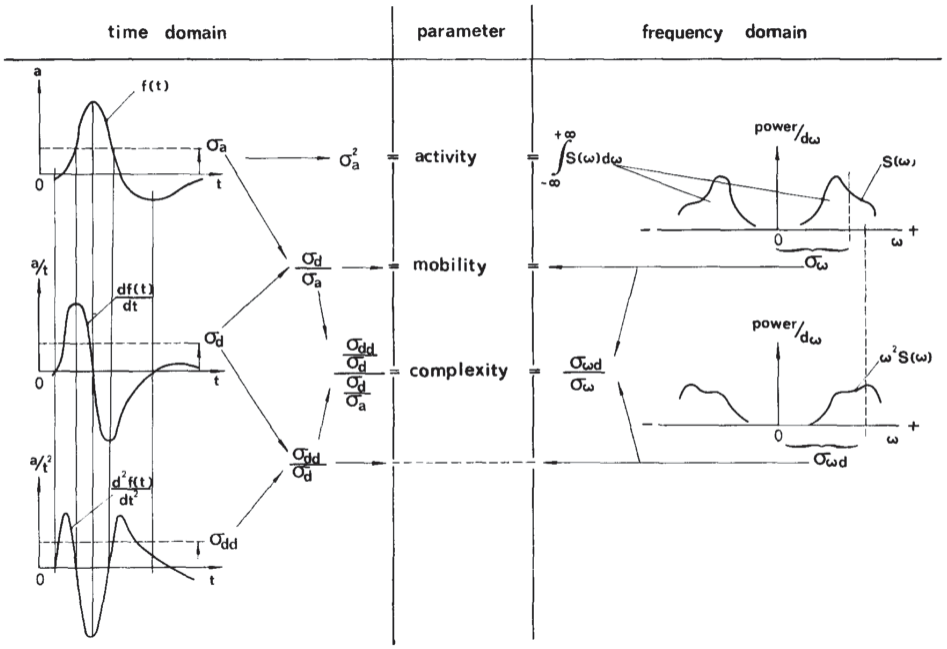

FIGURE 4.8: Features extracted using the Hjorth Transform [6]

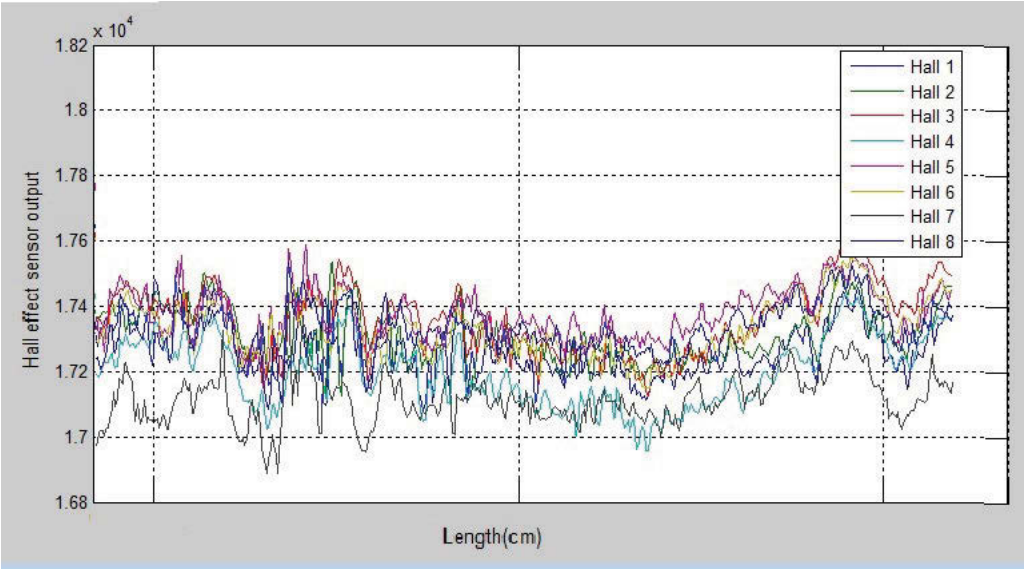

FIGURE 4.9: Typical output signals of the industry tool

the tool specific parameters required to generate the simulation model were not disclosed. An experiment based model validation process was carried out instead. As discussed in the Section 4.3, this approach relies on the extensive data generated using the simulation models. The same validation process for the simulation introduced in Section 3.3.4 was carried out for the industry tool model using well defined machined defects on cast iron

plates.

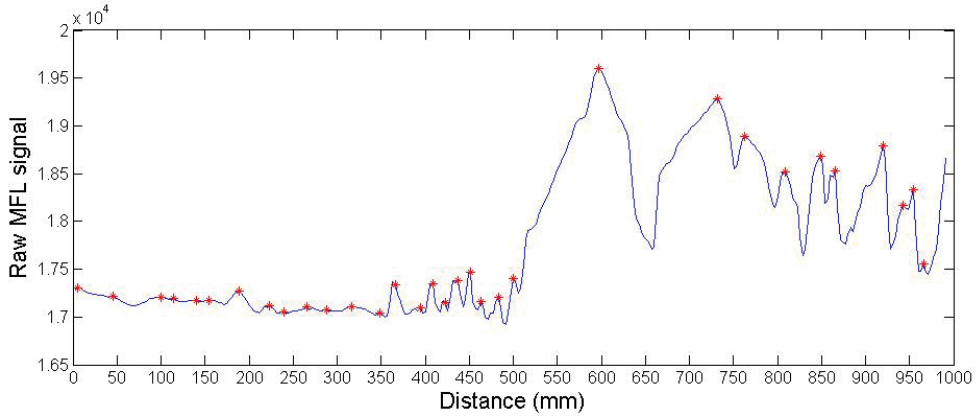

FIGURE 4.10: Basic feature extraction for the industry tool

Due to the limited technical details provided about the proprietary industry tool only a very basic feature is extracted from the signal, the magnitude of peaks of the axial component of the leakage signal. Figure 4.10 illustrates an example of these feature extraction points over a 1m of scan length.

4.4.2 Feature Sensitivity Analysis

In a grit-blasted aged cast iron pipe, it is hard to identify isolated defects. All the corrosion processes over the years create a thickness profile throughout any given cross section. With the multiple defect analysis done in Section 4.2.1, it is obvious that the near defects have an effect on the leakage magnitude, which is the feature value in this case.

The effect of nearby defects on the feature value has been analysed in the form of a sensitivity analysis. The defect cross-section used in this analysis is shown in Figure 4.11. Defect 1 has been kept constant where defect 2 dimensions have been changed and moved further away from defect 1 while capturing the leakage signal for each iteration. Defect 1 diameter has been set to 40mm to keep it half the width of the magnetic shoe. A summary of the dimensions are shown in Table 4.3.

The feature value, namely the peak magnitude with respect to defect 1 has been analysed for each of those iterations. As expected, due to the effect of defect 2, this feature value

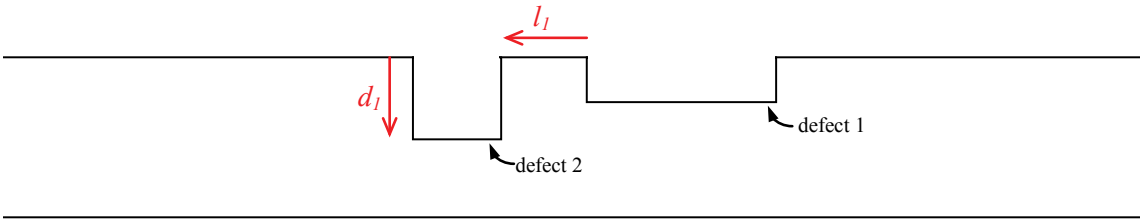

FIGURE 4.11: Illustration of the defect cross-section used in the analysis

TABLE 4.3: Mean squared error values for each GP model.

Property	Value
Thickness of the plate	30mm
Depth of defect 1	10mm (33.3 %)
Width of defect 1	40mm
Depth of defect 2	0 to 30mm by 1mm steps
l_1 Shortest distance	0 to 200mm by 1mm steps

fluctuated. The iterations of defect 2, which didn't change the feature value more than ±5% have been recorded and are shown in Figure 4.12.

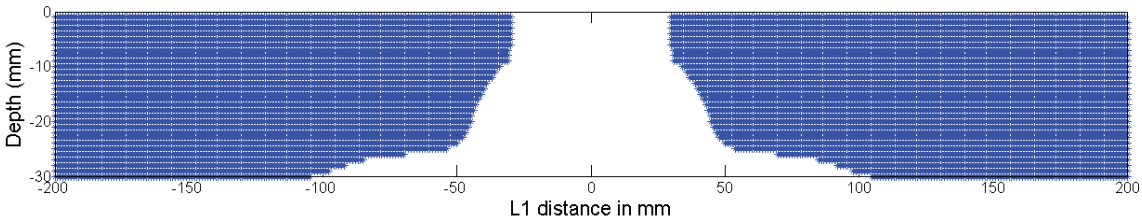

FIGURE 4.12: Feature tolerance area for nearby defects

According to this analysis, it is evident that there can be no defect of depth within $l_1 = 30mm$ from the current defect. Allowable defect depth rapidly increased from $l_1 = 30mm$ to $l_1 = 54mm$. This rate gradually decreases after $l_1 = 54mm$ and when $l_1 = 105mm$ no matter how deep the defect is, it cannot create a significant influence on the feature value of defect 1. This analysis gives an overview of the sensitivity of the feature value in the presence of another close proximity defect.

4.4.3 Obtaining the Ground Truth

The data driven approach discussed in this chapter employs probabilistic models in an attempt to interpret raw pipe wall measurements from MFL technology and produce interpretation of remaining wall thickness. The effectiveness of all the inferred thickness interpretation methodologies used must be evaluated using an accurate ground truth representation of the scan section. Therefore the ground truth extraction plays a major role in this process.

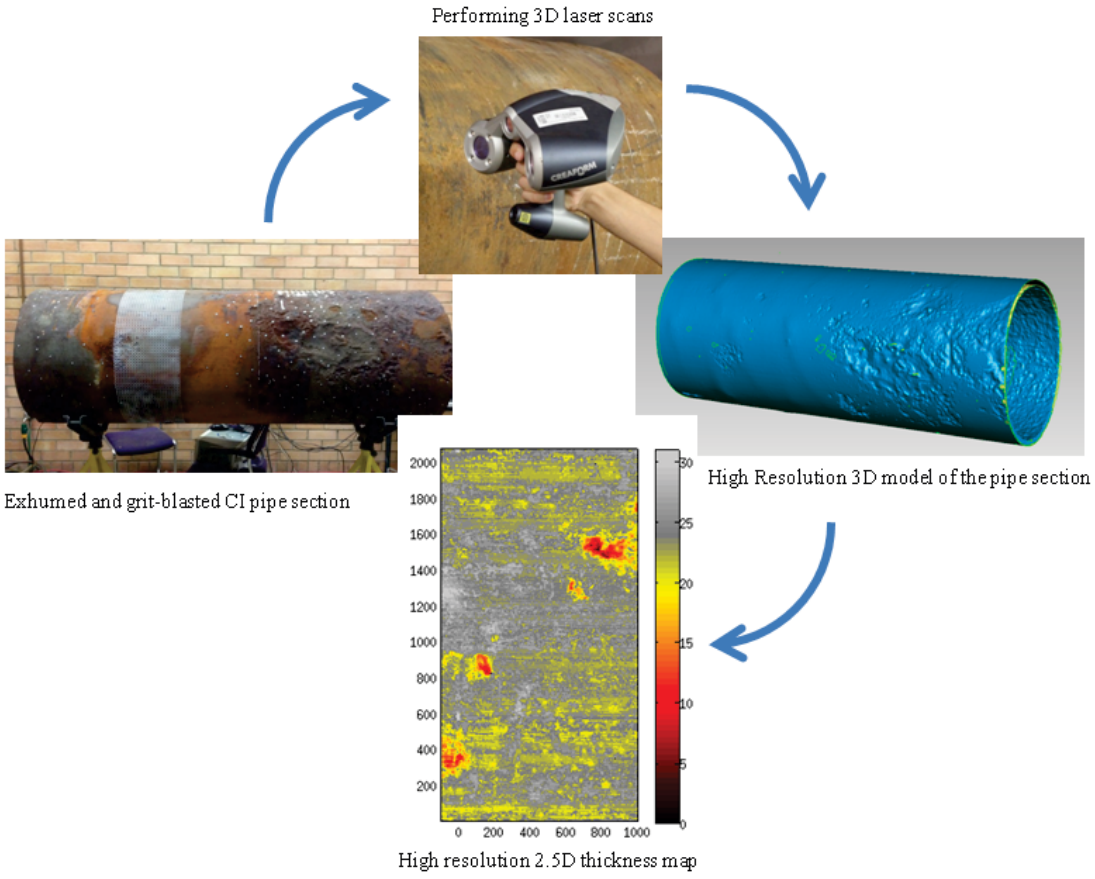

FIGURE 4.13: Process for obtaining the ground truth

The actual remaining thickness of ferromagnetic material in pipe walls is henceforth known as the Ground Truth (GT). Procedure followed to obtain the GT is elaborated in Figure 4.13. After performing MFL scanning, pipe segments were exhumed and grit-blasted to remove rust and graphitisation. The cleaned pipes were scanned with a very highly accurate 3D laser scanner [74] to obtain high resolution 3D point clouds. Currently, ray

tracing is performed using the point cloud acquired from the 3D laser scanning procedure. This point cloud is dense and can contain for example a large number ($> 20million$) points for a single pipe section of $length = 1500mm$ and outer diameter of $\phi = 660mm$.

Spatial filtering on the 3D point cloud has been used to remove outliers that are not part of the surface structure and voxelisation to create a uniformly sampled point cloud. To preserve the fine surface features of the internal and external pipe walls, the Robust Implicit Moving Least Squares (RIMLS) algorithm has been employed to generate a very dense and continuous iso-surface [75]. A computationally efficient ray tracing algorithm is then iterated along the central axis (x-axis), casting rays circumferentially around the voxelised representation of the iso-surface to determine the distance between the inner and outer pipe walls. Using sub-millimeter voxel resolutions allows for the computation of a dense and accurate 2.5D thickness map of the entire pipe section [76].

Validations were carried out by quantitatively comparing the thickness maps produced by the inverse modelling approach against the aligned appropriate GT maps. Results of the quantitative comparison and remarks are presented in the next section 4.5.

4.5 Modelling results

Interpretation framework was first evaluated on the experimental MFL set-up. Improving the interpretations of the industry tool being one of the targets of the research project, similar framework was applied to the industry tool as well. These results are presented in the following sub sections.

For the experimental tool, separate models have been learned to infer each dimension of the defect configuration independently; *e.g.* depth, width and separation. The data sets described in Table 4.1 correspond to $\Psi = \{(\mathbf{u}_0, v_0), (\mathbf{u}_1, v_1), ..., (\mathbf{u}_N, v_N)\}$, where v_i represents either depth, width or separation in the modelling process. For instance in the case of the depth, these data aim to cover various defect configurations for each depth profile.

By using the appropriate groundtruth for labelling, the model and the hyperparameters of the covariance function are learned. An example of the resulting variation of one of the features, namely the magnitude of the X component, with respect to the depth is illustrated in Figure 4.14(a). The model becomes more complex when all the configurations come into play as described in Section 4.2, so the variation of the depth with respect to all other features becomes a multidimensional model.

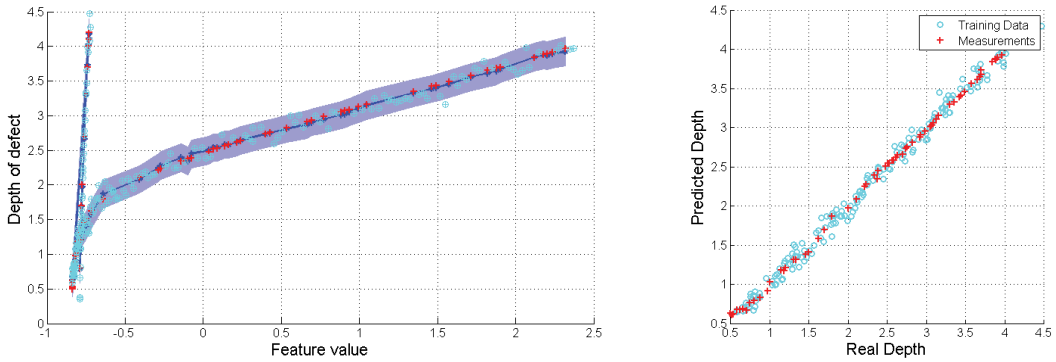

(a) (b)

FIGURE 4.14: Learning and evaluation of results of the GP model.

Gaussian process regression Toolbox version 3.6 (GPML) by Rasmussen [69] was used for the implementation. This tool box was selected since it allows more likelihood functions, further inference methods and a flexible framework for specifying GPs. Once the models have been learned, they are used to infer the defect parameters from fresh measurements. Also to validate the performance of this approach, a 3-fold cross-validation method have been used.

The same exercise has been employed to predict the width, separation and location of the defect as well, producing prominent results as shown in Table 4.4. Although the location is a straightforward solution, having a linear relationship with the peak location of the X component of the leakage field, the same framework has been used to maintain consistency. Therefore an independent GP model has been used to solve the location as well. Figure 4.14(b) illustrates the comparison between the real and the predicted values. To generate the Figure 4.14(b) only the mean prediction values have been used.

One of the main advantages of a GP model is that the model produces an uncertainty indication with each prediction, so the end result comes with bounds on the certainty for each prediction. Mean squared error has been used as a measure to evaluate the models. Since each of defect dimensions has its own model, the mean square error for each model is indicated in Table 4.4.

TABLE 4.4: Mean squared error values for each GP model.

Model	Mean squared error
Depth of the defect	0.000824
Width of the defect	0.003417
Defect separation	0.000148

4.5.1 Data interpretation for UTS MFL Lab Set-up

Initially the experimental MFL set-up has been used to validate the framework. Real measurements have been collected using the experimental MFL set-up on soft iron plates shown in Figure 4.15(a). A raster scan was carried out on the plate with a $3mm$ separation between each scan line covering the area of defects. The features presented in Section 4.4.1 have been extracted from the MFL signals and have been used as the input of the GP models. GP models infer the depth, width and the separation of the defects using independent models.

When it comes to the stress analysis and lifetime predictions it is of immense importance to have the profile of the anomalies. Although it is not the focus of this work, all the developed models have been combined together to generate a complete 3 dimensional profile of the defects (Figure 4.15(b)). A $3D$ reconstruction of the plate is presented in Figure 4.15(b). Top and side views of this reconstruction are shown in Figures 4.15(c),4.15(d) and 4.15(e). A quantitative analysis of the real and predicted values are given in Table 4.5.

Not only the model prediction error but also various other experimental errors contribute to the accuracy of the results. All the noise sources discussed in section 3.3.5 contribute to the overall error. Considering all these sources of noise, the GP modelling framework introduced in this section can be successfully used to interpret MFL signals for pitting

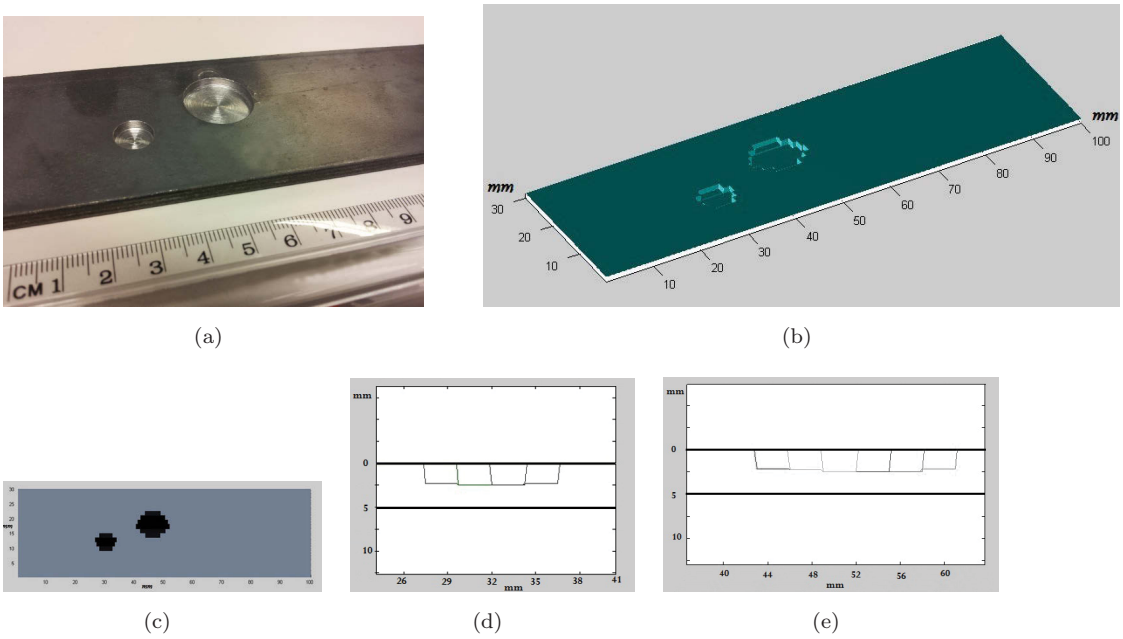

FIGURE 4.15: Comparison of the defect depth profile.

TABLE 4.5: Comparison of real and predicted defect parameters.

	Left Defect		Right Defect	
	Real	Reconstructed	Real	Reconstructed
Diameter (maximum width)	10mm	11.3mm	20mm	19.1mm
Average Depth	2.5mm	2.375mm	2.5mm	2.325mm
	Real	Reconstructed		
Defect Separation	25mm	26.1mm		

and other isolated defect types. After successful evaluation of the framework, the same methodology was used for the industry tool with slight variations.

4.5.2 Data Interpretation for Industrial Tool

As discussed in section 1.2 one of the main objectives of the research project is to provide a better interpretation to water utilities using industrial data. Addressing this need, the following section is to apply the previously described framework on the industrial tool (see section 4.3) which has already been successfully evaluated with the experimental set-up, to the industrial tool.

FIGURE 4.16: Industry tool on the 600mm cast iron pipe

Similar framework described in section 4.3 has been applied to the industry tool where the simulations are used to generate the training data with the required variations due to infeasibility of exhaustive experimental data collection. Simulation data along with the ground truth has been used to train the models. Since the simulation models are well calibrated, signals produced are close to the experimental signals. The trained models are then used to infer the defect information using fresh measurements. The required fresh measurements were collected during a few site trials in collaboration with water utility companies. Figure 4.16 shows the data collection in the field trials at Sydney Water test bed [8].

The scan area of the tool is $1m$ long and $85mm$ wide. The tool scans the 1m pipe circumference as a raster scan by accumulating all axial scans. Depending on the diameter of the pipe, the number of scans needed to scan around the pipe could vary. By using the odometry data and the measured scan locations, the data can be correlated with the actual location on the pipe.

Once the models have been developed the full data set for each scan section is used to evaluate the model. Due to the cylindrical approximation used in the modelling process, the end result infers a single cylinder for each peak detected. When it comes to a full 360^0 data set, these cylinders creates a profile with a combination of hundreds of cylinders.

These plots are called "Measles Plots" in this thesis. Given the data set is properly aligned with the actual pipe, the locations of the measles correspond to the location of the actual defect on the pipe. All the measles are arranged to generate an approximated $2-D$ defect profile.

After the MFL scanning process, the pipes were grit-blasted and the ground truth extraction method discussed in section 4.4.3 was followed. This allows a one-to-one comparison of the inference results with GT.

As discussed before, one of the major advantages of following this framework is that it gives the uncertainty of each prediction. Every single measle is associated with an uncertainty value too. So when it comes to decision making about the replacement of the infrastructure, these prediction uncertainties can be taken in to account. A visual comparison of a $2.5D$ ground truth plot [76], GP inference measle plot and uncertainties associated with each measle is shown in Figure 4.17(a),4.17(b) and 4.17(c) respectively.

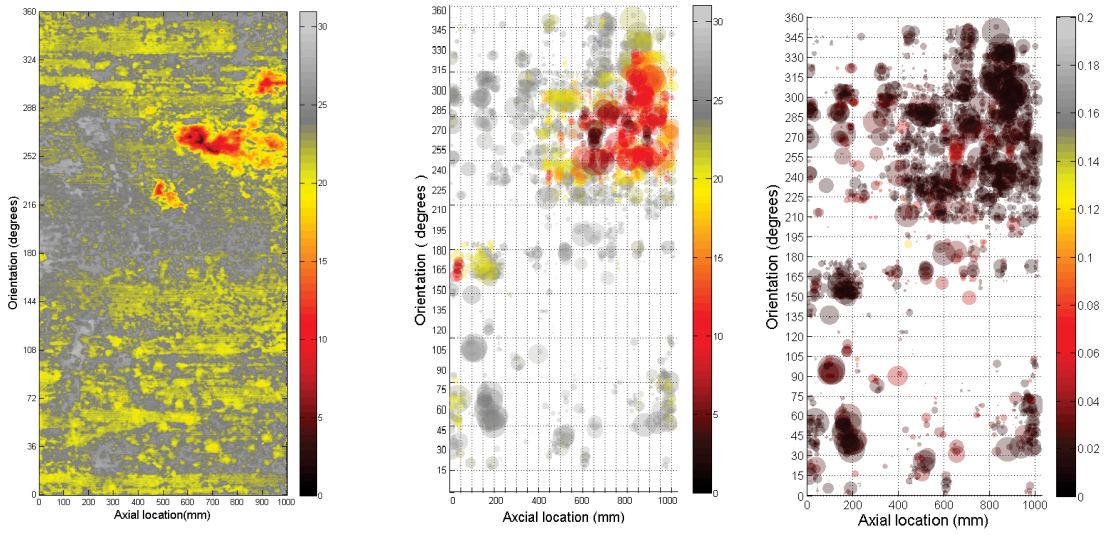

(a) (b) (c)

FIGURE 4.17: Comparison of ground truth and predicted measle plots with uncertainty for Trial 2 pipe section 3: (a) 2.5D Ground truth plot, (b) Predicted measle plot, (c) Uncertainty of each measle.

As part of the collaboration, the industry partner provided interpretations based on their existing industry standard methodology. This allowed for a qualitative and quantitative analysis of remaining wall thickness (RWT) of gray cast iron pipes as reported by the

industry partner and also as predicted by this framework from the same raw industrial data. Estimations are compared against sub-millimetre accurate laser GT generated as discussed in section 4.4.3.

Following parameters and definitions were used in the evaluation process.

Industry reported RWT

Current industrial scan reports provide worst 10 RWT defects per pipe segment and their locations. These reports are used as the industry standard, to evaluate the developed framework.

GP predicted RWT

The proposed framework infers a large number of defects. 10 worst RWT defects were sorted and worst ten RWT defects were selected for the RMS error comparison

Worst 10 RWT areas in GT

Ten minimum RWT areas in the laser measured RWT were identified by searching through non-overlapping 10cmx10cm grid cells in the laser measured RWT

Search Window

Industry reported results showed discrepancies in the location of the defects with respect to those found on the exhumed pipes. In order to accommodate misalignments between laser measured RWT and raw data scans, a search window of $10cm \times 10cm$ on the laser measured RWT was used. This window was chosen such that it was centred at the industry reported RWT location. Likewise for GP results too. RMS errors were calculated as the difference between reported/inferred defect and the worst RWT found within the same search window on the laser measured RWT.

These evaluation experiments were carried out for eight 1m long, 660mm diameter gray cast iron pipe sections. Figure 2(a) compiles the industry reported RWT for all the pipe segments. Likewise for GP based framework in Figure 2(b). Results were plotted against the matched defect in the laser measured RWT as described above. Root mean square (RMS) error is 12.72mm for industry reported RWT, and 4.59mm for GP based framework predicted RWT. Industry reported RWTs appear heavily biased towards through-wall defects. GP framework predicted RWTs do not show such a bias.

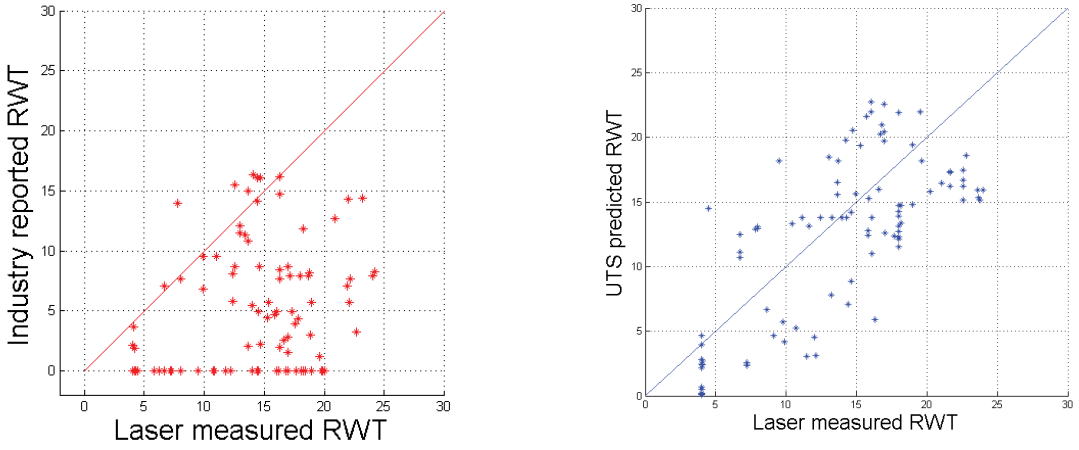

(a) (b)

FIGURE 4.18: Overall comparison of Industry reported/GP inference vs GT for 8 pipe segments: (a) Industry reports vs GT (RMS error:12.72mm), (b) GP inference vs GT (RMS error:4.59mm).

4.5.2.1 Individual Pipe Section Comparisons

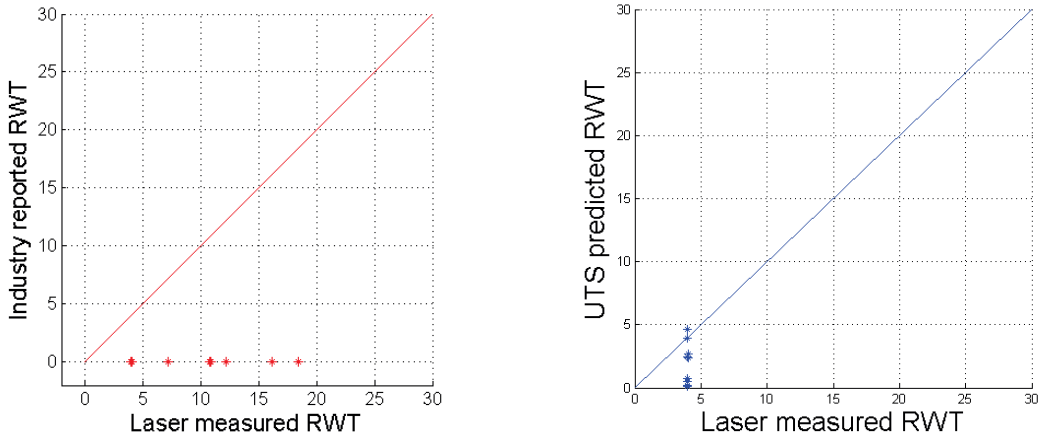

(a) (b)

FIGURE 4.19: Individual comparison of Industry reported/GP inference vs GT for Trial 2 Pipe section 2: (a) Industry reports vs GT (RMS error:10.24mm), (b) GP inference vs GT (RMS error:2.73mm).

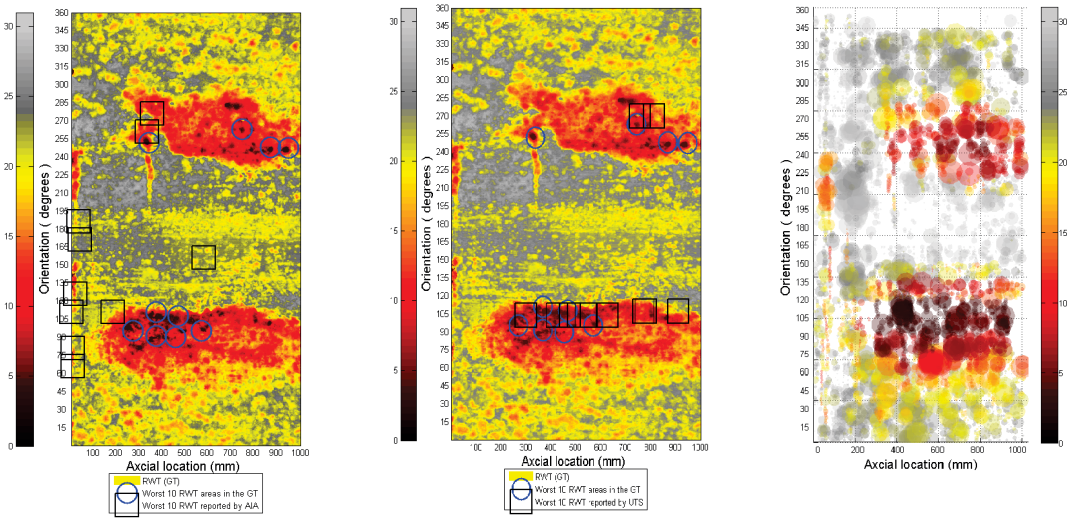

(a) (b) (c)

FIGURE 4.20: Individual comparison of industry reported/GP inference vs GT for Trial 2 Pipe section 2: (a) Worst 10 RWT reported by Industry partner and worst 10 RWT areas in GT, (b) Worst 10 RWT inferred by GP and worst 10 RWT areas in GT,(c) GP inferred measle plot.

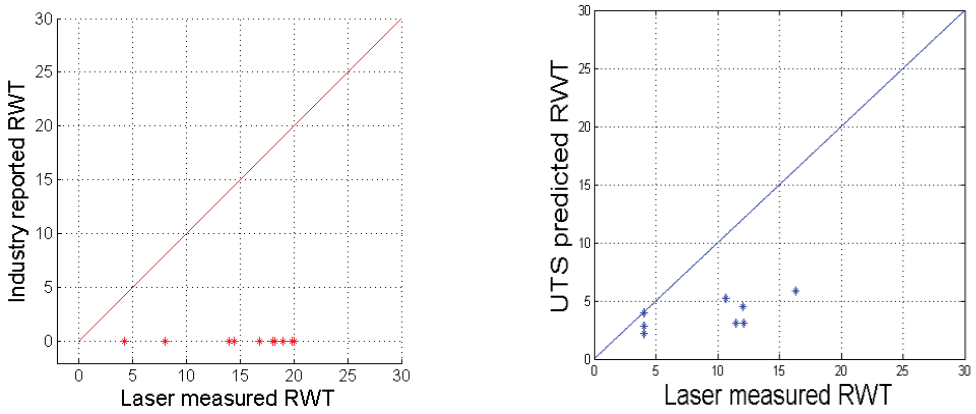

(a) (b)

FIGURE 4.21: Individual comparison of Industry reported/GP inference vs GT for Trial 2 Pipe section 3: (a) industry reported vs GT (RMS error:16.5mm), (b) GP inference vs GT (RMS error:5.96mm).

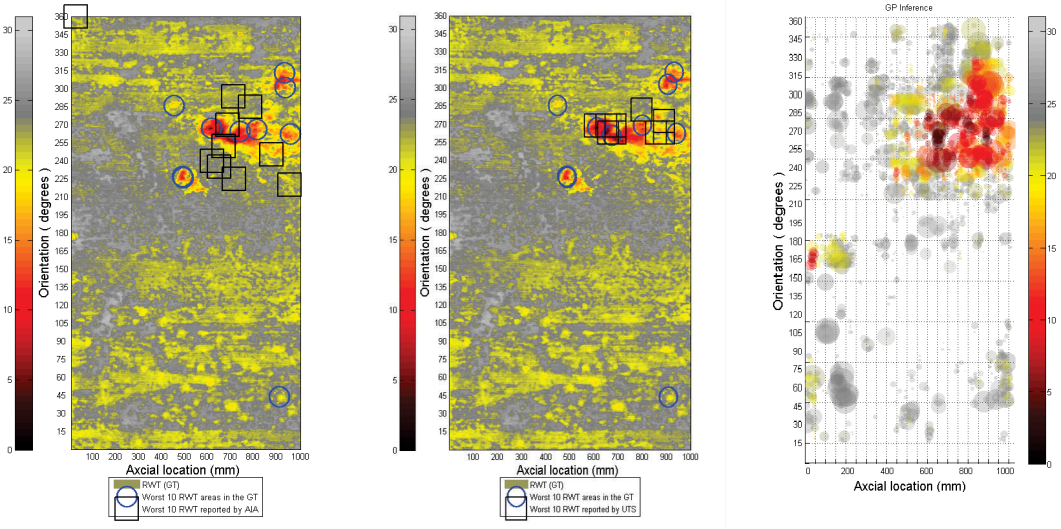

(a) (b) (c)

FIGURE 4.22: Individual comparison of industry reported/GP inference vs GT for Trial 2 Pipe section 3: (a) Worst 10 RWT reported by industry partner and worst 10 RWT areas in GT, (b) Worst 10 RWT inferred by GP and worst 10 RWT areas in GT,(c) GP inferred measle plot.

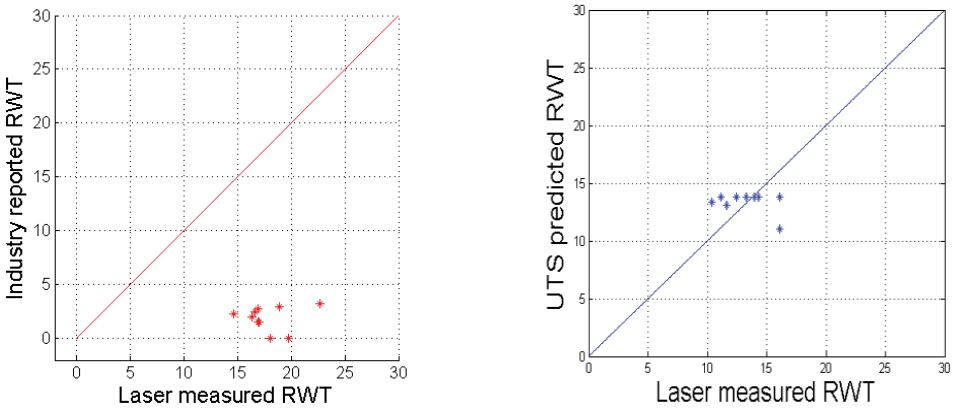

(a) (b)

FIGURE 4.23: Individual comparison of industry reported/GP inference vs GT for Trial 3 Pipe section 1: (a) Industry reports vs GT (RMS error:13.20mm), (b) GP inference vs GT (RMS error:2.37mm).

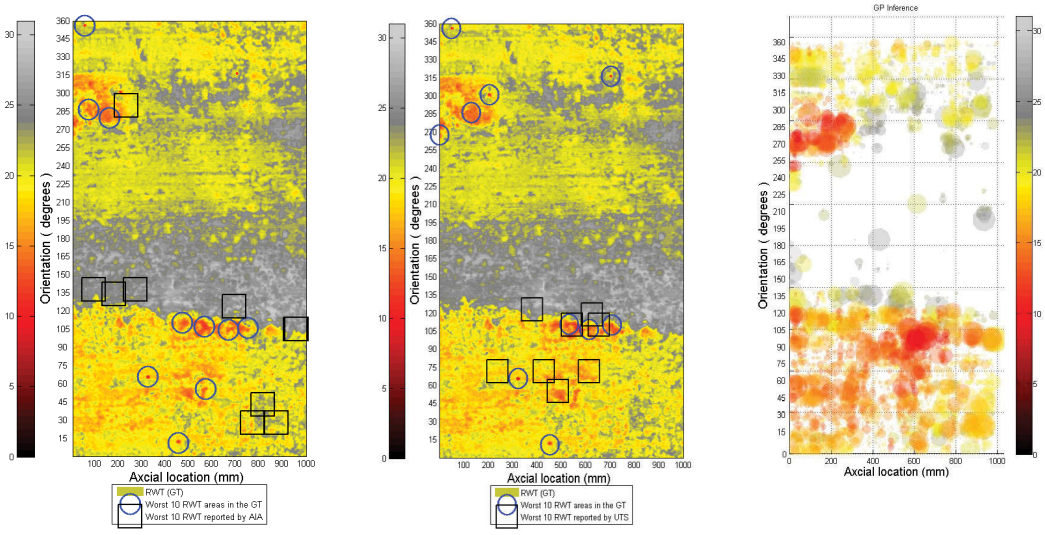

(a) (b) (c)

FIGURE 4.24: Individual comparison of industry reported/GP inference vs GT for Trial 3 Pipe section 1: (a) Worst 10 RWT reported by industry partner and worst 10 RWT areas in GT, (b) Worst 10 RWT inferred by GP and worst 10 RWT areas in GT,(c) GP inferred measle plot.

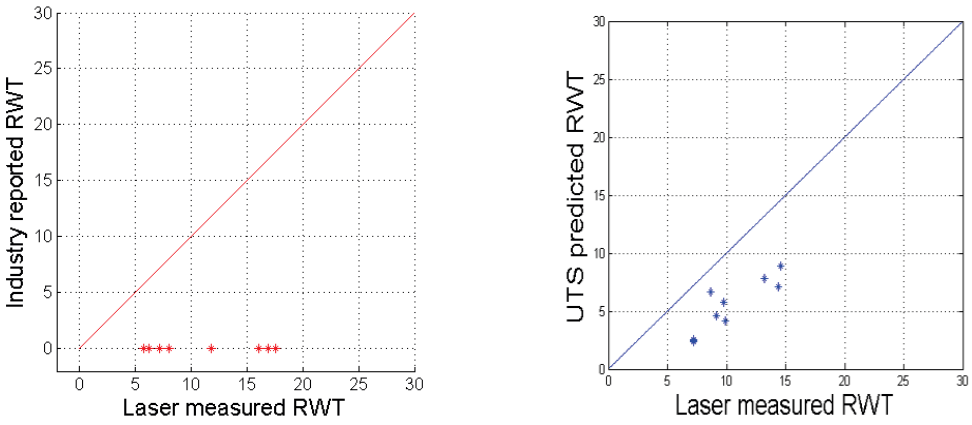

(a) (b)

FIGURE 4.25: Individual comparison of industry reported/GP inference vs GT for Trial 3 Pipe section 3: (a) industry reports vs GT (RMS error:11.81mm), (b) GP inference vs GT (RMS error:5.05mm).

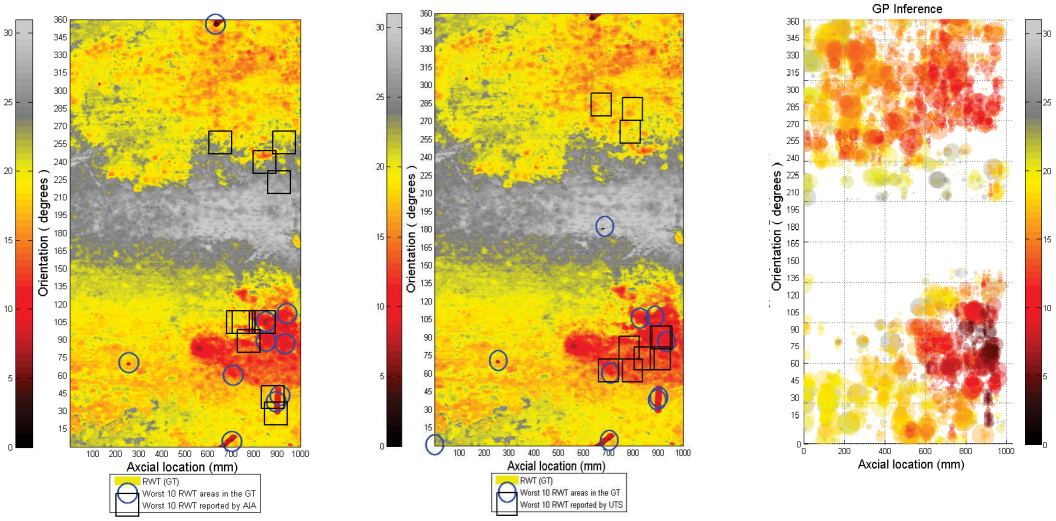

(a) (b) (c)

FIGURE 4.26: Individual comparison of industry reported/GP inference vs GT for Trial 3 Pipe section 3: (a) Worst 10 RWT reported by industry partner and worst 10 RWT areas in GT, (b) Worst 10 RWT inferred by GP and worst 10 RWT areas in GT,(c) GP inferred measle plot.

4.5.2.2 Development of a Software Module

As an agreed deliverable to the industry partner, a software module was specifically designed to interpret data from the Smart-CAT (tool provided by the industry partner). The back end of the software uses the above discussed GP based data interpretation framework. The models are entirely trained based on simulation data and the user can load experimental data collected from in-situ gray cast iron pipes of diameter range of $350mm$ to $660mm$. This range can be increased with the availability of validation data in future.

The software module is a standalone package that runs on 64 bit Microsoft Windows and has a simple graphical user interface for the convenience of the user. Industry partners have evaluated the software with constructive feedback and it will be further developed to meet the industry needs. The GUI of the software package is shown in Figure 4.27.

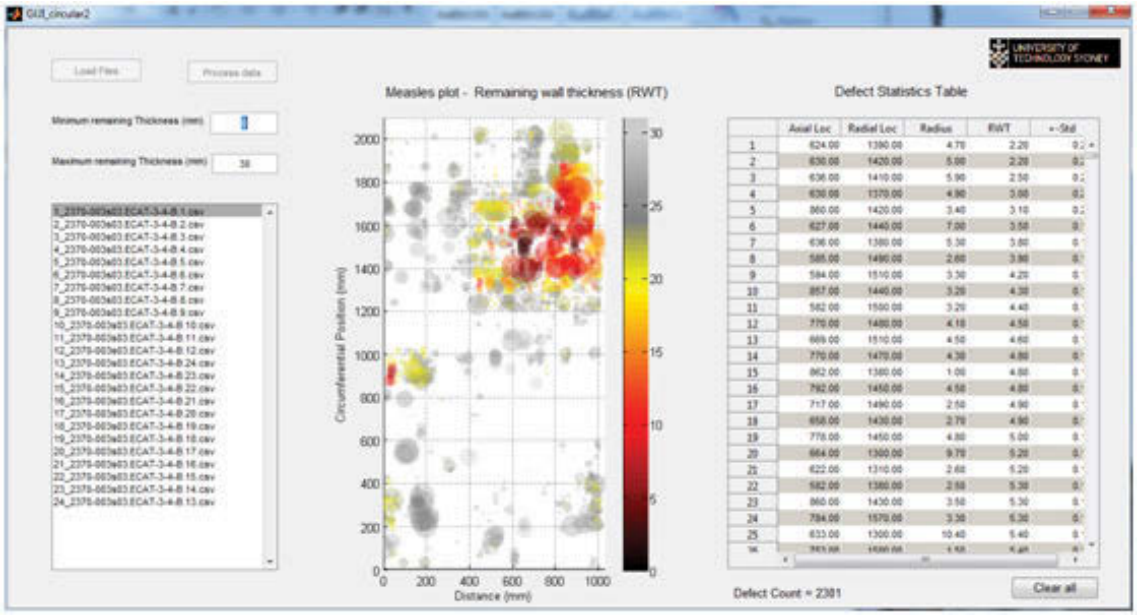

FIGURE 4.27: GUI of the software module released to the industry partner

Individual models have been trained for different thicknesses of pipes. Therefore the user has to input the nominal thickness of the pipe. This is normally related to the diameter of the pipe, or can be extracted from hydraulic profile specification sheets of the utility company. According to this value the corresponding model is used to interpret the signals. The software outputs the 360^0 measle plot for the scan section as well as a defect statistics table along with the uncertainty of the depth prediction for each measle.The first few lines

TABLE 4.6: Defect statistics table generated by the software module

Axial Loc in mm	Radial Loc in Deg	Radius (mm)	RWT (mm)	± STD
640	263	4.7593	6.3352	0.0648
649	264	5.8501	6.3682	0.051041
637	261	4.7385	6.901	0.056391
649	259	5.2512	7.0557	0.087124
877	264	3.1669	7.2574	1.7649
877	263	2.8197	7.3692	2.3188
643	266	4.9565	7.4608	2.147
634	268	2.5	7.7855	2.0095
877	266	3.4017	7.8508	2.1991
671	268	2.6622	7.855	2.0867
877	261	4.6631	8.0149	2.2436
877	268	3.5013	8.2258	2.3133
880	259	1.0139	8.3142	2.3871
594	281	3.2313	8.3851	2.3021
594	259	2.5	8.4739	2.2255
606	283	3.2829	8.5173	2.156
709	259	2.5	8.9915	2.0917
786	276	4.2938	9.0187	2.0328
...	...	...	...	...

of an example defect statistics for Trial 2 pipe section 3 is shown in Table 4.6. A typical aged CI pipe could contain more than 1000 table entries.

4.6 Discussions and Chapter Conclusions

Due to the complexity of the MFL signal behaviour an inverse modelling approach was followed to predict the defect configurations. The problem was formulated in the form of supervised learning as a regression. A semi parametric Gaussian Processes model was employed in the learning process.

The nature of machine learning is the more the data can capture variations, then the better the results. Since generating the required extensive data set experimentally is prohibitive, Comsol® [65] simulations were used. Different defect dimensions as well as multiple defect configurations were analysed in the simulation software to generate the MFL response. Suitable features were extracted from these MFL signals to best describe

the MFL signal over changes in the defect scenarios. Extracted features along with the associated groundtruth were used in the training process.

Evaluation of the models were carried out using the simulation data as well as using the industrial MFL tool. Interpretations generated using the industrial data were compared with the industry contractors reports generated using the same data. It shows a clear improvement of the accuracy of the interpretations using the GP models. These models were transferred to the industry partners as a software package for the benefit of both contractors and water utility companies.

One of the main limitations of the proposed method is that it can only approximate defects into a combination of cylindrical defects. Even though these cylinders can overlap each other to make complex defect shapes, they are far from the real RWT profile.

Another limitation in the framework is the requirement of a well validated simulation model. The entire training process relies on the simulation data which needs to be generated through a validated simulation model. This could not be fully implemented due to proprietary industry tools and the only possibility was to use approximate model validations.

Although the industry standard is to approximate defects to measles of a circular cross section, latest research on stress analysis finds it otherwise. As part of the research project, Monash university conducts research on stress analysis on aged cast iron pipes. Latest findings on stress on CI pipes shows that the defects of ellipsoidal shape are prone to stress based failure and to having the highest stress concentration. This raises the need of interpreting defects as ellipsoidal. Unconstrained global optimisation methods are proposed to interpret large wall loss areas on cast iron pipes as ellipsoids. This approach is discussed in the next Chapter.

Chapter 5

Analytical Model-Aided Optimisation for Ellipsoidal Defect Approximation

5.1 Introduction

Concentrated working stress of a corrosion pit is known to be an important factor inducing the deterioration and consequently the breakage of a buried pipe [77]. The corrosion pits, which is a common damage form of buried CI pipes, reduce pipe resistance and give rise to pipe breakage by intensifying the local stress field. The stress magnification on these local stress fields is best knows as stress concentration factor(SCF) [78].

Parametric studies show that elliptical defects on CI pipes are more prone to failure by the maximum stress development which can properly identify the onset of localised failure of a corrosion pit, thereby the water leakage [23]. Hence, approximation of ellipsoidal defects could play a significant role in failure prediction of CI pipes. Following up these requirements, global optimisation techniques are employed for the ellipsoid approximation of defects.

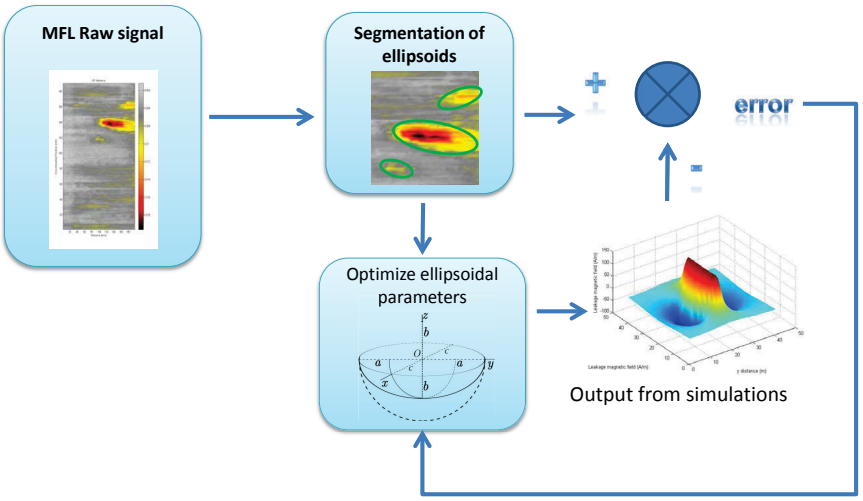

FIGURE 5.1: Iterative framework for ellipsoidal defect estimation

Proposed method uses industrial MFL data as the reference signal. An initial guess is calculated using a segmentation method run on the raw data plot which is then used in an iterative optimisation algorithm. Due to the possibility of parameterisation of ellipsoidal defects, a dipole based analytical model has been developed for the MFL leakage flux of an ellipsoidal defect. This model is computationally very efficient compared to a much more computationally complex FEA simulation of the same type.

Analytical model creates the leakage flux for a given ellipsoid, and is compared with the measurement leakage. This process is literately optimised until the model prediction best fits the given reference, in this case the measured field from the MFL tool. Finding the ellipsoidal parameters that minimises the model mismatch to the reference measurement, is equivalent to solving the inverse problem of finding the ellipsoid producing the most similar MFL measurement.

These approximated ellipsoidal parameters then can be successfully used for stress analysis. This chapter first derives the analytical model for an ellipsoidal defect based on the model described in section 3.2. The model as well as the proposed framework is then validated using a few machined ellipsoidal defects on a grit-blasted CI pipe. Later this model is used in the iterative optimisation process to find the best suitable ellipsoidal defect.

5.2 Formulation of the Optimisation Problem

The industrial MFL tool has been used to collect data circumferentially on aged CI pipes. Once the raster scans are arranged in the order of their locations, it creates a dataset of the full pipe. The raw signals are segmented to identify the valleys in the profile. These segmented valleys are individually used in the iterative framework to approximate the ellipsoidal parameters that best describe the defect.

A forward model which generates the leakage field for a given ellipsoid has been used in the framework and is the basis of the iterative process. When it comes to parameterisable individual defects, few methods can be used to generate the leakage field. These FEA models are very computation intensive which makes them slow to use in a iterative process. On the other hand, dipole based analytical models are computationally efficient but do not account for most of the real word imperfections. However, with suitable assumptions and approximations these analytical models can be developed to generate the leakage magnetic field for a given ellipsoidal defect. Ellipsoid parameters are then iteratively changed to best match the segmented measurement signal in the iterative process.

5.2.1 Forward Model Formulation

Since the forward model is used to generate the equivalent field of the measurement, accuracy of the forward model is crucial. The model should generate a rational MFL signal to match the signal measured on the pipe. A similar dipole based analytical model to the one developed in section 3.2 has been derived to parameterise the Magnetic flux leakage of an ellipsoid defect.

As discussed in Chapter 1, MFL technique consists of magnetising the material, and during this excitation a corrosion pit acts as a region of high magnetic reluctance. This causes the magnetic flux to divert, to avoid the high reluctance area resulting in a dipolar magnetic charge (DMC) on the defect walls of opposite sides [33, 60]. This phenomenon is the basis for the following derivation similar to that of Section 3.2.

In this derivation, the effects of variations in magnetisation and permeability of the material are minimised by assuming high magnetic excitation, corresponding to the saturation region of the material. The model also assumes that the eddy currents, which occur in ferromagnetic materials due to the relative motion of strong magnetic fields, can be neglected. It is also assumed that, stray magnetism, stress, temperature etc. which can influence the leakage flux are very minimal in the order of magnitudes considered and are also neglected[39].

There are few additional assumptions made for this derivation. It has been truncated with the infinite domain Ω^{∞} now at a finite distance sufficiently far from the region of interest (ROI) and the model domain $\Omega \subset \Omega^{\infty}$ has been created. It's also considered that $\Omega = \Omega_0 \cup \Omega_{st}$ to be consist of two homogeneous materials; air in Ω_0 with absolute permeability $\mu = \mu_0$ and a linear steel material in Ω_{st} with absolute permeability $\mu = \mu_0 \mu_{rs}$.

Further simplifications have been used in the excitation method. As described in Chapter 2, usually in MFL, the magnetisation unit consists of a U shaped yoke with an electro magnet due to practical reasons. In this model, this U shaped magnetisation unit is ignored in modelling process and replaced with a homogeneous magnetic field parallel to the test substance which is not uncommon in literature [41] [62] [45]. This allows the forward model to have a constant magnetic charge density in the wall of the defect, as there is no yoke which can interfere.

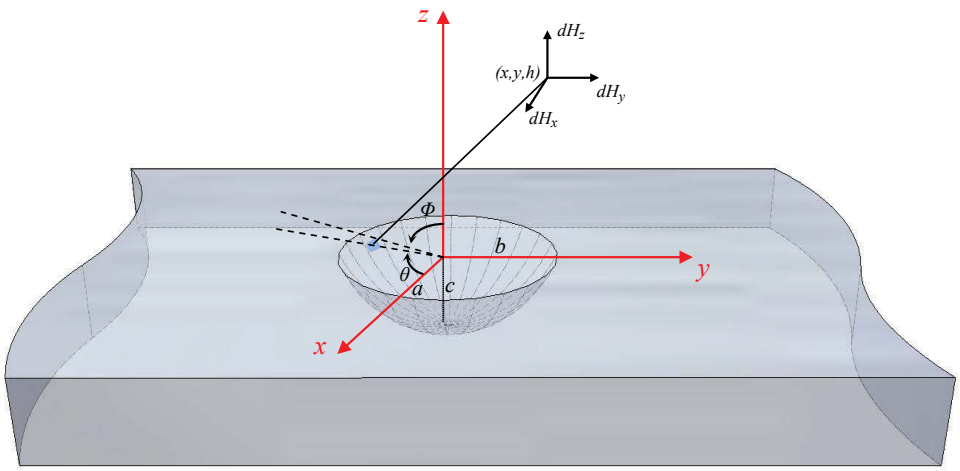

FIGURE 5.2: Dipolar magnetic charge model for an ellipsoidal defect

As schematically represented in Figure 5.2, an arbitrary ellipsoidal defect with ellipsoidal parameters, a, b and c has been introduced on a flat plate with its longitudinal axis (z-direction) perpendicular to the applied magnetic field (y-direction). The magnetic field lines diverge around the low permeability defect region, inducing a DMC on the walls of the defect. The surface of the test substance is defined by the xy plane at $z = 0$, with the top area of a ellipsoidal defect centred at $(0, 0, 0)$, and its bottom area centred at $(0, 0, -c)$, where c is the depth of the ellipsoidal defect. The MFL signal induced by the ellipsoidal defect is sampled in the region $z > 0$.

Half of the ellipsoidal defect develops a north polarity $(+\sigma)$, while the other half develops a south polarity $(-\sigma)$. The angle θ is measured from the positive x direction and the angle ϕ is measured from the positive z direction, to an element of magnetic charge, dp_1. Any arbitrary point on the ellipsoidal surface is given by the parametric equations as,

$$\begin{aligned} x &= a\cos\theta\sin\phi \\ y &= b\sin\theta\sin\phi \\ z &= c\cos\phi \end{aligned} \tag{5.1}$$

where $\theta \in [0, 2\pi]$ and $\phi \in [0, \pi]$.

The differential element of charge at the defect, dp, has coordinates (x, y, z) on the ellipsoidal surface of Equation 5.1 and a charge proportional to its area. Therefore,

$$dp = \mu_0.\mu_{rs}\sigma\sin\phi[a^2b^2\cos^2\phi + c^2\sin^2\phi(b^2\cos^2\theta + a^2\sin^2\theta)]^{1/2}d\theta d\phi \tag{5.2}$$

Now, the magnetic field (dH_1) generated at an arbitrary measurement point in a distance $\mathbf{r_1}$ from the element of charge dp is given by,

$$dH_1 = \frac{dp}{4\pi|r_1|^3}.\mathbf{r_1} \tag{5.3}$$

By keeping this arbitrary point at a constant height h above the defect surface, and by considering the positive polarity side H^+ of the defect, the axial component of the field H^{y+} at a given point (i, j) in a distance r_{1+} is given by,

$$H^{y+}_{(i,j)}(a,b,c) = \frac{\mu_0.\mu_{rs}\sigma \sin\phi[a^2b^2\cos^2\phi + c^2\sin^2\phi(b^2\cos^2\theta + a^2\sin^2\theta)]^{1/2}d\theta d\phi}{4\pi|r_1^+|^3}(j + b\sin\theta\sin\phi) \quad (5.4)$$

where,

$$r_1^+ = \sqrt{(i - a\cos\theta\sin\phi)^2 + (j + b\sin\theta\sin\phi)^2 + (h - c\cos\phi)^2} \quad (5.5)$$

The Equation 5.4 is integrated over θ from 0 to π and over ϕ from $\pi/2$ to ϕ to determine the total field at $\mathbf{r_1}$ due to the positively polarised side of the defect,

$$H^{y+}_{(i,j)}(a,b,c) = \int_{\pi/2}^{\pi}\int_{0}^{\pi} dH_y^+ d\theta d\phi \quad (5.6)$$

which leads to

$$H^{y+}_{(i,j)}(a,b,c) = \int_{\pi/2}^{\pi}\int_{0}^{\pi} \frac{\sigma \sin\phi[a^2b^2\cos^2\phi + c^2\sin^2\phi(b^2\cos^2\theta + a^2\sin^2\theta)]^{1/2}(j + b\sin\theta\sin\phi)}{4\pi[(i - a\cos\theta\sin\phi)^2 + (j + b\sin\theta\sin\phi)^2 + (h - c\cos\phi)^2]^{3/2}}d\theta d\phi \quad (5.7)$$

The same approach can be used to calculate the leakage field by the negatively polarised side of the cylinder. The only change is the opposite polarity and an appropriate y coordinate.

The negative polarity side leakage field H^{y-} of the defect is given by,

$$H^{y-}_{(i,j)}(a,b,c) =$$
$$-\frac{\mu_0.\mu_{rs}\sigma\sin\phi[a^2b^2\cos^2\phi + c^2\sin^2\phi(b^2\cos^2\theta + a^2\sin^2\theta)]^{1/2}d\theta d\phi}{4\pi|r_1^-|^3}(j - b\sin\theta\sin\phi) \quad (5.8)$$

where,

$$r_1^- = \sqrt{(i - a\cos\theta\sin\phi)^2 + (j - b\sin\theta\sin\phi)^2 + (h - c\cos\phi)^2} \quad (5.9)$$

The limits of the integral are kept the same, since all the angles and distances are measured in the same way as the positive side. Therefore, by using the same integration for the negatively polarised side H_z^- of the cylinder the total normal leakage field is given by,

$$H^{y-}_{(i,j)}(a,b,c) = \int_{\pi/2}^{\pi}\int_{0}^{\pi} dH_y^+ d\theta d\phi \quad (5.10)$$

which leads to

$$H^{y-}_{(i,j)}(a,b,c) =$$
$$\int_{\pi/2}^{\pi}\int_{0}^{\pi} -\frac{\sigma\sin\phi[a^2b^2\cos^2\phi + c^2\sin^2\phi(b^2\cos^2\theta + a^2\sin^2\theta)]^{1/2}(j - b\sin\theta\sin\phi)}{4\pi[(i - a\cos\theta\sin\phi)^2 + (j - b\sin\theta\sin\phi)^2 + (h - c\cos\phi)^2]^{3/2}}d\theta d\phi \quad (5.11)$$

Now the total leakage field is given by the addition of the positive and negative fields.

$$dH_{(i,j)}(a,b,c) = dH^{y+}_{(i,j)}(a,b,c) + dH^{y-}_{(i,j)}(a,b,c) \quad (5.12)$$

After the integration over the entire charged surface, the magnetic flux leakage $M_(i,j)$ in a given point (i,j) at a distance h above the defect is given by, (adding 5.7 and 5.11)

$$H_{(i,j)}(a,b,c) = H^{+}_{(i,j)}(a,b,c) + H^{-}_{(i,j)}(a,b,c) \tag{5.13}$$

The analytical model was implemented in MATLAB 8.2.0 . The model integrates over the scan window of the tool to compute the interested leakage field above a given ellipsoidal defect.

5.2.2 Formulation of the optimisation

The above derived model enables the generation of the leakage field for a given ellipsoidal defect. By using the realistic forward model, an iterative algorithm has been developed to solve the inverse model. Starting from an initial guess, the ellipsoid parameters were iteratively changed in the forward model to generate a matching leakage field to the measurement. Finding the optimal ellipsoidal parameters that minimise the model mismatch between the generated field and the measurement, is equivalent to solving the inverse problem of finding the ellipsoid that produces the most similar MFL measurement. This iterative optimiser is derived as follows.

The parameter vector is taken as $\gamma = (a, b, c)$, where a is the axially aligned major elliptic diameter, b is the circumferentially aligned minor diameter and c is the depth of the ellipsoidal defect. The framework is formulated as an unconstrained non-linear least mean square optimisation problem of the form,

$$f(\gamma) = \|H_{(i,j)}(a,b,c) - K_{ref}\|^2 \tag{5.14}$$

where $H_{(i,j)}(a,b,c)$ is a $n \times m$ matrix generated using the analytical model for a given $\gamma = (a,b,c)$ and K_{ref} is the measured leakage flux of the segmented area. Other methods such as Frobenius norm was also considered for the evaluation function but Equation 5.14 was selected as it had better representation of the problem along with good convergence properties. So the objective is to find the optimum γ that best fits $H_{(i,j)}$. *i.e.*

$$\gamma_{opt} = \arg min_{\gamma} f(\gamma) \tag{5.15}$$

A gradient based non linear optimisation algorithm has been used to solve the above formulation. In order to calculate the residual, the vector form of the matrices are used ignoring the spacial relationships. Let $h_i(a,b,c) = vec(H_{m\times n}(a,b,c))$ and $k_i = vec(K_{ref})$. Now the cost function can be simplified as,

$$min_\gamma\ f(\gamma) = min_\gamma \frac{1}{2}\|r(\gamma)\|^2 = min_\gamma \frac{1}{2}\sum_{i=1}^{m.n} r_i(\gamma)^2 \tag{5.16}$$

where $\gamma \in \mathbb{R}$ and

$$r_i(\gamma) = h_i(\gamma) - k_i,\ i = 1,2,...,m.n \tag{5.17}$$

For a gradient based optimisation, the gradient of $f(\gamma)$ needs to be derived for a given γ instance. The Jacobian $J(\gamma)$ of the vector function $f(\gamma)$ is defined as the matrix with elements,

$$[J(\gamma)]_{i,j} = \frac{\partial\ r_i(\gamma)}{\partial \gamma_j} = \frac{\partial\ h_i(\gamma)}{\partial \gamma_j},\ i = 1,2,...,mn, j = 1,2,3. \tag{5.18}$$

Therefore $J(\gamma)$ can be expanded as,

$$J^{[n]} = \frac{\partial\ vec(H_{m\times n}(\gamma))}{\partial \gamma} = \begin{bmatrix} \frac{\partial\ h_1(\gamma)}{\partial a} & \frac{\partial\ h_1(\gamma))}{\partial b} & \frac{\partial\ h_1(\gamma)}{\partial c} \\ \frac{\partial\ h_2(\gamma)}{\partial a} & \frac{\partial\ h_2(\gamma)}{\partial b} & \frac{\partial\ h_2(\gamma)}{\partial c} \\ \vdots & \vdots & \vdots \\ \frac{\partial\ h_{mn}(\gamma)}{\partial a} & \frac{\partial\ h_{mn}(\gamma)}{\partial b} & \frac{\partial\ h_{mn}(\gamma)}{\partial c} \end{bmatrix} \tag{5.19}$$

The i^{th} row of $J(\gamma)$ equals the transpose of the gradient of the gradient of $r_i(\gamma)$

$$[J(\gamma)]_{i,:} = \nabla r_i(\gamma)^T = \nabla h_i(\gamma)^T,\ i = 1,2,...,mn \tag{5.20}$$

Thus the elements of the gradient of $f(\gamma)$ are given by

$$[\nabla f(\gamma)]_j = \frac{\partial f(\gamma)}{\partial \gamma_j} = \sum_{i=1}^{m.n} r_i(\gamma) \frac{\partial\ r_i(\gamma)}{\partial \gamma_j} \tag{5.21}$$

and it follows that the gradient is the vector

$$\nabla f(\gamma) = J(\gamma)^T r(\gamma) \tag{5.22}$$

The algorithm employed is based on an optimisation approach that varies the parameter vector γ of the forward model which represents the geometric properties of the ellipsoidal defect on a flat gray cast iron plate. The formulated optimisation iterates until the model prediction best fits the given reference, in this case the measured field from the MFL tool. The idea is to iterate γ until the framework minimises the model mismatch between the generated field and the reference measurement.

A gradient based non linear optimisation algorithm has been used to solve the above formulation. Quasi-Newton optimisation methods are sequential line search algorithms. They are a variation of Newton's methods that still keep the good convergence properties but do not require Hessian computations and linear solvers. Similar to most of the gradient based algorithms Quasi-newton methods are iterative, involving a series of line searches and generally involve computations only of $f(\gamma)$ and $\bigtriangledown f(\gamma)$ at each iteration. For a given k^{th} iteration,

$$\gamma^{(k+1)} = \gamma^{(k)} - \alpha^k \delta^k \tag{5.23}$$

where,

$$\delta^k = [f''(\gamma_k)]^{-1} f'(\gamma_k) = H_k^{-1} g_k \tag{5.24}$$

is the direction which is a vector describing a segment of a path from the starting point to the solution where the inverse of the Hessian H_m determines the 'angle' of the direction

and the gradient g_m, determines its magnitude. α^m is the step length and is determined by the local optimisation of the function.

Derivation of the gradients $\bigtriangledown f(\gamma)$ and Hessian in this framework becomes rarely achievable because the Equation 5.13 is hardly derivable. Therefore in the implementation, the gradients were numerically calculated using the forward model. The calculation of the Hessian is very computationally expensive. However, efforts were made to find a way to approximate the Hessian less expensively. The critical insight from which came the current quasi-Newton methods was made by Broyden [79] who used information from the current iteration to compute the new Hessian. Let,

$$s^{(k)} = \gamma^{(k+1)} - \gamma^{(k)} = \alpha^{(k)}\delta^{(k)} \tag{5.25}$$

be the change in the parameters in the current iteration and,

$$\eta^{(k)} = g^{(k+1)} - g^{(k)} \tag{5.26}$$

be the change in gradients. Then a natural estimate of the Hessian at the next iteration $H^{(k+1)}$ would be the solution of the system of linear equations

$$H^{(k+1)}s^{(k)} = \eta^{(k)} \tag{5.27}$$

that is, $H^{(k+1)}$ is the ratio of the change in the gradient to the change in the parameters. This is called the quasi-Newton condition. There are many solutions to this set of equations.

Broyden [79] suggested a solution in the form of a second update

$$H^{(k+1)} = H^{(k)} + uv^t \tag{5.28}$$

Further work has developed other types of gradient updates, the most important of which are the DFP (for Davidon [80], and Fletcher and Powell [81]), and the BFGS (for Goldfarb [82], and Shanno [83]). The BFGS is generally regarded as the best performing method and was used in this implementation.

Algorithm 1 Quasi-Newton least squares method for ellipsoidal approximation

procedure
  Given prior $\gamma \in dom f, H_0 \succ 0$
  for each segmented defect region $K_{ref,i}$ **do**
    for until the termination criterion **do**
      compute quasi-Newton direction $\Delta\gamma = -H_{k-1}^{-1}\Delta f(\gamma^{(k-1)})$
      determine step size t (by backtracking line search)
      compute H_k
      compute $\gamma^{(k)} = \gamma^{(k-1)} + t\Delta\gamma$
      return $\gamma^{(k)}$
    end for
  end for
end procedure

The formulated optimisation iterates until the model prediction best fits the given reference, in this case the measured field from the MFL tool. Finding γ which minimises the model mismatch to the reference measurement, is equivalent to solving the inverse problem of finding the best ellipsoidal defect that produces the most similar measured magnetic leakage field. The same procedure is followed to all the segmented defects and one ellipsoid was approximated for each of them.

5.3 Results

The main objective of this chapter was to approximate ellipsoidal defects using MFL measurements. An analytical forward model based iterative framework was used for the approximation. The forward model needs to generate a realistic leakage field to the measurement field, and the accuracy of the method relies on a few factors such as the forward model, optimisation error tolerance and noise factors present in the MFL signal (See Section 3.3.5).

First the forward model was validated using a simulated perfect ellipsoid. A $3D$ COMSOL model was designed to simulate a perfect ellipsoidal defect. Figure 5.3 shows the simulated ellipsoidal defect and the tetrahedral mesh used.

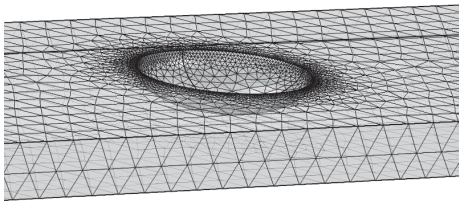

FIGURE 5.3: Perfect ellipsoidal defect simulated in COMSOL

The simulated leakage field can be considered as an ideal leakage field due to the non existence of lift-off errors, noise or tool localisation related practical issues. As the initial experiment, the simulated field was used as the reference field in the above framework. After the convergence of the optimisation, resulting γ values were compared with the ideal simulated values giving a good agreement. The convergence of the cost function and the results were compared with the GT is shown in Figure 5.4(a) and Figure 5.4(b) respectively.

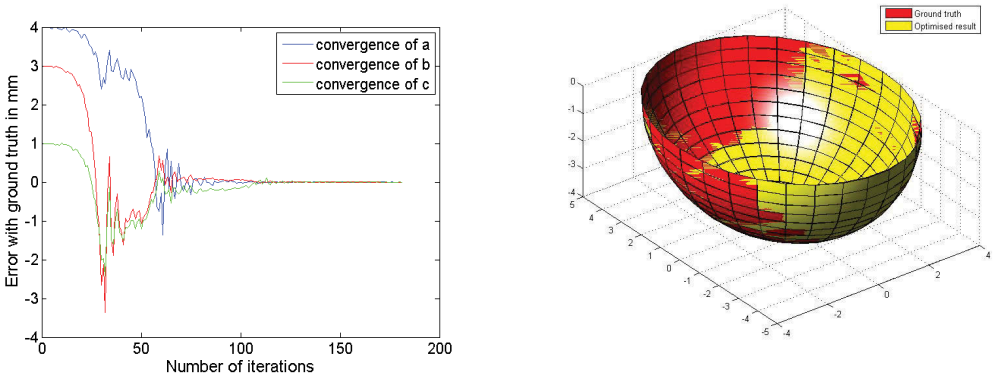

(a) (b)

FIGURE 5.4: Optimisation for simulated data: (a) Error variation over the iterations for each ellipsoidal parameter, (b) Converged result vs GT.

TABLE 5.1: Machined ellipsoidal defect approximation results

Machined Ellipoid	Axial major elliptic diameter (a)		Radial minor elliptic diameter (b)		Depth of the ellipsoid (c)	
	Laser based fit	Framework predicted	Laser based fit	Framework predicted	Laser based fit	Framework predicted
1	23.31mm	25.23mm	13.8mm	12.3mm	3.09mm	2.3mm
2	34.2mm	34.6mm	22.5mm	22.3mm	7.68mm	7.1mm
3	49.7mm	51.6mm	20.3mm	19.5mm	6.5mm	6.1mm
4	35.09mm	41.12mm	12.14mm	10.05	5.1mm	3.73mm

As shown in Figure 5.4 predicted ellipsoidal values converge to the real values due to ideal conditions. After the validation of the framework using simulation data, it was applied to the raw data collected from the industry tool.

FIGURE 5.5: Machined ellipsoidal defects

Four ellipsoidal defects were machined on a grit-blasted pipe (Figure 5.5). Pre-designed ellipsoids were machined manually on the pipe by an experienced operator up to the best possible accuracy using a range of power tools. Industrial MFL tool was used to raster scan the machined area and raw data was used in the framework. Only a segmented ROI of the full pipe scan as well as the appropriate calculated leakage field was used in the cost calculation. Table 5.1 summarises the prediction results for machined defects.

It is observed that the prediction values are not as accurate as the simulated ellipsoids. One of the major reasons identified is the imperfections of machining the ellipsoids on the pipe. Given the manual process of machining, even an experienced operator is limited to

the tool capacity and human error. In order to quantify the imperfections of the machined ellipsoids, they were $3D$ laser scanned. Laser scanned outer surface is shown in Figure 5.6.

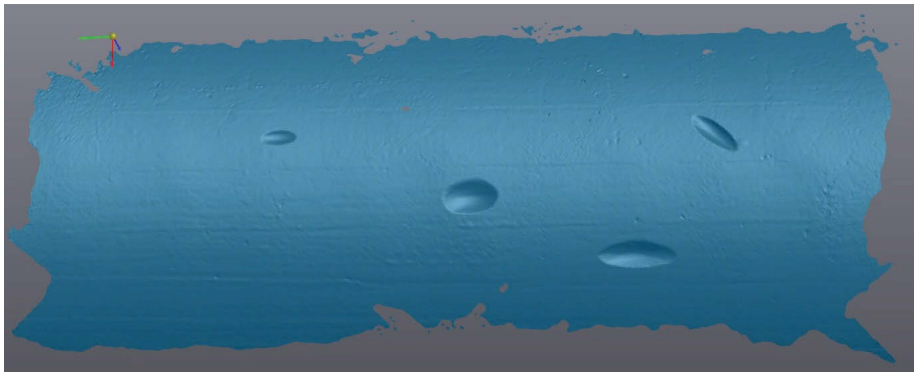

FIGURE 5.6: Laser scan of machined ellipsoidal defects

In Table 5.1, the laser based least squares fit is used to compare the prediction values. The point cloud generated from the $3D$ laser scanner was analysed to isolate the ellipsoids and a perfect half ellipsoid was fitted using least squares optimisation. These fitted ellipsoid parameters are used as the best reference values and compared with the prediction values. An example of point cloud based ellipsoidal fit for the machined ellipsoid 3 (as shown in Figure 5.5) is shown in Figure 5.7.

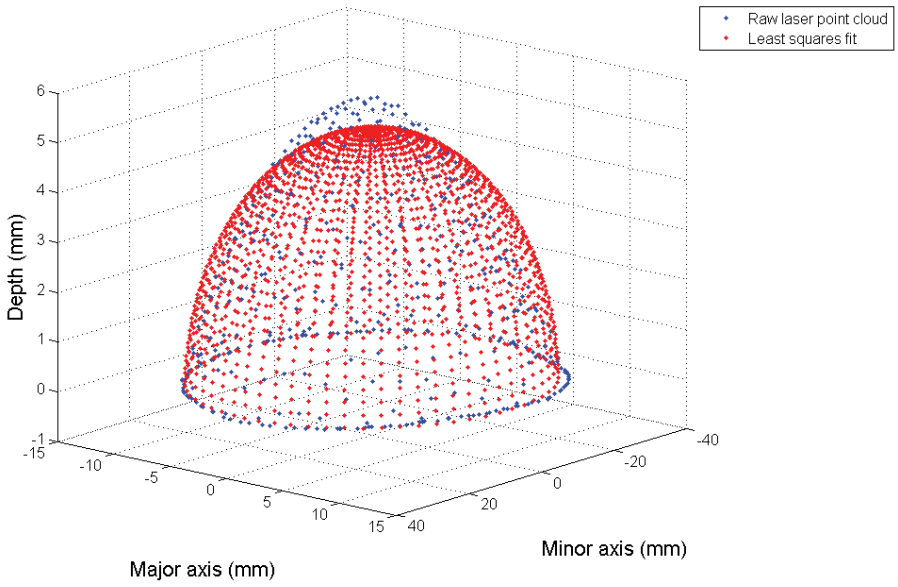

FIGURE 5.7: Ellipsoid fitting for laser point cloud data

This analysis shows the imperfections in the machining process. Furthermore some other error sources can be identified which were not present in the simulation study. Laser scanner is a surface scanner whereas MFL is influenced by defects inside the pipe material such as air bubbles. When it comes to millimetre level accuracy these imperfections could affect the end result.

The industrial MFL tool takes discrete samples over the scan length. The axial samples are taken at every 2.8mm and circumferential samples are taken at every 10.62mm. Therefore the resolution of the sensor becomes a major limitation. Although the framework best fits the curvature to the available samples, more accuracy could be achieved with lesser sampling intervals.

Experimental evaluation of the framework was further extended by applying it to the real corroded CI pipes. The full pipe scan was segmented to select the outstanding defect areas in raw data using a simple level set algorithm. Each segmented ROI of the full pipe scan as well as the appropriately calculated leakage field was then used in the iterative framework. The framework approximates an ellipsoid to the measured MFL data.

After the convergence of the cost function, the reference leakage field and the model output comes to an agreement. Comparison of the measured segmented raw signal and the optimised leakage field is shown in Figure 5.8(a).

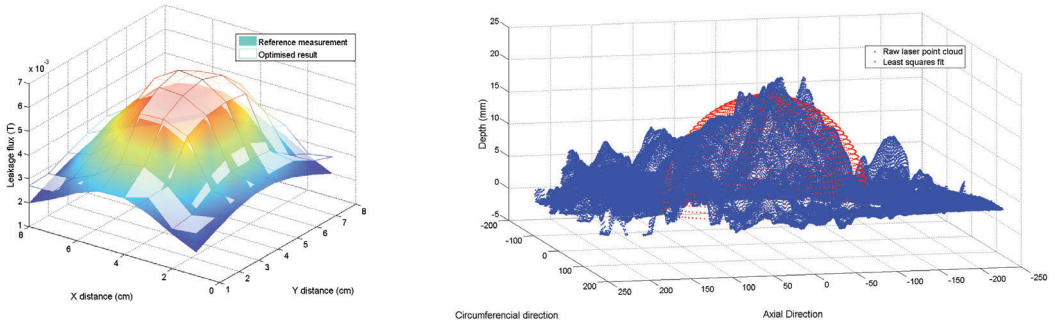

(a) (b)

FIGURE 5.8: Ellipsoidal optimisation results: (a) Comparison of measured and optimised leakage fields, (b) Least squares ellipsoidal fit on real GT .

Evaluation of the results was a challenging task due to the non-existence of an obvious ellipsoidal defect in the ground truth. As a result, a similar approach as described above

Table 5.2: Natural ellipsoidal defect approximation results

	Axial major elliptic diameter(a)	Radial minor elliptic diameter (b)	Depth of ellipsoidal defect (c)
Laser based fit	125.1mm	64.4mm	18.14mm
Framework predicted	119.6mm	57.7mm	21.3mm

for the ellipsoidal point clouds was followed. The $3D$ point cloud of the appropriate GT ROI was analysed to fit a half ellipsoid using least squares optimisation (See Figure 5.8(b)). This fitting result can be then compared to the framework approximation.

Although there are no obvious ellipsoids in the real corroded thickness profile, the least squares match can be considered as the best fit for a perfect ellipsoid. Although SCF analysis is not the focus of this thesis, the errors should be analysed in the form of stress deviations. However, given the $660mm$ diameter pipe, it can be considered that the approximation results are a close match. Calculated ellipsoidal parameters then can be used for subsequent stress analysis.

5.4 Discussion and Chapter Conclusion

Ellipsoidal defects on CI pipes are prone to failures by the maximum stress development. Therefore detection and approximation of ellipsoidal defects on aged CI pipes was the main focus of this chapter. An analytical model to generate the leakage field for a given ellipsoid defect was developed as part of the proposed iterative method. The ellipsoidal parameters were iteratively changed to generate a leakage field that best fits the measurement.

The framework was first validated using FEA simulated perfect ellipsoidal defects. Later four different sized ellipsoidal defects were machined on a grit-blasted pipe and used to collect data. The model predictions were close to the real measurements given the imperfections in machining and measurement errors. The framework was further evaluated on real aged CI pipes.

A few limitations of the proposed method can also be identified. Deepest points in general natural corrosion pits cannot be always in the centre; this is also found true for the

maximum tensile stress generation, generally not appearing at the centres of the natural pits [78]. This can be reflected via advanced FEMs using a hyperbolic non-linear constitutive model for cast iron pipes [23]. Nonetheless, these are beyond the scope of the analytical model where it assumes an ideal ellipsoid with the deepest point in the centre. The analytical solution is dependant on an equivalent approximated ellipsoid where the deepest point is, naturally, at the centre of the pit. This solution is not intended to locate the accurate position where the deepest point of a real pit is; but attempts to aid the calculation of magnitude of the maximum tensile stress calculations [23] within the studied natural pits.

Despite these limitations, the proposed framework approximated the ellipsoid defects on the aged pipe surface in a computationally efficient manner giving promising results.

Rather than approximating isolated defect shapes, further analysis has been carried out to study the possibility of generating dense $2.5D$ thickness maps using MFL data. A moving window based iterative optimisation framework has been developed to sequentially solve the entire thickness profile. The next chapter focuses on this framework which attempts to reconstruct $2.5D$ thickness maps using MFL data.

Chapter 6

Reconstruction of Dense 2.5D Thickness Maps using MFL Measurements

6.1 Introduction

By further investigating the MFL signals it is identified that the MFL signal itself has more information to infer the entire thickness map of the area. GP is a kernel based method and it enables flexible modelling which is more suitable for practical applications. However, due to the non uniqueness of the MFl signal, it becomes challenging for data driven methods to estimate thickness maps. These methods are well suited to predict a geometrical defect in the presence of a peak in the MFL signal [22]. Therefore the measle plots generated in Section 4.5.2 are limited to the combination of individual defects.

Using the estimated GP based profile as a prior, a coarse to fine approach is formulated. An iterative non-linear optimiser is employed as the basis of the framework. Once the initial estimated profile is given to the optimiser, it calls a FEA based COMSOL simulator to generate the appropriate MFL response. This response is then compared against the original measurement of the experimental set-up.

By analysing the previous iterations and the current error, the optimisation algorithm generates a temporary defect profile for the next iteration, which is again used in the simulator. Given the initial profile is a reasonable approximation, this iterative process converges to a near optimal solution giving a better fine interpretation of the defect profile. An overview of this framework is shown in Figure 6.1.

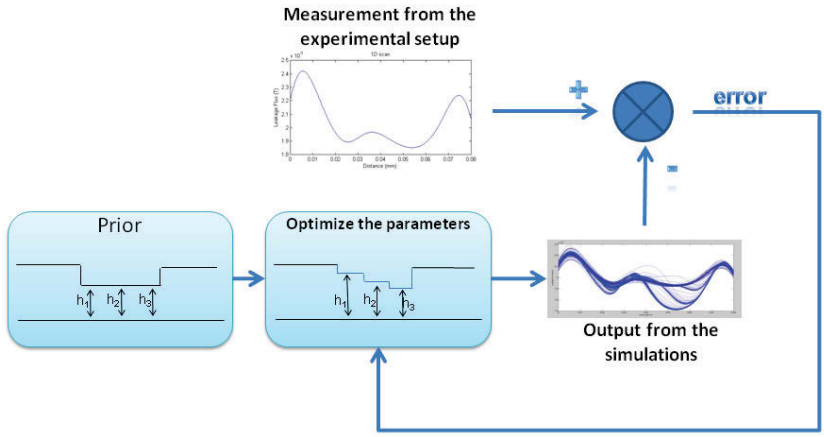

FIGURE 6.1: Iterative framework to optimise the thickness profile

6.2 Formulation of the Optimisation Problem

The industrial MFL tool has been used to scan 360^0 of a $1m$ long aged cast iron pipe. For each circumferential location, the tool moves from left to right towards the flow, recording the leakage measurement for each sampling point. Given this measurement, the idea is to generate the pipe RWT profile using a non-linear optimiser. After scanning, the pipe has been grit-blasted and 3D laser scanning procedure has been followed as described in Section 4.4.3. Later measured ground truth has been used to evaluate the estimation results.

A coarse to fine approach has been developed using an optimisation algorithm that varies the RWT profile of the forward model starting from a given prior. The forward model generates the MFL leakage field for a given RWT profile. The optimisation algorithm iterates until the forward model prediction best fits the reference signal, in this case the original measured MFL signal. Finding the thickness profile that minimises the model

mismatch to the reference measurement, is equivalent to solving the inverse problem of finding the profile that produces the most similar measured MFL signal.

6.2.1 Forward Model Formulation

With the above description, it is clear that the forward model performs a crucial role in the proposed framework. The model should generate a rational MFL signal that matches the signal measured on the pipe. An aged, corroded pipe wall can be very irregular which makes it harder and more complex to model. Non-linearity of the pipe material as well as the tool specific properties has to be captured in generating a realistic MFL signal. As Chapter 3 described, the COMSOL Multiphysics® [65] FEA based simulation model developed, best suits the purpose. The model is capable of producing the leakage field for a given irregular profile with a cost of computational time according to the level of details in the profile.

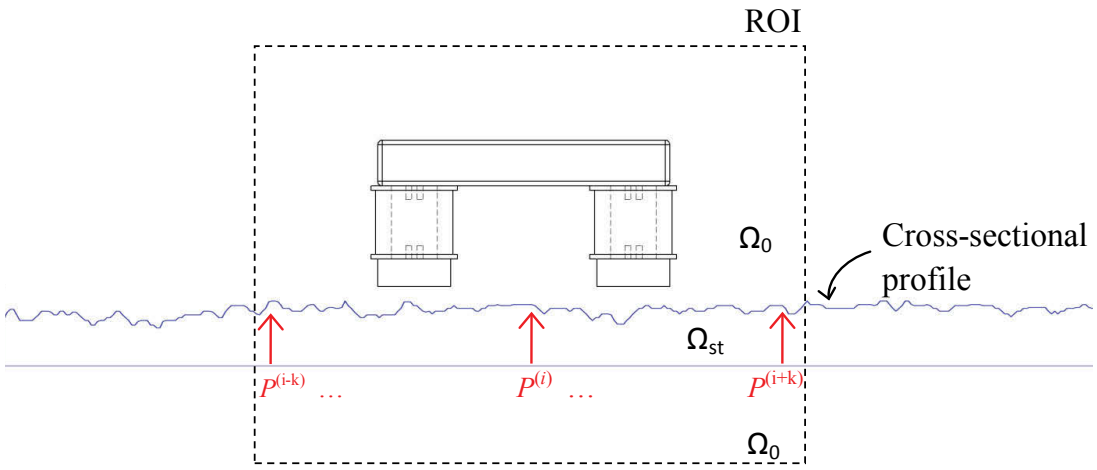

FIGURE 6.2: Truncating the infinite domain to ROI

In order to resemble the scanning procedure, a ROI has to be selected for each location of the tool and has to be moved from left to right along with the tool. In the simulation model, it has truncated the infinite domain Ω^{∞} at a finite distance sufficiently far from the region of interest (ROI) and created the model domain $\Omega \subset \Omega^{\infty}$. Its also has to be considered that $\Omega = \Omega_0 \cup \Omega_{st}$ consists of two homogeneous materials; air in Ω_0 with

absolute permeability $\mu = \mu_0$ and a non-linear gray cast iron material in Ω_{st} with absolute permeability $\mu = \mu_0\mu_{rs}(H)$. The B-H curve in Figure 3.9 for gray cast iron is used to capture the non-linear properties of the material.

To simplify the remaining wall thickness of the profile, it has been discretised to N samples over the axial direction. The discrete depth profile $P[n] = P[1], P[2], ..., P[N]$ approximates the profile of a given cross section of the pipe wall.

For a given circumferential location, ROI moves along the axial distance resembling the scan direction towards the flow of the pipe. As the ROI moves with the iteration i, the tool moves along as well keeping the centre of the tool, where the hall sensors are, accurately on top of the i^{th} sample of the thickness profile. In order to get the full measurement curve, the tool has to move all the way from the left most location to the right most location, i.e, $(i = 1 \; to \; N)$. Each i^{th} sample of the simulated measurement is an individual simulation result, which makes N number of simulations for a single iteration of the optimisation cycle.

An optimisation cycle can go up to a few hundreds of iterations depending on the dimensionality of the problem and termination criteria. A single $3D$ MFL COMSOL simulation can take up to even 1 hour of computation time depending on the mesh size in a modern HPC. A full 360^0 $660mm$ diameter pipe scan has about 192 axial scans, which means 192 different circumferential locations. If there is 100 sampling points per scan, it could take up to 800 days for a 1m section. Considering the computational time required, it is infeasible to optimise a full 360^0 pipe profile without any further simplifications.

6.2.2 Forward Model Simplifications

One of the major simplifications done is to employ $2D$ simulation instead of $3D$. A simulation with a real $3D$ laser profile even with an ROI was very computationally intensive. A $200mm \times 500mm$ down sampled ground truth to 10mm resolution had 88905 $3D$ free tetrahedral mesh elements and 564906 degrees of freedom and took about 15 minutes per single simulation. which is a 75% saving in terms of computation time.

This computational time can be exponentially decreased by using a $2D$ simulation. $3D$ pipe wall has been decomposed into cross sections with a given sampling interval and used in the simulation model. In order to validate this approach a pilot experiment has been carried out to simulate the same defect profile in 2D and 3D. These curves gave a good agreement between each other; see Figure 6.3 below.

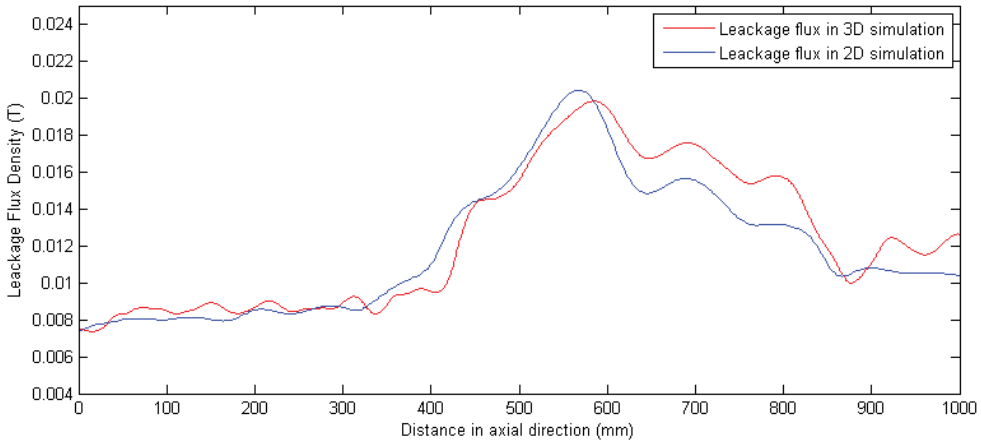

FIGURE 6.3: 2D and 3D Simulation comparison signals

One of the reasons for this observation is that the applied magnetic field is very strong in the axial direction. Most of the flux is directed towards the other magnetic pole axially creating leakages with respect to the profile variations in the axial direction. Therefore profile variations in the circumferential direction has minimal effect on the axial component of the leakage signal which is measured. Moreover profile variations in the circumferential direction itself are minimal. This property is further analysed in the next Section 6.3.

As discussed before in this section, the simulation model resembles the measurement signal by moving the tool from left to right with the iteration number where each iteration simulates one sample of the measurement signal. This procedure makes it very computationally intensive to generate the measurement curve for one given cross-sectional profile. The U shaped yoke with electro-magnets which generate the excitation field is removed from the model by introducing a strong magnetic field (ideally homogeneous) as in [39],[41],[44] and [45]. This simplification allows the generation of the entire MFL signal for a given cross sectional profile from a single FEA forward solution, as there is no magnetic yoke

which would interfere and would have to be moved. This simplification saved a remarkable amount of the computational power requirement. As long as the magnetic shoe is not very close to the hall sensor position, in this case about $150mm$ to the closest shoe, it can be assumed that the magnetic flux lines are spread parallel and homogeneously in the pipe material and are similar to an external homogeneous excitation field. This is further validated by a simple experiment too.

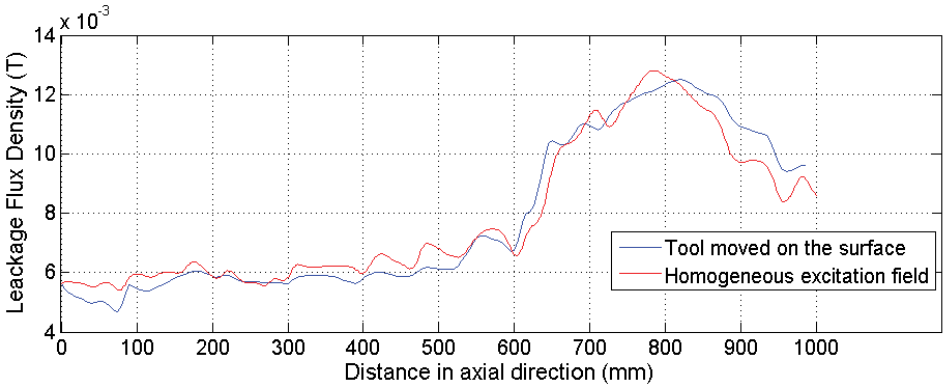

FIGURE 6.4: Tool moved signal vs Homogeneous excitation field

The U shaped magnetic element has been moved in the simulation environment in a cross sectional profile taken from the laser ground truth. The samples of the leakage curve have been recorded for each location for the entire cross section profile of $1m$ length. Later a constant homogeneous field was applied to the entire $1m$ profile and an array of hall sensors were simulated above the pipe surface. With the array of sensors the entire 1m long MFL signal was captured in one forward model solution. As shown in Figure 6.4 both of these signals are very close to each other.

In formulating the optimisation criteria further simplifications have been used. The laser based GT had a resolution of 2230×5184 axially and circumferentially. Solving the profile for that resolution means the dimensionality of the problem for a given cross sectional profile becomes the number of samples in a axial profile; in this case 2230. This very high dimensionality exponentially increases the computational power requirement. Therefore the profile has needed to be down-sampled. Further to the down sampling, the MFL signal behaviour was analysed to simplify the optimisation procedure.

With the understanding of the utility partners and stress analysis requirements a minimum resolution of 10mm was selected. Even with 100 samples per 1m, the dimensionality of the

optimiser becomes too high. And also it is challenging to derive the cost function which is descriptive enough for a wide scan range. Therefore the ROI has been limited and moved along the cross section to solve for the thickness profile.

Consider the general cross sectional profile is given by $P[n] = P[1], ..., P[i], ..., P[N]$. In this case $N = 100$. For simplification the tool response signal $f(P[n])$ is also sampled to have the same number of samples as the cross sectional profile $P[n]$.

The following analysis shows that the i^{th} sample of the cross sectional profile $P[i]$ has the most influence on the tool response signal $f(P[n])$ only for a limited range centred at $f(P[i])$. Other close-by samples to $P[i]$ have minimal influence on $f(P[i])$. This property has been used to further simplify the optimisation formulation.

The analytical model developed in Section 3.2 for cylindrical defects is extended for the justification of the above simplification. Figure 6.5 shows a close-up of the discretised defect profile which is approximated to be a multiple combination of cylindrical defects. The leakage signal $f(P[n])$ is captured above the centres of the cylindrical defects.

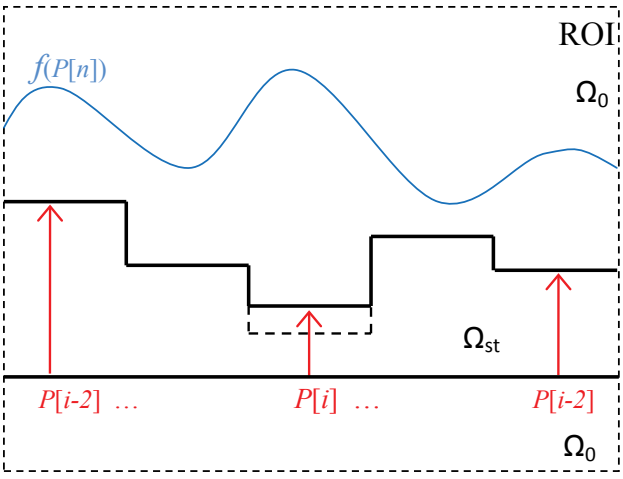

FIGURE 6.5: Close-up of the discretised defect profile

Considering a depth profile is a combination of multiple defects, the effect of each of their individual axial leakage fields $(H_{y,P[1]}, ..., H_{y,P[N]})$ on a given i^{th} measurement point adds together to form the final response signal magnitude $f(P[i])$.

$$f(P[i]) = H_{y,P[1]} + .. + H_{y,P[i]} + ... + H_{y,P[N]} \tag{6.1}$$

Now only the depth value of the i^{th} sample of the profile has been changed to $P'[i]$ keeping the rest of the profile unchanged. Ideally, new measurement at the i^{th} location is given by,

$$f'(P[i]) = H_{y,P[1]} + .. + H_{y,P'[i]} + ... + H_{y,P[N]} \tag{6.2}$$

The difference in the measurement value is given by the difference of Equations 6.1 and 6.2. The resulting change in the measurement is given by,

$$\Delta f(P[i]) = f(P'[i]) - f(P[i]) = H_{y,P'[i]} - H_{y,P[i]} \tag{6.3}$$

Using the Equation 3.5 and 3.9

$$\Delta f(P[i]) = \left\{ \int_0^{\pi} \int_{P'[i]}^{0} dH^{+}_{y,P'[i]} dz_1 d\theta_1 + \int_0^{\pi} \int_{P'[i]}^{0} dH^{-}_{y,P'[i]} dz_1 d\theta_1 \right\} - \left\{ \int_0^{\pi} \int_{P[i]}^{0} dH^{+}_{y,P[i]} dz_1 d\theta_1 + \int_0^{\pi} \int_{P[i]}^{0} dH^{-}_{y,P[i]} dz_1 d\theta_1 \right\} \tag{6.4}$$

Since all the other parameters are kept unchanged the Equation 6.4 simplifies to,

$$\Delta f(P[i]) = \left\{ \int_0^{\pi} \int_{P'[i]}^{P[i]} dH^{+}_{y,P'[i]} dz_1 d\theta_1 + \int_0^{\pi} \int_{P'[i]}^{P[i]} dH^{-}_{y,P'[i]} dz_1 d\theta_1 \right\} \tag{6.5}$$

where,

$$dH^{+}_{y} = \frac{\mu_0 . \mu_{rs} \sigma R_1 d\theta_1 dz_1}{4\pi |r_1^{+}|^3} (y + R_1 sin\theta_1) \tag{6.6}$$

$$dH_y^- = -\frac{\mu_0.\mu_{rs}\sigma R_1 d\theta_1 dz_1}{4\pi|r_1^-|^3}\,(y - R_1 sin\theta_1) \tag{6.7}$$

$$r_1^+ = \sqrt{(R_i cos\theta_1)^2 + (y + R_i sin\theta_1)^2 + (h - z_1)^2} \tag{6.8}$$

and

$$r_1^- = \sqrt{(R_i cos\theta_1)^2 + (y - R_i sin\theta_1)^2 + (h - z_1)^2} \tag{6.9}$$

with the same definitions of the other parameters as described in Section 3.2.

Now the idea is to find the range of influence of $P[i]$ on the measurement signal and thereby reduce the dimensionality of the optimisation problem. For any $\Delta P[i]$ the leakage field change along the axial direction y is given by the Equation 6.5. In order to compare all the $\Delta f(P[j])$ values along the y axis it is divided by the measurement precisely on top of $P[i]$; $f[i]$. This ratio $R[j]$ is given by,

$$R[j] = \frac{\Delta f[j]}{\Delta f[i]} \tag{6.10}$$

The $R[j]$ ratio can be analytically derived using Equations 6.5 to 6.9.

$$R[j] = \frac{\int_0^\pi \int_{P'[i]}^{P[i]} \frac{(y+sin\theta_1)}{\left\{(Rcos\theta_1)^2+(y+Rsin\theta_1)^2+(h-z_1)^2\right\}^{\frac{3}{2}}} dz_1 d\theta_1 - \int_0^\pi \int_{P'[i]}^{P[i]} \frac{(y-sin\theta_1)}{\left\{(Rcos\theta_1)^2+(y-Rsin\theta_1)^2+(h-z_1)^2\right\}^{\frac{3}{2}}} dz_1 d\theta_1}{\int_0^\pi \int_{P'[i]}^{P[i]} \frac{2(sin\theta_1)}{\left\{(Rcos\theta_1)^2+(Rsin\theta_1)^2+(h-z_1)^2\right\}^{\frac{3}{2}}} dz_1 d\theta_1} \tag{6.11}$$

where the measurement range y is the distance between centres of $P[i]$ and $P[j]$.

A histogram analysis has been conducted to study the variation of realistic thickness variation along the x axis. The full dense $2.5D$ thickness map was sampled for the $10mm$

resolution selected above *i.e.* $R = 5mm$. Figure 6.6 shows the histogram of the adjacent axial thickness difference on real GT.

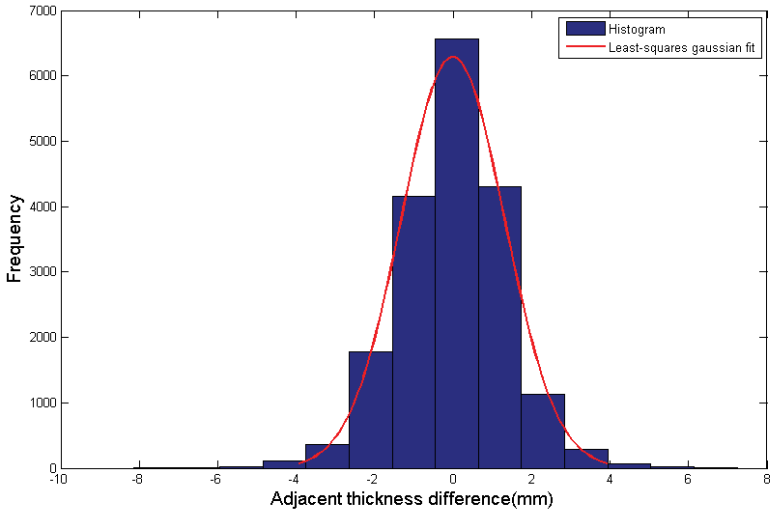

FIGURE 6.6: Axial thickness difference variation and Gaussian fit

The above histogram shows that, although ideally adjacent thickness values can vary the full range, which is 0 to $30mm$ for a $660mm$ CI pipe, the reality is a narrow range; 0 to $4mm$. Therefore $\Delta P[i]$ variation can be narrowed down for all possible depth values from 0 to $4mm$. The exhaustive study on Figure 6.7 shows the variation of $R[j]$ ratio against measurement range y and depth difference $\Delta P[i]$. R is the radius/width of defects.

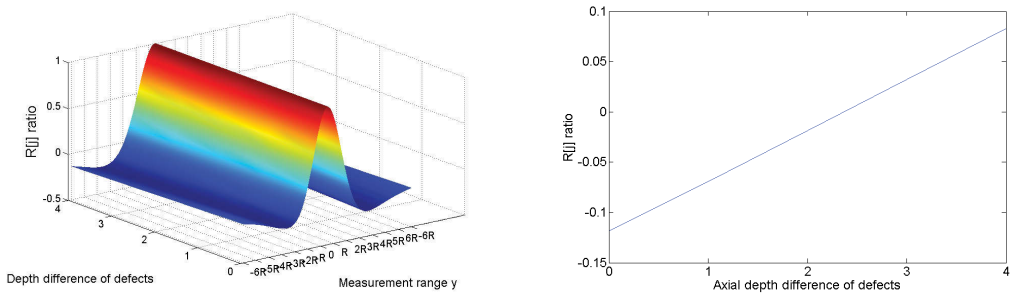

(a) (b)

FIGURE 6.7: R[j] ratio variation: (a) $R[j]$ ratio variation with scan range and depth difference of defects, (b) R[j] ratio variation at 2R distance with depth difference of defects.

The influence of the depth change exponentially drops as the measurement range increases as well as when the depth difference decreases. As illustrated in the above exhaustive analysis, it is evident that the effect of a given defect is significant only within $\pm R$ range

which is only above the current defect. When the measurement point goes to $2R$ the influence becomes negligible (Figure 6.7(b)).

Not only a single defect, multiple defect scenarios are also considered to confirm the above observation. Since there are an infinite number of multi-defect configurations a worst case analysis has been conducted. Worst signal variations between $f(P[i])$ and $f'(P[i])$ compared to an isolated defect were observed in the following scenario shown in Figure 6.8. Qualitatively the variation was 12.13%. Even with rather a high percentage variation, the optimisation framework could converge on the right defect profile and the results are demonstrated in Section 6.4.

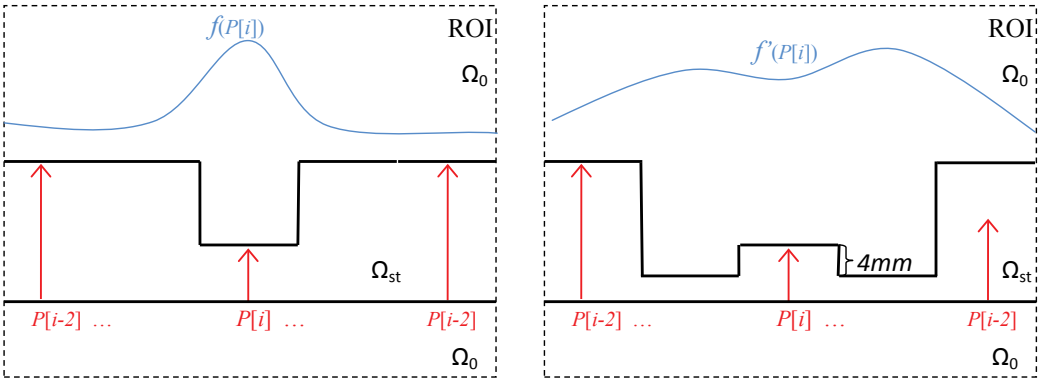

(a) (b)

FIGURE 6.8: Worst case analysis on signal variation: (a) Original isolated defect, (b) Introduced two deep defects observed to be the worst case.

This observation is further extended to narrow down the region of influence and hence reduce the dimensionality of the optimisation. Since the range of influence for a given defect lies only above the defect, for a given iteration, only one defect can be altered to match the measurement signal on top of the defect. So for a given profile and for a given iteration, the optimisation can be formulated to be a single dimension optimisation.

COMSOL Multiphysics® [65] FEA based simulation model developed in Section 3.3.2 has been configured to generate the response signal $f[n] = f(P[1], ..., [i], ..., P[N])$ for a given profile $P[n] = P[1], ..., [i], ..., P[N]$.

The experimental tool measurement $(g[n] = g^{(1)}, g^{(2)}, ..., g^{(M)})$ on the pipe surface has a different sampling rate but corresponds to the same scan length . For example the industry

tool takes 349 ± 5 equally distributed samples per 1m scan. An optimisation problem can be formulated such that $P[n]$ is altered until $f(P[n])$ comes to an agreement with $g[n]$.

With the above simplifications, for a given i^{th} location of the ROI only $P[i]$ was altered to get the best fit between $f(P[n])$ and $g[n]$. For the i^{th} location only the range of influence derived above was considered for the cost calculation. Iteratively optimising the individual sample over the whole profile is equivalent to solving the full profile. The algorithm iterates over the same profile multiple times until the model prediction best fits the given reference, in this case the measured field from the MFL tool, $g[n]$.

Taking the parameter vector as $\gamma = P[i]$, and the sample range corresponding to the $\pm 2R$ sensitivity range is $\pm k$ for $f[n]$ and $\pm m$ for $g[n]$, the optimisation is formulated as an unconstrained least mean square optimisation of the form,

$$f(\gamma) = \|f(\gamma) - g[i-m, ..., i+m]\|^2; \ \forall i = 1, ..., N \tag{6.12}$$

$$\gamma_{opt} = \arg min_{\gamma} f(\gamma); \ \forall i = 1, ..., N \tag{6.13}$$

where $f(\gamma)$ is the function to be minimised, $g[i-m, ..., i+m]$ represents the measurement signal over the $\pm 3R$ influence range and $f(\gamma)$ denotes the FEM model prediction of those measurements.

A similar gradient based non linear optimisation algorithm described in Section 5.2.2 has been used. Quasi-Newton optimisation methods are a variation of Newton's methods that still keep the good convergence properties but do require Hessian computations and linear solvers. Similar to most of the gradient based algorithms Quasi-newton methods are iterative, involving a series of line searches and generally involve computations only of $f(\gamma)$ and $\bigtriangledown f(\gamma)$ at each iteration. For a given k^{th} iteration,

$$\gamma^{(k+1)} = \gamma^{(k)} - \alpha^k \delta^k \tag{6.14}$$

where

$$\delta^k = [f''(\gamma_k)]^{-1} f'(\gamma_k) = H_k^{-1} g_k \tag{6.15}$$

is the direction which is a vector describing a segment of a path from the starting point to the solution where the inverse of the Hessian H_m determines the 'angle' of the direction and the gradient g_m, determines its magnitude. α^m is the step length and is determined by the local optimisation of the function.

Derivation of the gradients $\bigtriangledown f(\gamma)$ and Hessian in this framework becomes rarely achievable because the COMSOL based model interface does not provide gradient information. Therefore in the implementation, the gradients were numerically calculated using the forward model. The calculation of the Hessian is very expensive computationally, but similar to the Section 5.2.2 the BFGS (for Goldfarb [82], and Shanno [83]) method was used in the implementation.

Algorithm 2 Quasi-Newton least squares method to generate thickness maps

```
1: procedure
2:     for until all circumferencial locations are solved do
3:         for until all axial locations P[i] ∀i = 1toN are iteratively solved 3 times do
4:             Given prior γ ∈ domf, H_0 ≻ 0
5:             for each location k ∈ N until the termination criterion do
6:                 compute quasi-Newton direction Δγ = −H_{k−1}^{−1} Δf(γ^{(k−1)})
7:                 determine step size t (by backtracking line search)
8:                 compute H_k
9:                 compute γ^{(k)} = γ^{(k−1)} + tΔγ
10:                return γ^{(k)}
11:            end for
12:        end for
13:    end for
14: end procedure
```

Once all the iterations from $i = 1$ to N are complete, tool location is set back to the initial location to run the profile again. This is iteratively done multiple times with a maximum limit set to three, until a stable solution is found.

The above framework iterates until the model prediction best fits the given reference, in this case the measured field from the MFL tool. Finding γ which minimises the model mismatch to the reference measurement, is equivalent to solving the inverse problem of

finding the best remaining wall thickness value that produces the most similar measured magnetic leakage field.

ROI sweeps over the full cross-sectional profile and over all the cross sections. By arranging the fulls set of solved cross sections, the dense $2.5D$ thickness map of the scan area is generated.

6.3 Prior Generation

The initial guess used in the framework can influence the computation time as well as the end result. A careful analysis has been conducted to use the best suitable priors for this framework. The cylindrical approximations generated using the GP model were initially considered to be used as the prior. The validated simulation model and interpretation framework developed in Section 4.4 has been used to generate the prior. Since the GP model approximates the thickness profile as a multiple combination of cylindrical defects an example of the approximated prior is observed as shown in Figure 6.9.

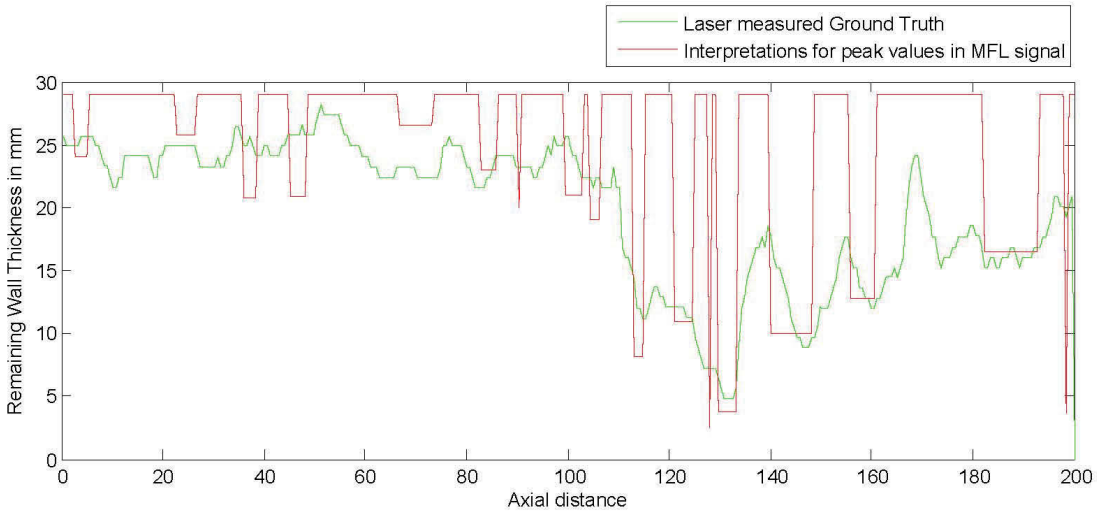

FIGURE 6.9: GP inference based prior

The measle plots are proven to produce close guesses to the deepest point of defects. Generation of these approximated profiles is computationally very fast too. However, the main disadvantage of using the approximations as the profile prior is that they lack information about the non-defect regions of the pipe. This makes the total number of iterations higher

for every cross-section. Given the fact that each iteration is computationally expensive using GP based measles approximated profiles as prior required an overall higher processing time.

By analysing the ground truth of a naturally corroded aged gray cast iron pipe, it is noted that consecutive cross sections do not have abrupt changes, unless there is a sharp pitting defect. Figure 6.10 shows an example of three adjacent cross sections.

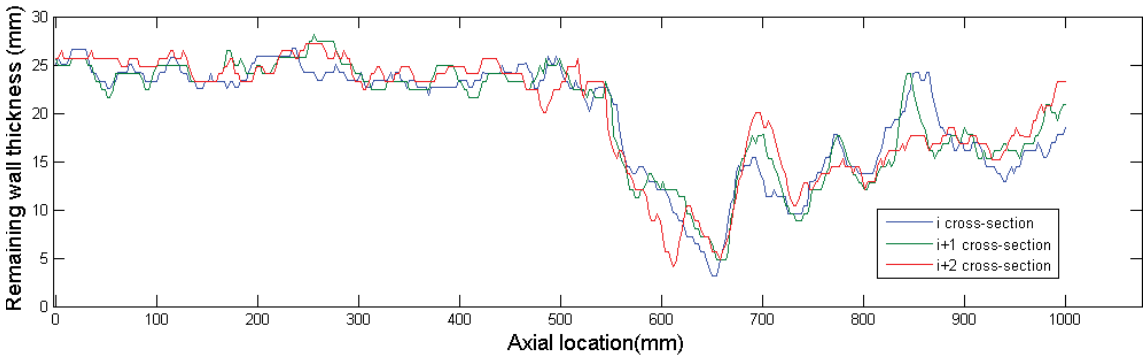

FIGURE 6.10: Adjacent cross sectional difference

Although there is a significant difference after about 500mm where the major defects are, the rest of the profiles are very similar to each other. This is about 50% of the profile in this example. This property is further analysed to be used in the prior generation process. Figure 6.11(a) shows the $2.5D$ thickness map of Trial 2 pipe section 3 and Figure 6.11(b) shows the difference between adjacent cross-sections of the entire 360^0 profile.

By generating the histogram of the difference between adjacent profiles this property is validated. 81.26% of the points were within $\pm 2mm$ difference of each other. The histogram for the absolute cross-sectional difference is shown in Figure 6.12.

This analysis shows that to use the full or a proportion of previous profile as the initial guess for the next profile is a reasonable approach. Since the MFL response has a direct correlation to the thickness profile, difference in adjacent MFL signals resembles a difference in the thickness profile. A tolerance level of 5% of the original MFL signal magnitude was used as the threshold to replace the current thickness with the previous adjacent thickness. So only the first ever initialisation used the GP based profile and after that the previous profile was used to initialise the iterative process. As Figure 6.10 shows, this

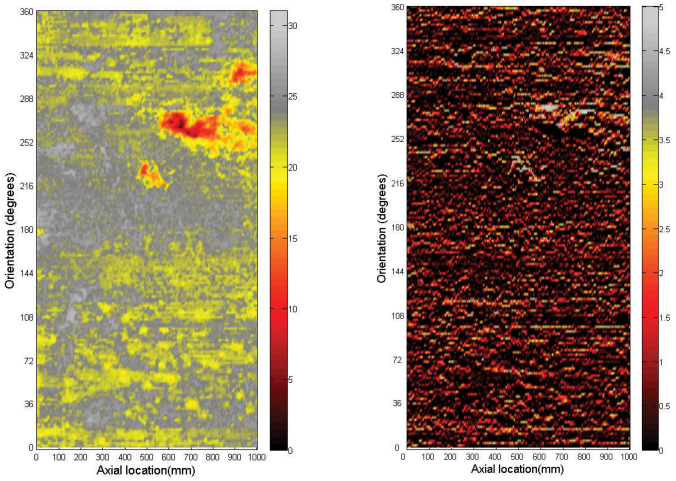

(a) (b)

FIGURE 6.11: Difference between adjacent cross-sections of GT: (a) Ground truth for Trial 2 pipe section 3, (b) Difference of adjacent cross sections.

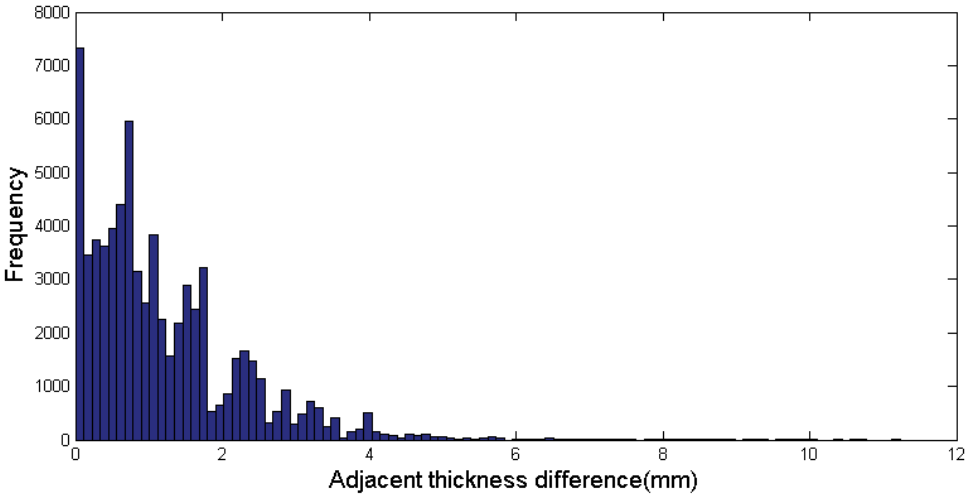

FIGURE 6.12: Histogram of adjacent axial cross-sectional difference in GT

approach gives a very close initial guess to start with which saves significant computation time.

Although the differences between a certain portion of the two signals are within the tolerance level, they do not need to be identical profiles. The presence of a gradual change of large diameter defect also called a lake type defect, can result in a drift which could be accumulated over iterations.

In order to address the possible drift error, the optimiser is run on the full profile at least once. So if there is an accumulated drift, there will be an iteration where the evaluation function exceeds the tolerance value. Once the cost is above the tolerance level, the region will be iterated until the cost function diverges. If the cost function returns an acceptable error value, the current profile thickness is kept the same as the initial value, and is not iterated further. This approach aids in saving the unnecessary computation time.

6.4 Results

One of the main objectives of this chapter was to enhance the MFL based defect interpretation using an iterative coarse to fine approach for cast iron water pipes. Aged water pipes were exhumed and used for forensic evaluation of the proposed method.

In Section 6.2.2 the dimensionality of the optimisation was simplified to a single variable optimisation. An analytical solution was derived for a two defect scenario and a worst case analysis was conducted for a multiple defect scenario. The multi-defect scenario was used in the optimisation framework for initial evaluation. The defect configuration is shown in Figure 6.8(b). After 2 iterations through the profile, the proposed framework could converge on the groundtruth profile with promising agreement ($\pm 0.4mm$). The resulting profile is illustrated in Figure 6.13.

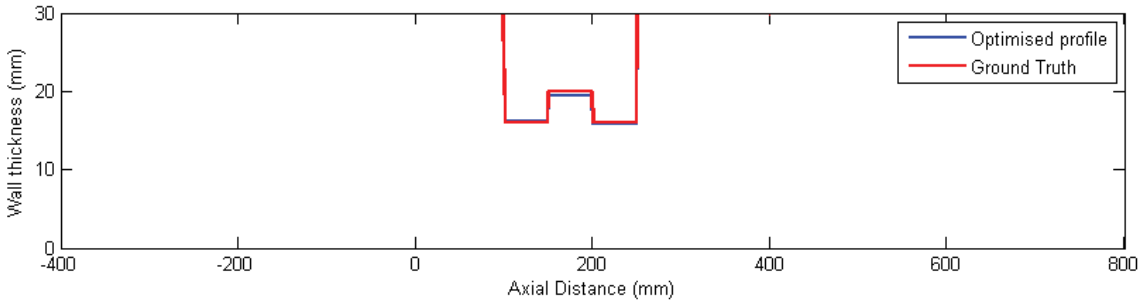

FIGURE 6.13: Worst case analysis: optimisation result

With the above validation, the framework was intended to be applied on real experimental data from the industry partner. When the industrial data was analysed by the proposed framework, some major issues appeared.

1. MFL sensor lift-off was unknown due to the uneven surface where the tool rests. Due to the adjustment of the tool for individual scans, this error was further increased and was unpredictable.

2. Although the scanning and ground truthing was done with respect to a carefully selected reference frame, due to the industrial MFL scanning procedure, some of the axial and radial localisations were erroneous and did not correlate with the ground truth.

To overcome these experiment related issues, the $3D$ groundtruth was used in the validated Comsol simulations to generate the MFL response. All the localisation issues as well as all tool specific error sources were avoided with this approach.

Initially the GP model was used to interpret the simulated MFL response signal and was used as the 'coarse' initial solution of the profile. This initial 'coarse' solution compared against the cross section of the ground truth is shown in Figure 6.9.

It is to be noted that these GP based solutions are only available at signal peaks. Starting from this seed, the iterative optimiser alters the profile to minimise the error between the measurement and the model response. The numerical solver is set to terminate once the error margin drops below a termination tolerance. Figure 6.14 shows the 'fine' result generated for the above example.

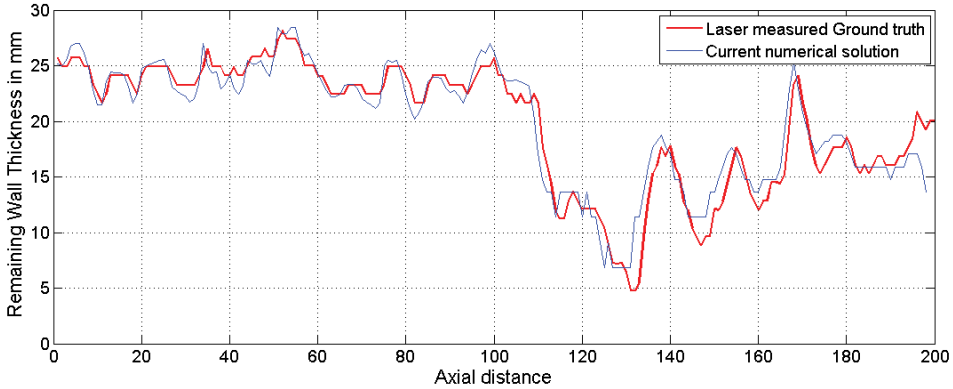

FIGURE 6.14: Iterative 'fine' solution

It is important to analyse the RMS error of the resulting cross section compared to ground truth and how it behaves with the number of iterations. Figure 6.15 shows the RMS error

vs number of iterations. It is clear that with the number of iterations, the RMS error decreases, but eventually converges to a close to optimal solution.

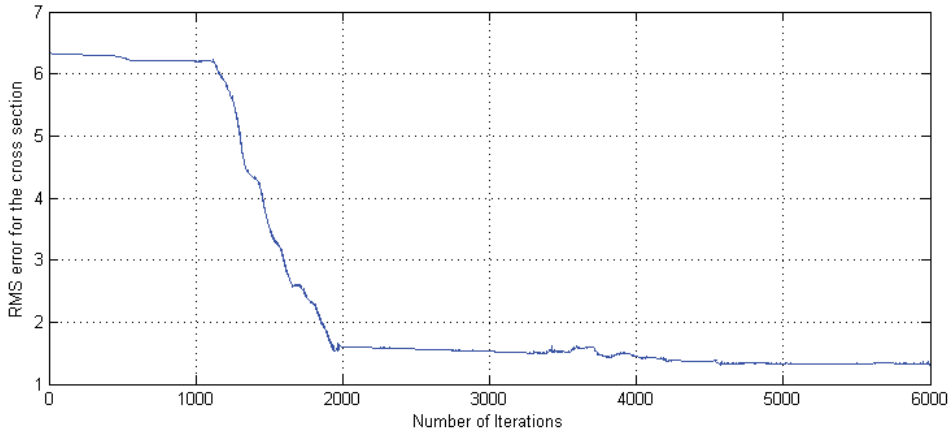

FIGURE 6.15: RMS error variation with number of iterations

Given the raster scan nature of MFL measurements, each cross-sectional profile was estimated individually. These profiles are later arranged in the original order to reconstruct the dense $2.5D$ thickness map of the full scan area. As an example, the reconstructed $2.5D$ thickness map is compared to the ground truth in Figure 6.16.

It is observed that the reconstruction is generally better at predicting the valleys than the hills. Generally the deepest valleys represent the major constrictions for the flux and therefore have the highest influence on the leakage which is resembled in the end reconstruction result too.

6.5 Discussions and Chapter Conclusions

The MFL signal was further processed to generate dense $2.5D$ thickness maps. Previously generated GP interpretations were initially used as a prior and the framework was derived to be a coarse to fine approach.

The underlying Comsol model used a simplified $2D$ simulation model due to limited computational power. Although the strong excitation field is axially oriented, this approximation could result in minor errors due to the absence of spacial profiles changes. Using a full

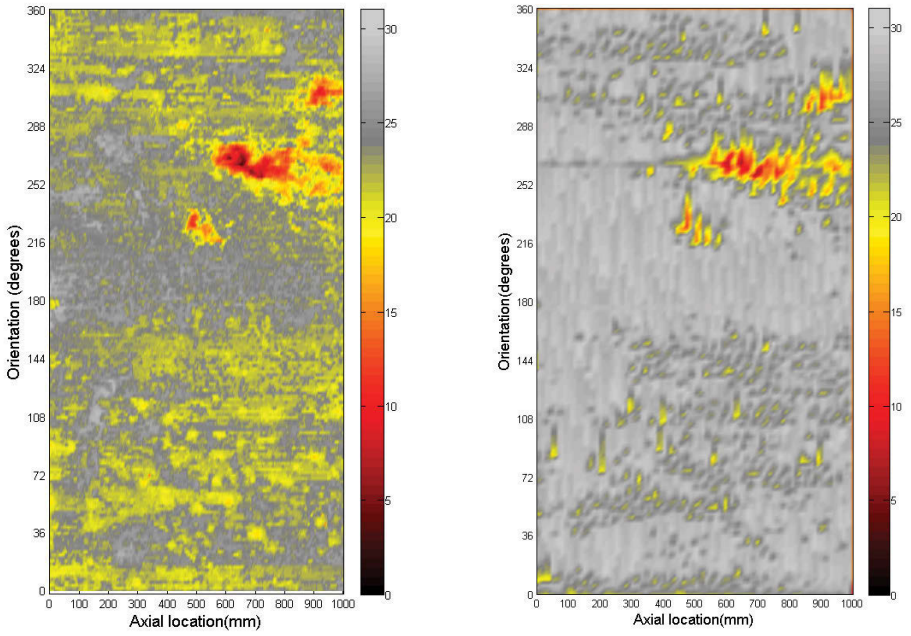

(a) (b)

FIGURE 6.16: Comparison of ground truth and optimised 2.5D thickness map for Trial 2 pipe section 3: (a) 2.5D Ground truth plot, (b) Optimised 2.5D thickness map.

3*D* FEA model would be the best solution but it includes an exponential increase of the computation time.

Also the U-shaped magnetising unit was replaced with an imaginary constant excitation field. This approximation also could slightly distort the signals compared to those obtained with the moving magnetisation unit. In addition, there are other unwanted influences as well as noise sources with unknown characteristics being present on MFL signals which all suggests that the real profile reconstructions using industrial data will have a higher error than those presented.

Chapter 7

Conclusions

This thesis focused on the task of modelling and interpreting techniques for MFL technology. It introduced the dipole based analytical solution as an initial MFL model and identified its limitations. To overcome those limitations a FEA based simulation model was developed. Simulated MFL data as well as experimental data was used for validations and evaluations of different interpretation frameworks.

Three different interpretation frameworks were presented in this thesis. Those methods were validated using simulated data and were then evaluated using experimental data. These designed interpretation techniques were benchmarked by comparing their performance to the results presented in industrial reports using the same data. Extensive simulation as well as real world experimental results were employed in this process.

7.1 Summary of Contributions

7.1.1 A comprehensive design of a semi-automated MFL lab set-up

This thesis presented a comprehensive methodology to develop a realistic MFL model followed by a prototyped lab set-up. A dipole based parametric analytical model captures the underlying MFL phenomenon. This model also validated the MFL FEA model. In the proposed framework the simulation model was prototyped as an improved MFL lab

set-up that employs a semi-automated scanning procedure. The developed realistic model was used to generate extensive data required for the data analytic methods.

7.1.2 Data driven machine learning framework for MFL interpretations which includes uncertainty of predictions

The advent of kernel machines, such as Gaussian Processes (GP) can be formulated as a non-linear regression. This thesis presented a Gaussian processes based data driven inverse modelling framework to characterise the geometry of multiple defects, *i.e.* depth and width of defects and their associated uncertainties. The GP models trained with the validated simulation models generate accurate predictions and the associated uncertainties which can be used in the decision making process of asset maintenance. The results are superior to the state of the art industry interpretations.

7.1.3 A novel analytical model-aided ellipsoidal defect estimation framework

Latest stress and failure analysis shows that ellipsoidal defects are the most vulnerable stress failure source on gray cast iron pipes. A novel analytical model-aided ellipsoidal defect estimation framework was introduced to aid these stress concentration factor (SCF) calculations. This framework utilises a non linear optimisation algorithm using a MFL analytical model. The ellipsoidal parameters are estimated based on raw MFL signals compared to model generated signals and it was verified through simulations and experiments..

7.1.4 Reconstruction of dense $2.5D$ thickness maps using MFL measurements

This thesis presented a global optimiser based framework to reconstruct a dense $2.5D$ high resolution thickness map of the entire scan area using MFL signals generated on ground truth. Non linear optimisation framework minimises the mismatch between the MFL

measurement signal and the FEA simulated signal. Reconstruction results are compared with ground truth to validate the algorithm.

7.2 Discussion of Limitations

A few limitations of the three interpretation frameworks presented in this thesis have been identified. First, all methodologies either use a simulation model or an analytical model. These models are designed to match a certain design of the MFL tool. Tool specific parameters needs to be known to develop the models. When such parameters are not available, it may be possible to employ a calibration process using known sets of defects for the same purpose. However resulting models and interpretation results would be less accurate than those obtained using known tool parameters.

Due to the limitations of the industry tool, this thesis focused only on the axial (X) component of the MFL signal (Section 3.1). The other two components, most importantly the radial (Y) component contain defect information[26, 27]. Although these could contain complementary information, considering all the signal components could result in more accurate and robust results.

MFL signals can be contaminated from a number of noise sources, affecting the end accuracy of the results. In-homogeneity of the material, residual magnetisation, tool lift off and operation related errors, vibration artefacts are some major noise sources found in MFL phenomenon. Some of these error sources could be minimised by improved engineering designs of the tool as described in Section 3.3.3 . Remaining noise levels should be identified and quantified to be used in the machine learning process to gain better interpretations as presented in Section 3.3.5 .

The GP based interpretation framework highly depends on the thickness of the material. Although most of the $660mm$ diameter CI pipes are $30mm$ in thickness, other large diameter pipes can have varying wall thicknesses. The GP models highly depend on the dataset used for training, and the nominal thickness used for generating the data. When delivering the software package to the industry partners, different models were trained for different possible thickness values as a solution for this limitation.

All frameworks required high processing power at some stage during the process either on-line or off-line. Mainly the reconstruction of dense $2.5D$ thickness maps needed high computation power since the framework required exhaustive forward model evaluations. Section 6.2.2 discussed the simplifications used to save the computation time which resulted in a significant improvement. Moreover, the computation time can be reduced by changing the required level of details. For some analysis, a very high resolution is not required. In some cases it might only require defects higher or lower than a certain threshold. These scenarios need to be addressed case by case basis, but the core framework remains unchanged.

Although the main focus of this work was Cast Iron pipes, proposed frameworks can be used for other materials as well. However, this requires the knowledge of magnetic properties of the material and re-generation of the models. It is a challenging task to generalise the models for any material of any thickness.

One of the other major limitation to MFL in general is that the technique is only applicable to ferromagnetic material. Water industry nowadays use PVC and other polymers as pipe material mainly due to economical reasons. Most electromagnetic NDE techniques including MFL cannot be used for condition assessment of these material.

7.3 Future Work

This thesis demonstrated a few techniques to interpret MFL signals in an accurate and a robust way. However, there are a number of additional improvements that can be incorporated into those frameworks to further increase their utility. Although these improvements are beyond the scope of this thesis, they are presented here with the hope that they may inspire future work on MFL signal interpretation.

The usage of an FEM model, without the need for supportive but inflexible secondary models, also allows further improvements in MFL modelling accuracy using the same concept by simply adding more detail to the FEA model presented in Chapter 6. For example this could incorporate eddy current effects due to motion of the magnetising unit. However, this requires implementing the full FEA solution in Matlab rather than using

software packages like Comsol. This approach would not only give more flexibility to the model but also would be computationally fast. Moreover similar to the method presented by Priewald *et al.* [39] the Jacobian information for the optimisations can be extracted directly from the FEA implementation.

The machine learning approach generates a quantitative indication of the uncertainty for each prediction, whereas the iterative optimisation frameworks are not generating the uncertainty. A fully implemented FEA solution could also provide Jacobian information to calculate uncertainty values in the iterative process. These values can be successfully utilised in the asset management process.

Future work should also look into the possibility of extending the frameworks to be martial and thickness invariant. In real world scenarios large diameter pipes are found in a variety of materials and thicknesses. Generalising the frameworks for all these practical scenarios is foreseen to be very productive. However the approach to generalise the modes remains to be investigated.

Bibliography

[1] Advanced Engineering Solutions Limited. smartcat, 2015. URL http://www.aesengs.co.uk/inspection.php.

[2] F. Förster. New findings in the field of non-destructive magnetic leakage field inspection. *NDT International*, 19(1):3–14, February 1986. ISSN 03089126. doi: 10.1016/0308-9126(86)90134-3. URL http://linkinghub.elsevier.com/retrieve/pii/0308912686901343.

[3] A.a. Carvalho, J.M.a. Rebello, L.V.S. Sagrilo, C.S. Camerini, and I.V.J. Miranda. MFL signals and artificial neural networks applied to detection and classification of pipe weld defects. *NDT & E International*, 39(8):661–667, December 2006. ISSN 09638695. doi: 10.1016/j.ndteint.2006.04.003. URL http://linkinghub.elsevier.com/retrieve/pii/S096386950600034X.

[4] Wenhua Han and Peiwan Que. A Modified Wavelet Transform Domain Adaptive FIR filtering Algorithm for Removing the SPN Contained in the MFL data. In *IEEE International Conference on Industrial Technology*, pages 152–157. IEEE, 2005. ISBN 0-7803-9484-4. doi: 10.1109/ICIT.2005.1600627. URL http://ieeexplore.ieee.org/xpl/articleDetails.jsp?arnumber=1600627.

[5] Vijay Babbar and Lynann Clapham. Residual Magnetic Flux Leakage : A Possible Tool for Studying Pipeline Defects. *Journal of Nondestructive Evaluation*, 22(4):117–125, 2004.

[6] B O Hjorth. Technical contributions eeg analysis based on time domain properties. *Electroncephalography and Clinical Neurophysiology*, 29:306–310, 1970.

[7] RB Petersen and RE Melchers. Long-term corrosion of cast iron cement lined pipes. *Corrosion and Prevention*, pages 11–14, 2012.

[8] Jaime Valls Miro, Jeya Rajalingam, Teresa Vidal-Calleja, Freek de Bruijn, Roger Wood, Dammika Vitanage, Nalika Ulapane, Buddhi Wijerathna, and Daoblige Su. A live test-bed for the advancement of condition assessment and failure prediction research on critical pipes. *Water Asset Management International, ISSN Print: 1814-5434, ISSN Online: 1814-5442*, 10(2):03–08, 2014.

[9] Dammika Vitanage, Jayantha Kodikara, and Greg Allen. Collaborative research on condition assessment and pipe failure prediction for critical water mains. *Water Asset Management International*, 10:15–18, 2014.

[10] Sydney Water Inc. Sydney water corporation, 2015. URL `http://www.sydneywater.com.au/`.

[11] Robert Petersen, Matthew Dafter, and Robert Melchers. Long-term corrosion of buried cast iron water mains: field data collection and model calibration. *Water Asset Management International*, 9:13–17, 2013.

[12] Zheng Liu and Yehuda Kleiner. State of the art review of inspection technologies for condition assessment of water pipes. *Measurement*, 46(1):1–15, 2013. doi: 10.1016/j.measurement.2012.05.032.

[13] Nalika Ulapane, Alen Alempijevic, Teresa Vidal-Calleja, Jaime Valls Miro, Jeremy Rudd, and Martin Roubal. Gaussian process for interpreting pulsed eddy current signals for ferromagnetic pipe profiling. In *Industrial Electronics and Applications (ICIEA), 2014 IEEE 9th Conference on*, pages 1762–1767. IEEE, 2014. doi: 10.1109/ICIEA.2014.6931453.

[14] Max Wishaw. Notes on the industrial technologies for crack detection and condition monitoring. *Structural Monitoring Systems Limited*, pages 1–9, 2009.

[15] Critical Pipes Project. The advanced condition assessment and pipe failure prediction project, 2015. URL `http://www.criticalpipes.com/`.

[16] Weiying Cheng. Pulsed eddy current testing of carbon steel pipes wall-thinning through insulation and cladding. *Journal of Nondestructive Evaluation*, 31(3):215–224, 2012. doi: 10.1007/s10921-012-0137-9.

[17] Zhiyuan Xu, Xinjun Wu, Jian Li, and Yihua Kang. Assessment of wall thinning in insulated ferromagnetic pipes using the time-to-peak of differential pulsed eddy-current testing signals. *NDT & E International*, 51:24–29, 2012. doi: 10.1016/j.ndteint.2012.07.004.

[18] Burd John. Magnetic flux leakage old and new, magnetics in nondestructive testing. volume 1, pages 8–13, April 2005.

[19] JC Drur and N Pearson. Corrosion detection in ferrite steels using magnetic flux leakage. volume 1, pages 14–19, April 2005.

[20] K Mandal, Th Cramer, and D L Atherton. The study of a racetrack-shaped defect in ferromagnetic steel by magnetic Barkhausen noise and flux leakage measurements. *Journal of Magnetism and Magnetic Materials*, 212:231–239, 2000.

[21] J R Davis. ASM specialty handbook: cast irons. *ASM International*, 124:433–435, 1996.

[22] Buddhi Wijerathna, Teresa Vidal-Calleja, Sarath Kodagoda, Qiang Zhang, and Jaime Valls Miro. Multiple defect interpretation based on gaussian processes for MFL technology. *Nondestructive Characterization for Composite Materials, Aerospace Engineering, Civil Infrastructure, and Homeland Security*, pages 86941Z–86941Z–12, April 2013. doi: 10.1117/12.2009966.

[23] Jian Ji, Chunshun Zhang, Jayantha Kodikara, and Sheng-Qi Yang. Prediction of stress concentration factor of corrosion pits on buried pipes by least squares support vector machine. *Engineering Failure Analysis*, 55:131 – 138, 2015. ISSN 1350-6307.

[24] Buddhi Wijerathna, Sarath Kodagoda, Jaime Valls Miro, and Gamini Dissanayake. Iterative coarse to fine approach for interpretation of defect profiles using mfl measurements. *Proceedings of the 10th IEEE International Conference on Industrial Electronics and Applications*, 2015.

[25] Daobilige Su, Nalika Ulapane, and Buddhi Wijerathna. An acoustic sensor based novel method for 2d localization of a robot in a structured environment. *Proceedings of the 10th IEEE International Conference on Industrial Electronics and Applications*, 2015.

[26] N N Zatsepin and V E Shcherbinin. Calculation of the magnetostatic field of surface defects. *Defectoskopiya*, 5:50–59, 1966.

[27] V E Shcherbinin and A I Pashagin. Influence of the extension of adefect on the magnitude of its magnetic field. *Defectoskopiya*, 8:74–82, 1972.

[28] R.C. Ireland and C.R. Torres. Finite element modelling of a circumferential magnetiser. *Sensors and Actuators A: Physical*, 129(1-2):197–202, May 2006. ISSN 09244247. doi: 10.1016/j.sna.2005.11.066. URL `http://linkinghub.elsevier.com/retrieve/pii/S092442470500693X`.

[29] D.L. Atherton and W Czura. Finite element calculations on the effects of permeability variation on magnetic flux leakage signals. *NDT International*, 20, 1987. URL `http://www.sciencedirect.com.ezproxy.lib.uts.edu.au/science/article/pii/0308912687902483`.

[30] D L Atherton and M G Daly. Finite element calculation of magnetic flux leakage detector signals. *NDT & E International*, 20(4):235–238, 1987.

[31] Yong Li, John Wilson, and Gui Yun Tian. Experiment and simulation study of 3D magnetic field sensing for magnetic flux leakage defect characterisation. *NDT & E International*, 40(2):179–184, March 2007. ISSN 09638695. doi: 10.1016/j.ndteint.2006.08.002. URL `http://linkinghub.elsevier.com/retrieve/pii/S0963869506000934`.

[32] D. Minkov, Y. Takeda, T. Shoji, and J. Lee. Estimating the sizes of surface cracks based on Hall element measurements of the leakage magnetic field and a dipole model of a crack. *Applied Physics A: Materials Science & Processing*, 74(2):169–176, February 2002. ISSN 0947-8396. doi: 10.1007/s003390100899. URL `http://www.springerlink.com/openurl.asp?genre=article&id=doi:10.1007/s003390100899`.

[33] Catalin Mandache and Lynann Clapham. A model for magnetic flux leakage signal. *Journal of Physics D: Applied Physics*, 36:2427–2431, 2003.

[34] MATLAB. *Signal processing toolbox for use with MATLAB*. Natick, MA: The Math Works Inc., 1999.

[35] Sophocles J. Orfanidis. *Introduction to signal processing*. Prentice Hall, 1996.

[36] a. Khodayari Rostamabad, J.P. Reilly, N.K. Nikolova, J.R. Hare, and S. Pasha. Machine Learning Techniques for the Analysis of Magnetic Flux Leakage Images in Pipeline Inspection. *IEEE Transactions on Magnetics*, 45(8):3073–3084, August 2009. ISSN 0018-9464. doi: 10.1109/TMAG.2009.2020160. URL `http://ieeexplore.ieee.org/lpdocs/epic03/wrapper.htm?arnumber=5170224`.

[37] A. Joshi, L. Udpa, S. Udpa, and A. Tamburrino. Adaptive Wavelets for Characterizing Magnetic Flux Leakage Signals From Pipeline Inspection. *IEEE Transactions on Magnetics*, 42(10):3168–3170, October 2006. ISSN 0018-9464. doi: 10.1109/TMAG.2006.880091. URL `http://ieeexplore.ieee.org/lpdocs/epic03/wrapper.htm?arnumber=1704562`.

[38] Simon O. Haykin. *Neural Networks and Learning Machines (3rd Edition)*. Prentice Hall, 2008. ISBN 0131471392. URL `http://www.amazon.com/Neural-Networks-Learning-Machines-Edition/dp/0131471392`.

[39] R.H. Priewald, C. Magele, P.D. Ledger, N.R. Pearson, and J.S.D. Mason. Fast magnetic flux leakage signal inversion for the reconstruction of arbitrary defect profiles in steel using finite elements. *Magnetics, IEEE Transactions on*, 49(1):506–516, Jan 2013. ISSN 0018-9464. doi: 10.1109/TMAG.2012.2208119.

[40] Zhenmao Chen, G. Preda, O. Mihalache, and Kenzo Miya. Reconstruction of crack shapes from the mflt signals by using a rapid forward solver and an optimization approach. *Magnetics, IEEE Transactions on*, 38(2):1025–1028, 2002. doi: 10.1109/20.996263.

[41] R Schifini and A C Bruno. Experimental verification of a finite element model used in a magnetic flux leakage inverse problem. *Journal of Physics D: Applied Physics*, 38(12):1875, 2005.

[42] K.C. Hari, M. Nabi, and S.V. Kulkarni. Improved fem model for defect-shape construction from mfl signal by using genetic algorithm. *Science, Measurement Technology, IET*, 1(4):196–200, July 2007. ISSN 1751-8822.

[43] Yong Zhang, Zhongfu Ye, and Chong Wang. A fast method for rectangular crack sizes reconstruction in magnetic flux leakage testing. *NDT & E International*, 42(5):369 – 375, 2009. ISSN 0963-8695. doi: http://dx.doi.org/10.1016/j.ndteint.2009.01.006.

[44] M. Ravan, R.K. Amineh, S. Koziel, N.K. Nikolova, and J.P. Reilly. Sizing of 3-d arbitrary defects using magnetic flux leakage measurements. *Magnetics, IEEE Transactions on*, 46(4):1024–1033, April 2010. ISSN 0018-9464.

[45] Reza K. Amineh, S. Koziel, N.K. Nikolova, J.W. Bandler, and J.P. Reilly. A space mapping methodology for defect characterization from magnetic flux leakage measurements. *Magnetics, IEEE Transactions on*, 44(8):2058–2065, Aug 2008. ISSN 0018-9464. doi: 10.1109/TMAG.2008.923228.

[46] M. Yan, S. Udpa, S. Mandayam, Y. Sun, P. Sacks, and W. Lord. Solution of inverse problems in electromagnetic nde using finite element methods. *Magnetics, IEEE Transactions on*, 34(5):2924–2927, Sep 1998. ISSN 0018-9464. doi: 10.1109/20.717682.

[47] P. Mojabi and J. LoVetri. Overview and classification of some regularization techniques for the gauss-newton inversion method applied to inverse scattering problems. *Antennas and Propagation, IEEE Transactions on*, 57(9):2658–2665, Sept 2009. ISSN 0018-926X.

[48] M. Vauhkonen, D. Vadasz, P.A. Karjalainen, E. Somersalo, and J.P. Kaipio. Tikhonov regularization and prior information in electrical impedance tomography. *Medical Imaging, IEEE Transactions on*, 17(2):285–293, April 1998. ISSN 0278-0062. doi: 10.1109/42.700740.

[49] M Afzal and s Udpa. Advanced signal processing of magnetic flux leakage data obtained from seamless gas pipeline. *NDT & E International*, 35(7):449–457, October 2002.

[50] S. Hosur and A.H. Tewfik. Wavelet transform domain adaptive FIR filtering. *IEEE Transactions on Signal Processing*, 45(3):617–630, March 1997. ISSN 1053587X. doi: 10.1109/78.558477. URL `http://ieeexplore.ieee.org/xpls/abs_all.jsp?arnumber=558477`.

[51] S.G. Mallat. A theory for multiresolution signal decomposition: the wavelet representation. *IEEE Transactions on Pattern Analysis and Machine Intelligence*, 11 (7):674–693, July 1989. ISSN 01628828. doi: 10.1109/34.192463. URL `http://ieeexplore.ieee.org/xpls/abs_all.jsp?arnumber=192463`.

[52] Yong Li, Gui Yun Tian, and Steve Ward. Numerical simulation on magnetic flux leakage evaluation at high speed. In *NDT & E International*, volume 39, pages 367–373, July 2006. doi: 10.1016/j.ndteint.2005.10.006. URL `http://linkinghub.elsevier.com/retrieve/pii/S0963869505001544`.

[53] S. Mandayam, L. Udpa, S.S. Udpa, and W. Lord. Invariance transformations for magnetic flux leakage signals. *IEEE Transactions on Magnetics*, 32(3):1577–1580, May 1996. ISSN 00189464. doi: 10.1109/20.497553.

[54] Liang Chen, Xing Li, Xun-bo Li, and Zuo-ying Huang. Signal extraction using ensemble empirical mode decomposition and sparsity in pipeline magnetic flux leakage nondestructive evaluation. *Review of Scientific Instruments*, 80(2):025105, 2009.

[55] Yan Shi, Chao Zhang, Rui Li, Maolin Cai, and Guanwei Jia. Theory and application of magnetic flux leakage pipeline detection. *Sensors*, 15(12):29845, 2015. ISSN 1424-8220. doi: 10.3390/s151229845.

[56] K Mandal and D.L. Atherton. A study of magnetic flux-leakage signals. *Journal of Physics D: Applied Physics*, 31:3211—-3217, 1998.

[57] S.E. Heath. Residual and active magnetostatic leakage field modeling. Master's thesis, Colorado State University Fort Collins Colorado, 1984.

[58] S.R. Satish. Finite element modeling of residual magnetic phenomena. Master's thesis, Colorado State University Fort Collins Colorado, 1980.

[59] S.M. Dutta, F.H. Ghorbel, and R.K. Stanley. Dipole modeling of magnetic flux leakage. *Magnetics, IEEE Transactions on*, 45(4):1959–1965, April 2009. ISSN 0018-9464. doi: 10.1109/TMAG.2008.2011895.

[60] C Edwards and S B Palmer. The magnetic leakage field of surface-breaking cracks. *Journal of Physics D: Applied Physics*, 19(4):657, 1986. URL `http://stacks.iop.org/0022-3727/19/i=4/a=018`.

[61] Gwan Soo Park and Sang Ho Park. Analysis of the velocity-induced eddy current in mfl type ndt. *Magnetics, IEEE Transactions on*, 40(2):663–666, March 2004. ISSN 0018-9464. doi: 10.1109/TMAG.2004.824717.

[62] M. Ravan, R.K. Amineh, S. Koziel, N.K. Nikolova, and J.P. Reilly. Sizing of multiple cracks using magnetic flux leakage measurements. *Science, Measurement Technology, IET*, 4(1):1–11, January 2010. ISSN 1751-8822. doi: 10.1049/iet-smt.2009.0054.

[63] H. C. Martin M. J. Turner, R. W. Clough and L. J. Topp. Stiffness and deflection analysis of complex structures. *Journal of the Aeronautical Sciences*, 23(9):805–823, 1956.

[64] Joo Pedro A. Bastos and Nelson Sadowski. *Electromagnetic Modeling by Finite Element Methods* . CRC Press; 1 edition, 2003.

[65] COMSOL Multiphysics. Comsol multiphysics user guide (version 4.3 a). *COMSOL, AB*, 2012.

[66] G. Katragadda, W. Lord, Y.S. Sun, S. Udpa, and L. Udpa. Alternative magnetic flux leakage modalities for pipeline inspection. *Magnetics, IEEE Transactions on*, 32(3): 1581–1584, May 1996. ISSN 0018-9464. doi: 10.1109/20.497554.

[67] T.L. Chow. *Introduction to Electromagnetic Theory: A Modern Perspective*. Jones and Bartlett Publishers, 2006. ISBN 9780763738273. URL `https://books.google.com.au/books?id=dpnpMhw1zo8C`.

[68] Pradeep Ramuhalli, Lalita Udpa, and Satish S. Udpa. Neural network-based inversion algorithms in magnetic flux leakage nondestructive evaluation. *Journal of Applied*

Physics, 93(10):8274–8276, 2003. doi: 10.1063/1.1558693. URL http://link.aip.org/link/?JAP/93/8274/1.

[69] C. Rasmussen and C. Williams. *Gaussian Process for Machine Learning*. MA:MIT press, Cambridge, 2006.

[70] C. K. I. Williams and C. E. Rasmussen. Gaussian processes for regression. In *Advances in Neural Information Processing Systems 8*, pages 514–520. MIT Press, June 1996. URL http://eprints.aston.ac.uk/651/1/getPDF.pdf.

[71] A. Brooks, A. Makarenko, and B. Upcroft. Gaussian Process Models for Indoor and Outdoor Sensor-Centric Robot Localization. *IEEE Transactions on Robotics*, 24(6): 1341–1351, December 2008. ISSN 1552-3098. doi: 10.1109/TRO.2008.2004887. URL http://ieeexplore.ieee.org/lpdocs/epic03/wrapper.htm?arnumber=4660315.

[72] D.J.C. MacKay. Introduction to gaussian processes. *NATO ASI Series F Computer and Systems Sciences*, 168:133–166, 1998.

[73] M. Gibbs and D.J.C. MacKay. Efficient implementation of gaussian processes. Technical report, Cavendish Lab., Cambridge, UK, 1997.

[74] Creaform Inc. Handyscan 3d laser scanner, 2015. URL http://www.creaform3d.com/en/ndt-solutions/handyscan-3d-laser-scanners.

[75] Cengiz Oztireli, Gael Guennebaud, and Markus Gross. Feature preserving point set surfaces based on non-linear kernel regression. *Computer Graphics Forum*, 28(2), 2009. URL http://vcg.isti.cnr.it/Publications/2009/OGG09.

[76] Bradley Skinner, Jaime Vidal-Calleja, Teresa amd Valls Miro, Freek De Bruijn, and Raphael Falque. 3D point cloud upsampling for accurate reconstruction of dense 2.5D thickness maps. In *Proceedings of the Australasian Conference on Robotics and Automation 2014 (ACRA 2014)*, pages 1–7, Melbourne, Australia, 2014. Australian Robotics and Automation Association Inc.

[77] J.M Makar. A preliminary analysis of failures in grey cast iron water pipes. *Engineering Failure Analysis*, 7(1):43 – 53, 2000. ISSN 1350-6307.

[78] W.D. Pilkey and D.F. Pilkey. *Peterson's Stress Concentration Factors*. Wiley, 2008. ISBN 9780470048245.

[79] CG Broyden. A new double-rank minimisation algorithm. preliminary report. In *Notices of the American Mathematical Society*, volume 16, page 670. AMER MATHEMATICAL SOC 201 CHARLES ST, PROVIDENCE, RI 02940-2213, 1969.

[80] WC Davidon. Variable metric method for minimization. In *Technical report, Argonne National Laboratories*, volume III, 1959.

[81] R. Fletcher and M. J. D. Powell. A rapidly convergent descent method for minimization. *The Computer Journal*, 6(2):163–168, 1963. doi: 10.1093/comjnl/6.2.163.

[82] Donald Goldfarb. A family of variable-metric methods derived by variational means. *Mathematics of Computation*, 24(109):pp. 23–26. ISSN 00255718', year =.

[83] David F Shanno. Conditioning of quasi-newton methods for function minimization. *Mathematics of computation*, 24(111):647–656, 1970.